

# UC Santa Cruz

## UC Santa Cruz Electronic Theses and Dissertations

**Title**

NANOCOMPOSITE ENABLED SENSITIZED SOLAR CELL

**Permalink**

<https://escholarship.org/uc/item/9804k8tj>

**Author**

Phuyal, Dibya

**Publication Date**

2012

Peer reviewed|Thesis/dissertation

UNIVERSITY OF CALIFORNIA

SANTA CRUZ

**NANOCOMPOSITE ENABLES SENSITIZED SOLAR CELL**

A Thesis Submitted in Partial Satisfaction  
Of the requirements for the degree of

MASTER OF SCIENCE

in

ELECTRICAL ENGINEERING

by

**Dibya D. Phuyal**

December 2012

The Thesis of Dibya Phuyal  
is approved:

---

Professor Bin Chen, Chair

---

Professor Holger Schmidt

---

Professor Nobuhiko Kobayashi

---

Tyrus Miller  
Vice Provost and Dean of Graduate Studies

Copyright © by

Dibya D. Phuyal

2012

## TABLE OF CONTENTS

GLOSSARY	VI
ABSTRACT	VII
ACKNOWLEDGEMENTS	IX
INTRODUCTION	1
1.1 The Energy Future	1
1.2 Current Solar Cells	2
1.3 Dye Sensitized Solar Cell	5
1.3.1 History and Concept	5
1.3.2 Operating Principles	6
1.3.3 Device Fundamentals	8
1.3.4 Kinetics	10
1.3.5 Material Components	12
1.3.5.1 Photoanode Semiconductors	12
1.3.5.2 Multiple TiO <sub>2</sub> Structure	15
1.3.6 Dye Sensitization	16
1.3.7 Electrolyte Dynamics	18
1.4 Outlook and Commercialization	20
1.5 Thesis Outline, Aims and Objectives	21
2 MATERIAL PROPERTIES & CHARACTERIZATION	23
2.1 Materials Used	24
2.1.1 FTO	24
2.1.2 TiO <sub>2</sub> Morphologies	24
2.1.3 PbS Quantum Dots	25
2.1.4 CuPc	28
2.1.5 Iodine/Iodide Electrolyte	30
2.1.6 Pt as Counter Electrode	30

2.2 Device Architecture	30
2.2.1 Single Sensitization	31
2.2.2 Co-Sensitization	31
3 EXPERIMENTAL PROCEDURE AND CHARACTERIZATION	33
3.1 Material Synthesis and Electrode Preparation	33
3.1.1 Preparation of FTO/Glass Slides	34
3.1.2 Preparation of TiO <sub>2</sub> Photoanode	34
3.2.1 Dip Coating of TiO <sub>2</sub> Solution in Isopropanol	35
3.2.2 Dr. Blade Method	37
3.2.3 Synthesis of TiO <sub>2</sub> Nanowires	38
3.2.4 Preparation of TiO <sub>2</sub> Nanoparticle/Nanowire Composite	39
3.3 Preparation of CuPc Suspension	40
3.3 Synthesis of PbS Quantum Dots <i>in situ</i> on TiO <sub>2</sub> Nanowires	42
3.4 Platinum Deposition on Counter Electrode via DC Sputtering	43
3.5 Injection of Electrolyte	44
3.6 Material Characterization	44
3.6.1 Raman Spectroscopy (Renishaw inVia Raman Microscope)	45
3.6.2 Photoluminescence	45
3.6.3 SEM (Hitachi S-4800 Scanning Electron Microscope)	45
3.6.4 TEM (Hitachi Transmission Electron Microscope)	45
3.6.5 AFM (Multimode Atomic Force Microscopy)	45
3.6.6 UV-Vis (Jasco V-670 UV-Vis Spectrophotometer)	46
3.6.7 4-Point Probe (MMR Technologies)	46
3.7 Device Assembly	49
3.7.1 Secondary FTO with Pt and Parafilm Spacer	50
3.8 Solar Cell Characterization and Measurement	50
4 RESULTS AND DISCUSSION	53
4.1 Material Characterization	54
4.1.1 TiO <sub>2</sub> Photoanode	54

4.1.2 TiO <sub>2</sub> Nanowires	56
4.1.3 Resistivity of photoanode	59
4.1.4 CuPc Characterization	60
4.1.5 PbS Quantum Dots	62
4.1.5.1 Photoluminescence of PbS QDs	64
4.1.5.2 Crystallization Cycles of PbS Quantum Dots	66
4.1.5.3 Stability and Degradation of Quantum Dots	67
4.2 Co-Sensitization of TiO <sub>2</sub> Nanostructures by Raman and UV-Vis Spectroscopy	68
4.3 Photocurrent and I-V Characteristics	70
4.4 CuPc Dispersed in TiO <sub>2</sub> Matrix	74
 5 CONCLUSION AND FUTURE WORK	 76
 APPENDIX	 80
Appendix A	81
Appendix B	82
Appendix C	83
 REFERENCES	 86

# Glossary

Si – Silicon

NREL – National Renewable Energy Laboratory

$E_g$  – Energy Band Gap

NIR – Near Infrared

DSSC – Dye Sensitized Solar Cell

TiO<sub>2</sub> – Titanium (II) Dioxide

TCO – Transparent Conducting Oxide

WE – Working Electrode

HOMO – Highest Occupied Molecular Orbital

LUMO – Lowest Occupied Molecular Orbital

CE – Counter Electrode

CB – Conduction Band

VB – Valence Band

Pbs – Lead (II) Sulfide

MPc -Metal-phthalocyanines

CuPc – Copper phthalocyanine

Pt - Platinum

QDs – Quantum Dots

$V_{OC}$  – Open-Circuit Voltage

$I_{SC}$  – Short-Circuit Current

FF – Fill Factor

FTO – Fluorine-Doped Tin Oxide

ITO – Indium-Doped Tin Oxide

DI – Deionized Water

# Abstract

Dye Sensitized solar cells (DSSCs) are a promising candidate for next generation photovoltaic panels due to their low cost, easy fabrication process and relative high efficiency. Despite considerable effort on the advanced of DSSCs, the efficiency has been stalled for nearly a decade due to the complex interplay among various DSSC components. DSSCs consist of a photoanode on a conducting substrate, infiltrated dye for light absorption and electron injection, and an electrolyte to regenerate the dye. On the photoanode is a high band-gap semiconducting material, primarily of a nanostructure morphology of titanium (II) dioxide ( $\text{TiO}_2$ ), dye molecules whose molar absorption is typically in the visible spectrum, are adsorbed onto the surface of  $\text{TiO}_2$ . To improve the current DSSCs, there are many parameters that can be investigated.

In a conventional DSSC, a thick semiconducting layer such as the nanoparticle  $\text{TiO}_2$  layer induces charge separation efficiently while concurrently increasing the charge transport distance, leading the cell to suffer from more charge recombination and deterioration in charge collection efficiency. To improve on this limitation,  $\text{TiO}_2$  nanowires (NW) and nanotubes (NT) are explored to replace the nanoparticle photoanode. One-dimensional nanostructures are known for the excellent electron transport properties as well as maintaining a relatively high surface area. Hence one of the focuses of this thesis explores at using different morphologies and composition of  $\text{TiO}_2$  nanostructures to enhance electron collection efficiency.

Another challenge in conventional DSSCs is the limit in light absorption of solar irradiation. Dyes are limited to absorption only in the visible range, and have a low molar absorption coefficient in the near infrared (NIR). Tuning dyes is extremely complicated and may have more disadvantages than simply extending light harvesting. Therefore our strategy is to incorporate quantum dots to replace the dye, as well as prepare a cell for the possibility of co-sensitization, thereby extending the absorption of light in the visible and NIR.

The first phase of the thesis involves the synthesis and characterization of the materials used for the cell. We successfully synthesized  $\text{TiO}_2$  nanowires and nanotubes and characterized them for the use as the photoanode. Both one-dimensional structures proved to have low resistivity, chemical stability, and high density. We also synthesized Lead (II) Sulfide (PbS) quantum dots (QDs) and explored at modifying their



diameter in order to properly control their light harvesting potential into the NIR region. The electron transport kinetics proved to be faster in one-dimensional nanostructure due to their high crystallinity order and reduced elastic scattering of the electrons during transport. Furthermore, quantum dots were synthesized such that their band-gap allowed for the absorption of NIR light. This result extended the harvesting potential of our solar cell and suggests the possibility for co-sensitization in DSSCs using dye molecules and quantum dots.

Hence, the focus of this thesis work is to systematically explore a transformative way to fundamentally enhance charge transport and extend light absorption by incorporation of two sensitizing agents.

# Acknowledgements

I would like to extend my gratitude and many thanks to Dr. Chen for the opportunity given to me. She has introduced me to the diverse and dynamic field of nanomaterials and their applications. Her group gave me insights into the nature of nanomaterials, the synthesis procedures, and ultimately the range of devices her group develops. I especially want to thank her for introducing me into dye sensitized solar cell and the potential they can serve in photovoltaic research. Experimenting with this cell gave me insights into the multidisciplinary approach, combining chemistry, physics, material science, and engineering. I thank her sincerely for her patience, guidance, and her keen knowledge in this field.

A special thanks to Professor Holger Schmidt in the electrical engineering department. It was an educational experience being his teaching assistant, a student in his class, and his guidance through this research endeavor. I would also like to extend gratitude to Professor Nobby Kobayashi for his guidance and counseling throughout my graduate career.

I would like to acknowledge Mr. Zuki Tanaka for his enormous support, guidance into instrumentation and spectroscopy, his ideas and creativity, and specially his problems solving skills. It was with his help that I was able to do this, and we built a friendship through this time that I am very grateful for. My other colleagues also deserve mention for their support in material synthesis and general chemistry: Cristina Javier, Robin Young, Arthur Cheng, Alex LeGrande, and Dr. Nicolas Ladando.

I also want to thank Prof. Micheal Oye and Mr. Joey Varelas for all their support in sputtering, SEM, TEM, and research activities at NASA Ames Laboratory. Dr. Jessica Koehne also provided support in this thesis and I am very thankful for her support.

I am also thankful for all the friends that I made during this time, especially members of the engineering department. They have made my time here fruitful and enjoyable. I also want to extend my thanks to Ms. Camilla Lind, who has given me tremendous support and enriched my life during this period.

Finally, I would like to thank my brother, my mother, and my father for all their love, support, and encouragement.

to my father and mother

# 1

## Introduction

### **1.1 The Energy Future**

Energy has long played a critical role in nations' national security, economic prosperity, and environmental quality, and today concerns about how the world produces and consumes energy are at the forefront of public attention. Political instability in primary energy-producing regions around the world, rapidly rising global demand for energy, especially in developing countries, and a growing awareness of the impact of fossil fuel use on global climate change have contributed to a new sense of urgency about the role of energy in our society. Now a renewed sense of urgency has raised the stakes and the scale of the challenge.

Global warming and the impending exhaustion of fossil fuels are placing increasing demand on sustainable energy, in particular energy harvested from sunlight. The energy needs of the planet will at least double within the next fifty years, with global power consumption expected to increase to 28 TW [1]. Currently, 85% of global power is obtained from CO<sub>2</sub> emitting fossil fuels. The state is set for a major shortage of energy supply unless renewable sources can cover the substantial deficit that fossil fuels can longer furnish. The supply of energy from the sun to the earth is enormous, amounting to  $3 \cdot 10^{24}$  J/year, equivalent to 10<sup>4</sup> times the current consumption today [2]. In crude statistical standpoint, this amounts to 0.1 % of the earth's surface with solar cells with nominal efficiency of 10%, would meet the current needs.

Photovoltaic is a promising renewable energy technology that converts sunlight to electricity, with broad potential to contribute significantly to solving the future energy problem that humanity faces. The current worldwide photovoltaic production was more than 5 GW in 2009, and is expected to rise above 20 GW by 2015 [3]. Photovoltaic could thus make a considerable contribution to solving the energy problem that our society faces in the next generation. To make power from photovoltaics competitive with fossil-fuel technologies, the cost needs to be reduced by a factor of 2-5. It is from this standpoint, to meet the energy needs and find sustainable resources of energy, substantial effort in research and commercialization of photovoltaics has reached a critical stage.

## 1.2 Current Solar Cells

To date, semiconductor solar cells dominate commercial markets, with crystalline Silicon (Si) having an 80% share; the remaining 20% is mostly thin-film solar technology, such as CdTe and CuIn<sub>1-x</sub>Ga<sub>x</sub>Se<sub>2</sub><sup>1</sup>. The conventional Silicon solar cell is an indirect band gap material typically requiring thick (100 – 400 μm) absorption layer, all requiring complicated manufacturing equipment and costly silicon fabrication processing, primarily in the purification process for silicon. It is the core commercial cell for industrial and household usage. This brand of solar cells has been growing and profiting from the experience and material availability resulting from the semiconductor industry. Bringing conventional photovoltaics to the market is mainly limited by the high cost of manufacturing processes. Currently, the first-generation solar cells based on crystalline silicon have achieved certified laboratory efficiencies of 25 % and module

efficiencies around 13-14 % [33]. However high quality silicon is extremely expensive, reaching production cost of about \$3/Watt [4].

Because of this demand to reduce cost, there is a great deal of interest in thin-film solar cells. Thin-film solar cells are made from a variety of semiconductors including amorphous and polycrystalline Si, Gallium Arsenide, CdTe, and CuInSe<sub>2</sub>, as well as organic semiconductors. The film thickens in the range of 1-2 microns, which can be deposited on cheap module-sized substrates such as glass plastic, or stainless steel. A limitation in all thin-film solar cell technologies is that absorbance of near-bandgap light is small, in particular for the indirect bandgap semiconductor Si. Therefore, structuring the thin-film solar cell so that light is trapped inside to increase absorbance is very important. Thin film solar technology such as CIGS (Copper, Indium, Gallium, Selenium) and CdTe/CdSe all contain elements that are toxic and in low abundance in the earth's crust, an industry that will surely face resource restraints in their potential. However CuIn<sub>1-x</sub>Ga<sub>x</sub>Se<sub>2</sub> forms the best performing thin-film solar devices, exhibiting an efficiency of 20%, but is more than 1.4 times as expensive as CdTe and amorphous Si. CIGS efficiency values are  $19.6 \pm 0.6\%$ , CdTe  $16.7 \pm 0.5\%$ , and organic bulk heterojunction is  $8.3 \pm 0.3\%$ , all of which are for cell that are 1 cm<sup>2</sup> in area [5].

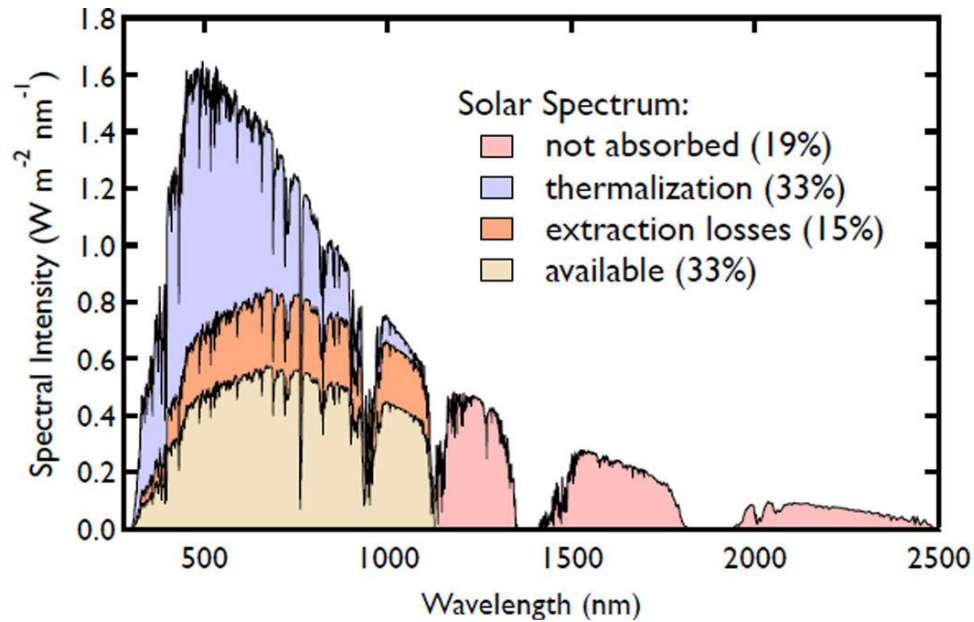


**Figure 1.1** - Minimum Losses for Si Cell ( $E_g = 1.1\text{eV}$ ) and where they occur in the solar spectrum (top line). These are the losses accounted for in the Shockley-Queisser limit and represent an upper limit for solar cells made from single-junction bulk crystalline semiconductors. Thermalization represents the largest loss in this estimate, and it increases for the bluer portions of the solar spectrum [6].

However, for both the first and second generation solar cells, the maximum theoretical efficiency is limited to 31%. This limitation is known as the Shockley-Queisser limit, due to a single p-n junction [7]. This limitation occurs when an absorbed photon generates an electron-hole pair, while all other photon with excess energy is wasted in thermodynamic processes. These losses are highlighted in Figure 1.1, and current silicon solar cells can only account for 33% of the spectral intensity available.

This limitation can be overcome by using multiple junction photovoltaics that rely on various third-generation solar cells, including nanocrystals dye sensitized solar cell, polymer hybrid cells, quantum dot solar cells, and plasmonic solar cells. These emerging solar cell technologies have undergone decades of research to ones that are less than a decade old. These technologies are all motivated by two parameters: (1) reducing the cost of solar cells by depositing inexpensive semiconductors onto inexpensive substrates, (2) increasing the efficiency by harvesting more of the solar spectrum. The National Renewable Energy Laboratory, United States main institution to support renewable energy research and procurement, tabulates the various solar cell technologies and their progress as shown in Figure 1.2. Hence, the fabrication of cost-efficient multiple junction solar devices with remarkably high efficiency should be the direction and objective of photovoltaic research.

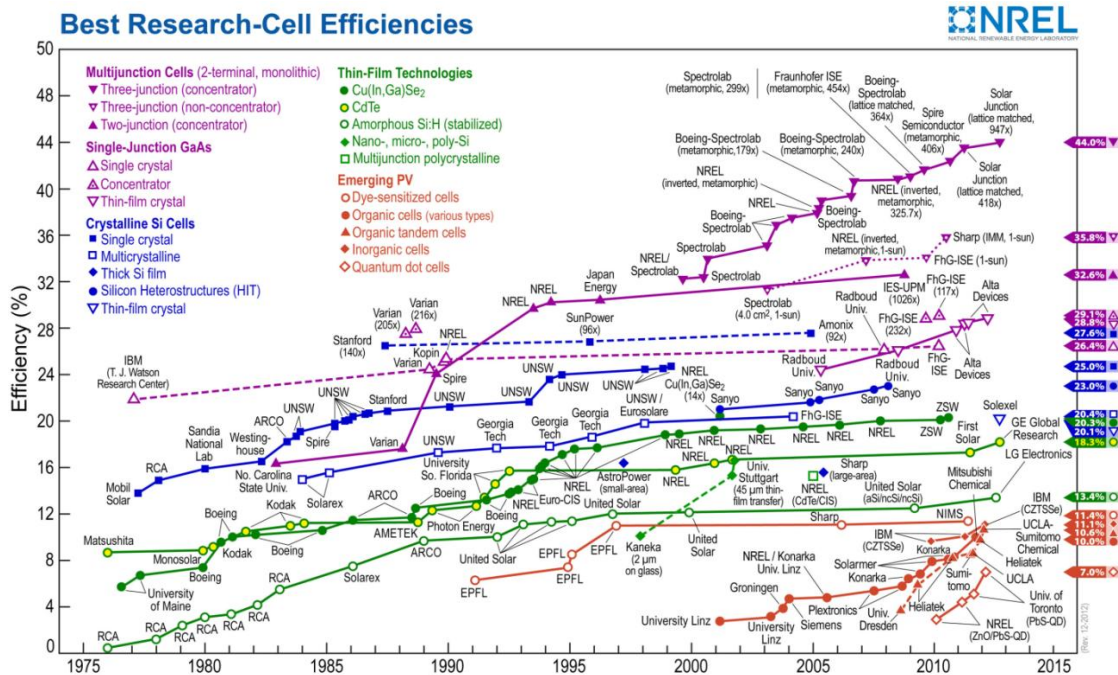


Figure 1.2 - Research solar cell efficiencies by type (Source: NREL).

### 1.3 Dye Sensitized Solar Cell

#### 1.3.1 History and Concept

A low- cost and environmentally friendly alternative to conventional Si solid-state devices is the dye-sensitized solar cell (DSSC). DSSCs are a class of photoelectrochemical cells, which converts solar light to electric energy. It is inexpensive to prepare, and the light-weight thin-film structures are compatible with automated manufacturing and thus potentially has easy scaling possibilities. Its immediate advantages are low production cost, easy scale-up, good performance under weak/diffuse light, and compatibility with building window glass and on flexible substrates. Therefore, DSSCs have been placed as one of the promising alternatives to bulk silicon-based solar cell

The history of dye sensitization dates back to the photosensitization phenomenon by organic dyes first reported in 1887. It is an interesting convergence of photography and photo-electrochemistry, both of which rely on photo-induced charge separation at the liquid-solid interface. Its conceptual rebirth was not until 1991 by Micheal Grätzel, who carried out a milestone research and invented the current structure of DSSC. The breakthrough made in Grätzel 's cell is the introduction of  $\text{TiO}_2$  nanoparticle based photoanode with extremely high surface area. A thin layer of photoactive dyes is coated on the surface of the  $\text{TiO}_2$  porous film that preferentially collects the photogenerated electrons from the dyes. The energy conversation efficiency of the first Grätzel's cell is 7.1% under standard testing conditions [8]. For the last two decades since his initial research, DSSCs have been extensively studied, which covers the areas of fundamental condensed matter physics, device operating mechanics, material innovation, and novel structure design.

A major difference of DSSCs from other semiconductor solar cells are that solar light is not mainly absorbed by the semiconductor, and that the electron-hole pair is separated not at the built-in-potential of a p-n junction. The twenty years since the publication of the much-cited 1991 *Nature* paper entitled "A Low-Cost, High-Efficiency Solar Cell Based on Dye-Sensitized Colloidal  $\text{TiO}_2$  Films" by O' Regan and Grätzel [8]. DSSC based on nanocrystalline semiconductors such as  $\text{TiO}_2$  are of great interest as an alternative to the conventional solar cells because of their high performance, low-cost production, and environmental advantages. They have seen the annual publication rate of papers dealing with various aspects of DSSC rise exponential, with around 1000 papers published in the year 2010 alone [9]. It has



been the subject of substantial academic and commercial research over the last 20 years, motivated by their potential as a low-cost solar energy conversion technology.

### 1.3.2 Operating Principles

The DSSCs consist of dye molecule coated to a wide bandgap semiconductor layer, electrolyte, and transparent conduction oxide (TCO) film. When these cells are exposed to solar irradiation, an incident photon creates a bound electron-hole pair. A broad band component of the solar light generates electron-hole pairs in the dye sensitizer which anchors itself on the photoanode of wide bandgap semiconductor nanoparticles. When the electron-hole pairs are formed in the dye molecules, they are quickly separated at the picosecond scale due to the difference in energy levels. Electrons are injected from the dye to the conduction band of the photoanode, and are transferred to the transparent conduction oxide film that is coated on glass (could also be coated on polymer substrates). In this structure, the maximum output voltage is the difference between Fermi energy of the semiconductor film and the redox potential of the electrolyte.

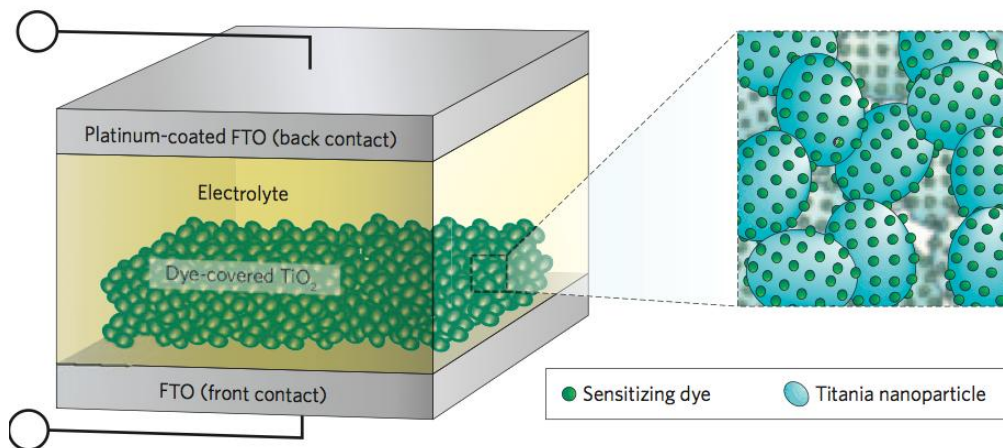


**Figure 1.3** – The sandwich configuration of a dye sensitized solar cell [10].

Traditional DSSCs are constructed in a sandwich configuration, as shown in Figure 1.3. The working electrode is nanocrystalline semiconductor deposited onto a transparent conductive oxide (TCO). In contrast to the conventional systems where the semiconductor assumes both the task of light absorption and charge carrier transport, the two functions are separated here. Light is absorbed by a sensitizer, which is anchored to the surface of a wide band gap semiconductor; primarily  $\text{TiO}_2$ ,  $\text{ZnO}$ , and  $\text{SnO}_2$  are the preferred compounds. Charge separation takes place at the interface between the two materials via photo-induced electron injection from the dye into the conduction band of the solid. Carriers are transported in the conduction band of the semiconductor to the charge collector, usually the TCO.

The nanocrystalline film has mesoscopic pores that are filled by a mediator such as a redox couple. The photosensitive dye is chemisorbed into the semiconductor surface in order to capture the light. The counter electrode (CE) is made of TCO coated glass, either processed chemically or physical sputtered with thin layer of platinum. Platinum serve to catalyze the regeneration process of the redox couple. The CE is separated from the working electrode (WE) by a thin spacer.

The working principle behind the DSSC operation is as follows. As light is illuminated onto the cell, a photon is absorbed by a dye molecule. Next, photoexcitation occurs when the dye is energetically promoted to its excited state. The excitation results in an ultrafast injection of an electron into the conduction band of the semiconductor, producing an oxidized dye. The electron then transports through the network of  $\text{TiO}_2$  (or  $\text{ZnO}$ ) to the collecting anode where it flows into the external circuit allowing energy utilization by a load. Concurrently, the oxidized dye is reduce to its ground state by the redox species present in the electrolyte, which is usually an iodide ( $\text{I}^-$ )/triiodide( $\text{I}_3^-$ ). Iodide reduces the oxidized dye to form an intermediate ionic species (such as  $\text{I}_2^-$ ), that then disproportionates to form triiodide and diffuses to the counter-electrode, providing two electrons per molecule, as shown in Fig. 1.4 [10]. The regeneration cycle of iodide by triiodide takes place at the platinum catalysts-coated cathode [11]. The slow recombination and relatively fast dye regeneration rates of the  $\text{I}^-/\text{I}_3^-$  redox couple have resulted in near-unity internal quantum efficiencies for a large number of dyes, providing the high external quantum efficiencies.

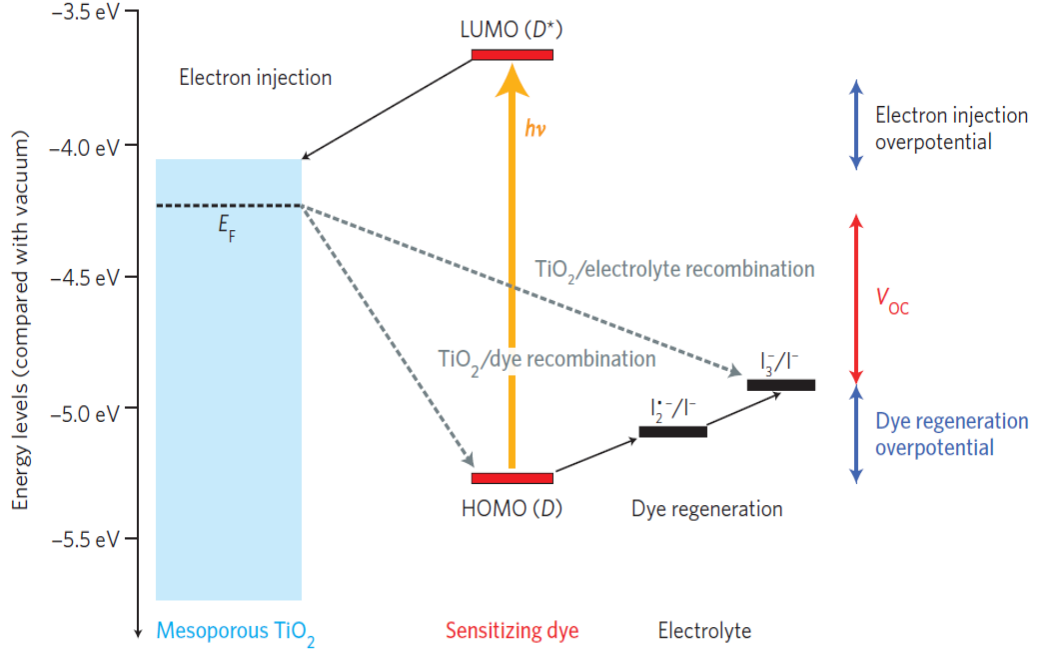


**Figure 1.4** – Dye-sensitized solar cell device schematic and operation. Energy level and device operation of DSCs; the sensitizing dye absorbs a photon (energy  $h\nu$ ), the electron is injected into the conduction band of the metal oxide ( $\text{TiO}_2$ ) and travels to the working electrode (WE, not shown). The oxidized dye is reduced by the electrolyte, which is regenerated at the counter-electrode (not shown) to complete the circuit [10].

Overall, this system generated electron power from sunlight without exhibiting any permanent chemical changes, allowing for DSSC to be practical source of renewable energy.

### 1.3.3 Device Fundamentals

The most important functions of the DSSCs in converting solar energy to electricity are the conversion of the photons to carriers and the transport of photogenerated carriers through the device. Therefore, the yield of electron at a given wavelength for DSSCs can be expressed as:

$$(1.1) \quad n(\lambda) = LHE(\lambda) \cdot \phi_{inj} \cdot \eta_e$$

LHE is the light harvesting efficiency; the fraction of the incident photons absorbed by the dye,  $\phi_{inj}$  is the quantum yield for charge injection, and  $\eta_e$  is the efficiency of collecting the injected charge at the back contact.

A factor associated with the light harvesting of DSSC are that given the dye coated on the mesoporous semiconductor film mainly absorbs the visible solar spectrum. The yield of the electric current for the illumination from the photoelectrode is approximated as follows:

$$(1.2) \quad n(\lambda) = (1 - R)(1 - 10^{\Gamma \varepsilon}) \cdot \phi_{inj} \cdot \eta$$

where  $R$  is the reflectance from the surface,  $\Gamma$  is the monolayer coverage of the dye, and  $\varepsilon$  is the extinction coefficient of the dye. We know that  $\varepsilon$  depends on the incoming wavelength. This extinction coefficient is not constantly high over the range of the spectrum; therefore even most efficiency dye of DSSCs absorbs only part of the solar spectrum. Therefore, LHE of DSSC is not uniform in the visible range of the solar spectrum. The charge collection efficiency can also be expressed as a ratio between the number of charge carriers generated (electron or holes) in the external circuit [12].

$$(1.3) \quad \eta_{col} = \frac{\tau_{rec}}{\tau_{rec} + \tau_{tr}}$$

Where  $\tau_{rec}$  and  $\tau_{tr}$  are the lifetime and transport time of charge carriers respectively. The collection efficiency is typically discussed in terms of the diffusion length, which represents the average distance that carriers can travel in the material. For the case of linear recombination kinetics, this is shown to be equal to

$$(1.4) \quad L = (D\tau_{rec})^{1/2}$$

where  $D$  is the diffusion coefficient. Hence the longer the  $L$ , the larger the probability of collecting charges in the external contact. Both equations show that good collection efficient arises from a balance of fast transport and slow recombination. This effect is primarily sought after in 1D nanostructures to accelerate transport and/or minimize recombination.

The energy diagram in Figure 1.4 shows a typical DSSC configuration that governs the efficiency of the device. The electrochemical potential for electrons in a semiconductor on the energy diagram is known as

the Fermi level,  $E_F$ . However, in an electrolyte solution, this potential energy is often referred to as the redox potential,  $E_{\text{redox}}$ . The energy levels of the dye are described on the basis of highest occupied molecular orbital (HOMO) and lowest occupied molecular orbital (LUMO) levels.

The difference between these two states (HOMO/LUMO) governs the harvesting of incoming light. The optical gap of commonly used Ruthenium-based dyes is about 1.85 eV [13], allowing the dye to absorb light to 700 nm. In order to extend the light absorption, one can narrow the optical gap by raising the HOMO level or lowering the LUMO level. However, photo-induced charge separation first occurs at the interface of the photoanode/dye. Efficient charge separation requires the dye's excited state (HOMO) to be lower in electrochemical potential than the conduction band of the semiconductor [15]. This indicates that the LUMO level has to be higher than the electrode conduction band edge. Similarly, restoration of the dye by redox coupling requires the dye cation (ground state) to be more oxidizing than the redox. Thus modifying these levels has been suggested in order to increase light absorption [15], however remain a challenge in optimizing the energetics of DSSCs. Therefore it is essential in understanding the energetics of the components within the DSSC, and thus suitable anode, dye, and electrolyte must be carefully chosen to achieve an efficient functional device.

#### 1.3.4 Kinetics

The complexities of distinct material components including oxide nanostructure, a molecule sensitizer dye, and redox electrolyte, all of which exhibit complex interactions with each other become difficult to fully explain. In particular, the electrolyte alone is chemically complex, including only a redox couple, but also a range of additional additives found empirically to enhance device performance. These interactions are also modulated by solar irradiation, and thus device function properties change with flux of photons.

There are four competing mechanisms, or electrochemical kinetics, that is continuously under operation during illumination: injection, regeneration, reduction, and recombination. Regeneration is in competition with reduction of the oxidized dye by an electron from  $\text{TiO}_2$ . This process is preferred on thermodynamic grounds, as electrons prefer a back reaction with the oxidized sensitizer. This is undesirable because, instead of electrical current, it merely generates heat. Recombination is anointed to when electrons, during

their transport in the photoanode, are transferred back to the oxidized species in the electrolyte or to the oxidized dye.

Once a photoexcited dye injects an electron, the dye needs to regenerate itself to an excited state in order for it to be capable of injecting once again, a process known as regeneration. This is the aforementioned kinetically challenging step. The key rate requirement at this step is that the dye be regenerated by the electrolyte, before it is 'regenerated' by an electron from the  $\text{TiO}_2$  resulting in no net photocurrent (referred to as electron dye recombination, EDR) [10]. Because the nature of the iodide/tri-iodide redox couple, the regeneration reaction is complex, and the rate constant is several orders of magnitude lower than the diffusion-controlled limit.

Extensive studies of electron injection process, in common  $\text{TiO}_2$ /ruthenium dye films coated in inert solvent have shown sub-picosecond injection dynamics [16], an order of magnitude faster than the competing process of excited state decay to ground. This electron-transfer process with such a high rate can be rationalized in terms of a strong electronic coupling and of the large density of acceptor states in the semiconductor. Therefore, electron injection is not considered a factor in limiting device performance. A charge transfer from the excited dye into the conduction band is resolved on a femtosecond-picosecond time scale [17]. These processes all have rate that has been extensively studied, as highlighted in Figure 1.5.

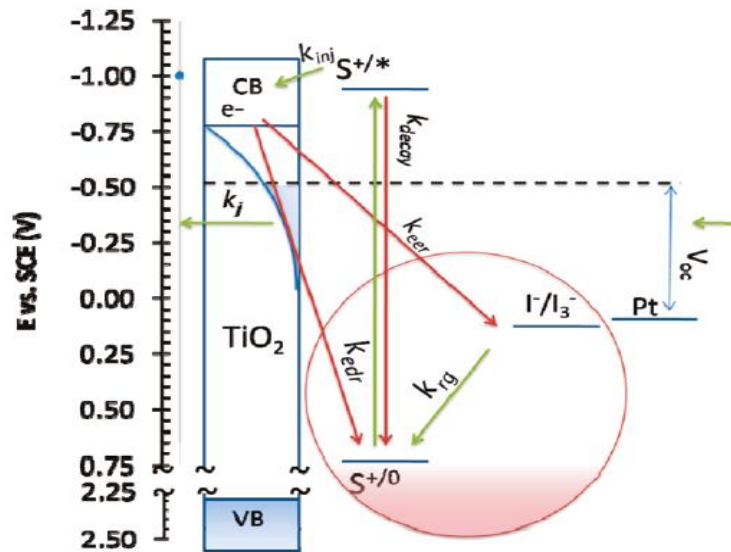


**Figure 1.5** – Energetic and kinetic relationships in DSSCs. The rate  $k_i$ , which refers to electron transfer, is in competition with  $k_{edr}$  and  $k_{eer}$  referred to as recombination [17].

Regeneration reaction with the iodide/tri-iodide couple is complex, and the rate constant is several orders magnitude lower than the diffusion-controlled limit. Usually the reduction of the dye by the electron in  $\text{TiO}_2$ ,  $k_{\text{inj}}$  is also rather slow. Despite this, there is a large thermodynamic driving force for the regeneration step [18], which is the difference in the oxidation potential of the dye and the electrolyte, energy dissipated as heat during the regeneration reaction and contributes to a major loss in the energy efficiencies of DSSCs. This large driving force, typically  $\geq 600$  mV, is a major impediment to lower band gap dyes which absorb near-infrared light. To reduce the band gap of the dye, either the reduction potential of the LUMO must become less negative, impairing the already optimized injection, and/or the HOMO must become less oxidizing, decreasing the driving for regeneration. This process, an expression of the difference in redox potential is needed to make the regeneration proceed faster than recombination, as highlighted by the overlap in kinetic speeds in Figure 1.6.

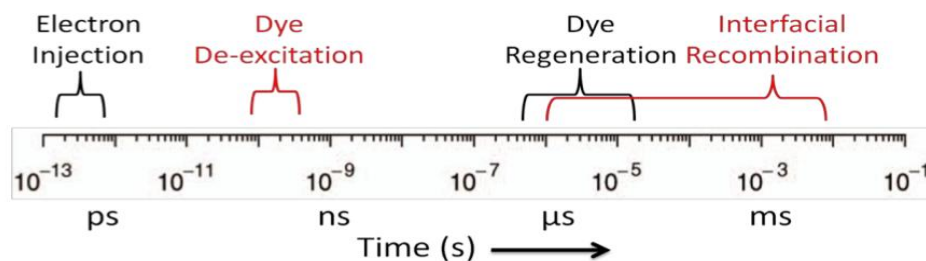


**Figure 1.6** – Kinetic processes and their respective time frame. The main challenge in DSSCs, where efficiency is compromised the most, is during dye regeneration and recombination [19].

### 1.3.5 Material Components

#### 1.3.5.1 Photoanode Semiconductors

The mesoporous oxide layer is the most distinguishing and the most important factor in determining the photovoltaics performance of DSSCs. Its main function is to optimize light harvesting by providing high internal surface area in which dyes are adsorbed. The oxide film holds the dye molecules, collects the photogenerated electron from the LUMO level of the dye molecules, and provides the path for the transport of the electrons to the TCO. Therefore, the oxide materials have to satisfy several requisites: high surface area to load a large amount of dye molecules, conduction band energy level locating between

the LUMO level of the dye and the redox level of the electrolyte, high electron mobility, and chemical stability. To date, anatase  $\text{TiO}_2$  nanoparticles based porous film is known to satisfy these complicated requirements [17].

The inertness of  $\text{TiO}_2$  crystal structure makes it an ideal supporting material for sensitizers that rely on carboxylate groups to attach the dye to the surface [20]. Common polymorphs of  $\text{TiO}_2$  are rutile phase (tetragonal space group,  $E_g \sim 3.05$  eV), an anatase phase (tetragonal,  $E_g \sim 3.23$ ), and a brookite phase (orthorhombic  $E_g \sim 3.26$ ). Among the three phases, the rutile is thermodynamically stable and its bandgap is suitable in absorbing the solar spectrum. However, the rutile phase  $\text{TiO}_2$  is not widely employed in DSSCs due to their high resistivity. Though the anatase phase is irreversibly transformed to the rutile phase at high temperature ( $800^\circ\text{C}$ ), the meta-stable anatase crystal structure can form in the nanoscale regime [21]. The nanostructured anatase is beneficial from the standpoint of its high surface area. The surface area and surface potential of the oxide nanoparticles control the amount of dye adsorbed on the photoanode, which determines the total number of photogenerated carriers. Nanometer sized crystal is important in providing an internal surface area  $\sim 1000$  times larger compared to a flat, non-structured electrode of the same size and thickness [18]. In addition, the anatase phase has higher electric conductivity, higher surface area and therefore can accommodate larger dye loading capability than its rutile counterpart. Its conduction band (CB) is 0.1 eV higher than that of rutile phase, thereby maximizing the potential open circuit voltage ( $V_{oc}$ ). For these primary parameters, is the reason anatase nanoparticle is used as the main component of the Photoanode in DSSCs.

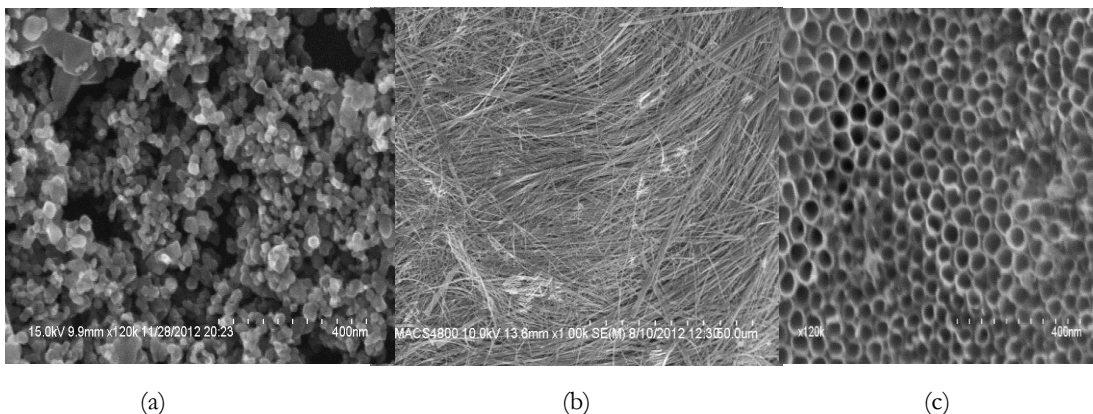


**Figure 1.7** – The photoanode can come in various compositions from nanoparticles (a), nanowires (b), and nanotubes (*Synthesized by Cristina Javier and Robin Young*) (c). Current research also explores double layer film and compositions of particle and one-dimensional structure.



The crystal structure of  $\text{TiO}_2$  has a profound effect on the intrinsic electrical properties of  $\text{TiO}_2$ . One more unique and critical parameter is its non-stoichiometry. The carrier concentration and mobility of this transition metal oxide semiconductor are closely related to the type and concentration of cation and anion defects. Possibly intrinsic point defects in  $\text{TiO}_2$  are oxygen vacancies, titanium interstitial, and titanium vacancies. Oxygen vacancies play a key role in the overall performance of DSSCs. Electron and hole dynamic studies show that vacancies in  $\text{TiO}_2$  surface stabilize dye adsorption [22]. Consequently, strong bond between the dye and the semiconductor promote charge injection, though the oxygen vacancy near the conduction band edge decreases  $V_{\text{OC}}$  and facilitates electron-hole recombination. Oxygen vacancies also have an influence on the relation between electron and redox couple. When the vacancy is present on the surface of  $\text{TiO}_2$ , the HOMO and LUMO of the redox species are shift to higher energy levels and the back-electron transfer becomes more pronounced [23]. These large band-gap oxide films are insulating in the dark; however, a single electron injected in 20nm-sized particles produces an electron concentration of  $2.4 \cdot 10^{17}/\text{cm}^3$ . This corresponds to a specific conductivity of  $1.6 \cdot 10^{-4} \text{ S/cm}$  if a value of  $10^{-4} \text{ cm}^2/\text{s}$  is used as the electron diffusion coefficient [24]. In reality, the situation is more complex because the transport of charge carriers in these films involves trapping unless the Fermi level of the electron is so close to the conduction band that all of the traps are filled and the electrons are moving freely. Therefore, the depth of the traps that participate in the electron motion affects the value of the diffusion coefficient. This is why the diffusion coefficient increases with the light intensity. There is no drift term in electron transport, since the cations in the electrolyte screens the negative charge, eliminating the internal field.

Another role the photoanode can participate is light management. The incorporation of scattering particles voids increases the optical path length, improving the long-wavelength response of the DSC. The treatment of  $\text{TiO}_2$  surface by  $\text{TiCl}_4$  is commonly used procedure to enhance the energy conversion efficiency of DSSCs.  $\text{TiCl}_4$  has the benefit are an increased density of specific binding sites, positive shift in the conduction band edge of  $\text{TiO}_2$ , and overall increased percolating motion of electrons [23]. This treatment allows for an ultra-pure layer lowers the acceptor levels of the surface energy in  $\text{TiO}_2$ , which can improve the charge injection efficiency, as well as increase the dye adsorption due to an increased film roughness.

One could also coat the  $\text{TiO}_2$  nanoparticle with a heterogeneous oxide layer, creating a core-shell structure that can block the back electron transfer [20]. Optical path length in the photoanode can extend the photoresponse of any dye. The ideal porosity of  $\text{TiO}_2$  nanoparticles is suggested to be 50-60% throughout

the film; higher values would lead to a decreased connection between the  $\text{TiO}_2$  particles and reduce the charge collection efficiency [25]. Analysis of the layer morphology shows the porosity to be around 50-65%, the average pore size being 15nm [26].  $\text{TiO}_2$  also has high mobility of n-type carriers as shown by Forro and colleagues [27].

### 1.3.5.2 Multiple $\text{TiO}_2$ Structure

A multilayer  $\text{TiO}_2$  structure can improve response by incorporating light-scattering voids. Normally, a thin  $\text{TiO}_2$  underlayer between the FTO and the porous  $\text{TiO}_2$  layer has been used to reduce recombination [28]. Many researchers have argued that one dimensional structures such as nanowires, nanotubes, and nanorods among other should enhance DSSC performance due to the diffusion of electrons is much quicker. Improvements in trap occupancy, which are electrons occupying in a 'trapped state,' alter the electron diffusion coefficient that incorporate 1D structures [29].

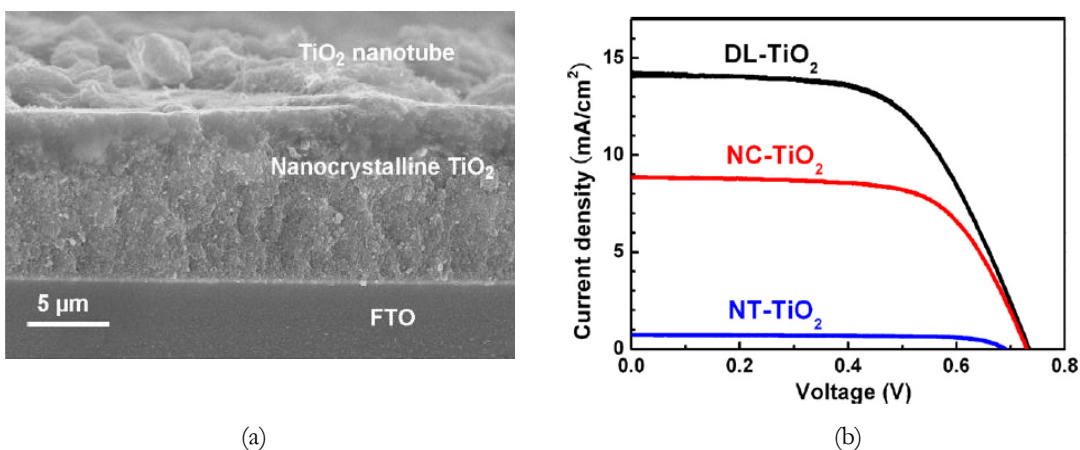


**Figure 1.8** – Tailored microstructure for light harvesting and fast electron transport using two layers (a). The double layer  $\text{TiO}_2$  device shows photovoltaic enhancement, low transfer resistance, and longer electron lifetime [48] (b).

For a double-layer electrode, another thin layer of submicron-sized nanostructures has been shown to give higher photocurrent, primarily attributed to the increased optical path length created by the bottom compact layer, which acts to scatter the incoming photons [30]. An interfacial layer can harvest light as well as create a potential barrier between the conducting FTO and  $\text{TiO}_2$  nanoporous layer. Such films are able to suppress back electron transfer from the FTO and  $\text{TiO}_2$  nanoporous layers to  $\text{I}_2/\text{I}_3$  redox electrolytes without lowering electron injection from the  $\text{TiO}_2$  to FTO [31]. It is now well-accepted that a high-

efficiency photoelectrode for DSSCs requires not only a high surface area for the loading of large amounts of dye molecules but also a tailored microstructure for light harvesting and fast electron transport. To simultaneously satisfy these requirements, much effort has recently been paid to the development of bi-functional oxide film materials, which are composed of a thin surface layer of nanocrystalline particles to effectively adsorb dye molecules and an apparent mesoporous microstructure to confine the incident light within the electrode and/or to enhance the electron conduction.

### 1.3.6 Dye Sensitization

The use of sensitizers offers a key advantage over the traditional harvesting mechanism – the broad absorption band in the dye in conjunction with oxide films of nanocrystalline morphology permits to harvest a large fraction of the sunlight. There are several fundamental features on dyes that should be met accordingly. First, upon excitation, the dye should inject an electron into the photoanode with quantum yield of unity. Most importantly, the energy level of the excited state should be higher than the edge of the conduction band of semiconductor minimizing energetic losses during electron transfer [9]. And lastly, the dye's redox potential should be sufficiently high in order to cause dye regeneration via electron donation from the redox electrolyte or by a hole conductor [13]. Finally, the dye should be photochemically, electrochemically, and thermally stable to sustain years of exposure to light.

Photon absorption by the sensitizer dye (or equivalent inorganic absorber) is the first step in the sequence of process that lead to power generation in the DSSC. The optical absorption properties, coverage of the dye, and optical path length are all parameters that need attention. In contrast to semiconductors that have steep absorption coefficients the onset of the band gap, molecular absorptions bands typical in sensitizing dyes do not exhibit such steep onsets, and N719, the most commonly used ruthenium dye, has an onset around 1.65 eV, not sufficient since NIR harvesting is more desirable. Typical dyes such as N3, N719, C106, and CYC have a fairly broad absorption spectra ( $\Delta\lambda = 350$  nm) but low molar extinction coefficients (10000-20000/M-cm) [32]. Steps to increase the optical path length by some form of light management in the form of scattering or light guiding can offer promising ways to harvest long-range wavelengths.

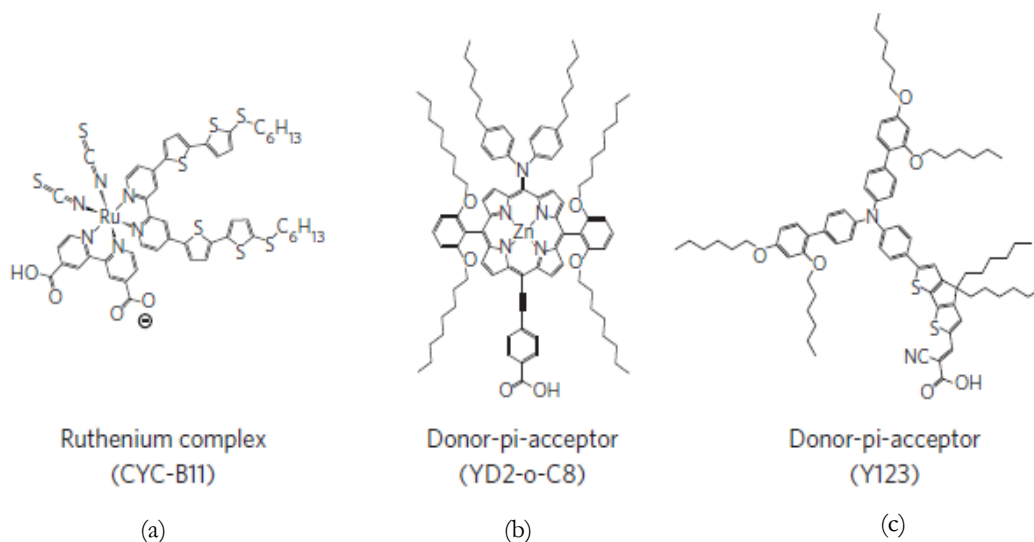


**Figure 1.9** – Chemical structures of the best-performing ruthenium based complex (a), along with donor-pi-acceptor dyes (b, c).

Synthesis and characterization of new have been major preoccupations in recent research. The design of new dyes, specifically tailored to modifying light harvesting is called ‘panchromatic engineering.’ These ‘exotic dyes’ are often tested as a direct replace to improve the response in low-energy part of the spectrum by lowering the HOMO-LUMO gap of the dye without affecting the injection efficiency and regeneration rate. Modifying this gap could conceivably lead to efficiencies that are much higher than current good cells. Electron injection is typically fast in most dye complexes, and therefore higher molar absorption coefficient so that thinner  $\text{TiO}_2$  films can be used, increasing the collection efficiency for electrons [20]. A design issue that needs to be addressed is to structure the dye in such a way that it hinders the contact of electrolyte to the  $\text{TiO}_2$  preventing back electron transfer. The best dyes contain both electron-rich (donor) and electron-poor (acceptor) sections connected through a conjugated  $\pi$  bridge, functionalized with binding groups that couples the molecule to the oxide surface, so as to create a barrier between holes in the redox couple and electrons in the  $\text{TiO}_2$ . It is assumed with confidence that regeneration of the sensitizer dye by the electron transfer iodide ions (or equivalent reduced species) following injection is sufficiently rapid that the back electron transfer from the oxide to the oxidized de can be neglected. This assumptions need to further investigated, and has been shown to be a significant loss mechanism at the maximum power point, where electron density is higher [33].

The motivation in this stems from a number of issues inherent to the use of dyes. A critical component to dyes feasibility in DSSCs is cost. The synthesis and purification of the best performing ruthenium-based dyes is expensive. The terpyridine black dye for example, sells at around \$3500 per gram. Alternative metal-free dyes such as those based on the indoline structure have been widely investigated with performance in competition with ruthenium dyes. Stability and degradation are also concerns in dyes.

An alternative to molecular sensitizers is the use of solid-state sensitizers in the form of small semiconductor particles [34]. A way to engineer a sensitizer that properly addresses the issue of absorption limit is the band gap of certain bulk semiconductors. CdTe ( $E_g = 1.5$ ) and Bi<sub>2</sub>S<sub>3</sub> ( $E_g = 1.25$ ) are two examples that could serve this approach. Constraining the size of semiconductor introduces quantum mechanical phenomena known as quantum confinement. This allows one to tune the band gap so that it falls in the NIR and has the semiconductor properties of high absorption coefficients. However, dyes have the potential to outperform inorganic sensitizers, and therefore careful quantitative analysis can aid in comparing which would work best.

### 1.3.7 Electrolyte Dynamics

The function of the electrolyte is to shuttle charges from the counter electrode to the working electrode while maintaining the ionic conduction between the two electrodes. Dissolved within the electrolyte solution are redox couples, which are used to react at the surface of the counter and working electrodes. Thus, the reactions of the redox species with both electrodes in a desired manner are crucial processes in DSSCs.

In order to achieve a desirable performance, several factors of the electrolyte are considered. First, open-circuit voltage is determined by the difference between the photoanode conduction band level under illumination and the redox Fermi level [35]. Second, the electrolyte should be electrochemically compatible with the dye sensitizer in order to efficiently reduce dye cations [11]. Consecutively, it should not destroy the attachment of the dye on the semiconductor surface or even the electrode material. Lastly, because the redox couple diffuses across the liquid layer and reacts with both electrodes to complete the circuit of the cell, the electrolyte should be chemically stable, have low viscosity in order to minimize electron transport, and have a high boiling point.

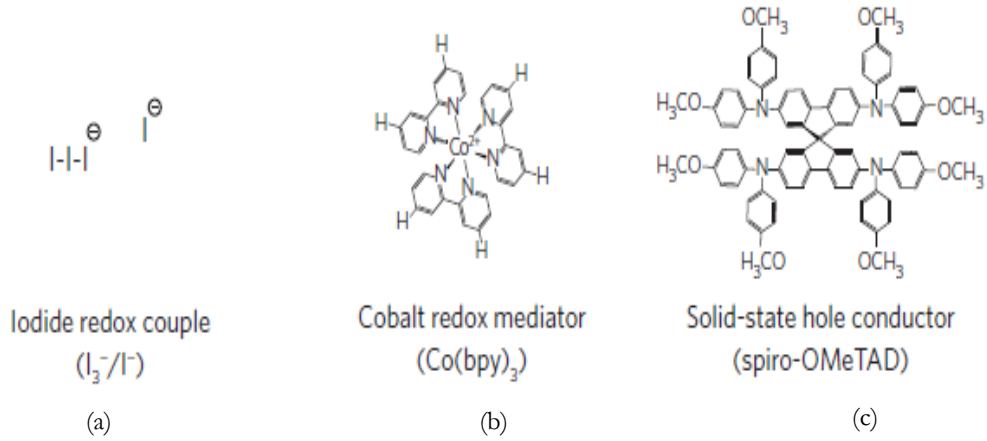


**Figure 1.10** – Chemical structures of the iodide redox couple (a), a cobalt mediator (b), and the solid-state hole conductor spiro-OMeTAD (c).

In order to achieve a desirable performance, several factors of the electrolyte are considered. First, the maximum open-circuit voltage is determined by the difference in the potential between the redox potential in the electrolyte and  $TiO_2$  conduction band [11], as outlined in equation 1.5 and 1.6. Strategies to increase  $V_{OC}$  involve retarding the rate of electron transfer to the oxidized component of the redox couple or shifting the  $TiO_2$  conduction band energy up by adsorption of species that alter the surface dipole. A key process in cell operation is the regeneration of the dye from its oxidized state following electron injection. This involves electron transfer from the redox component of the redox couple. The driving force for this reaction is high, around 0.5 eV in conventional DSSC cells [27]. It is ideal to move the redox level closer to the S+/S (see Figure 1.5 for nomenclature) redox level so as to increase the open-circuit voltage while maintaining rapid regeneration of the dye. This was recently achieved by Grätzel and colleagues by applying an insulating ligand technique to a donor-pi-acceptor dye YD2-o-C8, which has a broad absorption spectrum. In doing so, they achieved low recombination rates and demonstrated world record efficiency of 12.3 % [32]. The improved performance was linked to a 16% increase in  $V_{OC}$  over cells containing an iodide-based redox couple. This effectively demonstrated the effect of tuning the redox potential to increase cell  $V_{OC}$ .

$$(1.5) \quad E_{F,redox} = E_{F,redox}^{0'} - k_b T \ln\left(\frac{C_{ox}}{C_{red}}\right)$$

$$(1.6) \quad V_{OC,theoretical} = E_F^{Anode} - E_{Redox}$$

Some redox electrolytes are capable of fulfilling most of the state criteria, such as halogen systems including  $I^-/I_3^-$ ,  $Br^-/Br_3^-$ ,  $Co^{2+}/Co^{3+}$ , and pseudohalides such as  $SCN^-$ . The most common used for high efficiency device are the iodide-tri-iodide couple as a redox shuttle in organic solvents. Unfortunately this couple exhibits corrosion and energy loss. The main cause of these drawbacks is the over-potential of the iodine [36], discussed in the prior section on kinetics. This has been the motivation focusing DSSC research towards developing an alternative redox couple. Recently, transition metal system, for example the cobalt complex system appears to show promising activity and may be a rival to iodide redox couple [37]. Solid-state hole conductors as alternatives to liquid redox electrolytes.

#### 1.4 Outlook and Commercialization

The ultimate goal of any emerging solar cell technology is to achieve an installed cost-per-watt level that reach grid parity versus conventional fossil fuel technologies and competes favorably against incumbent photovoltaic technologies. Silicon photovoltaic module cost have continue to reduce from \$4/W in 2008 to just \$1.25/W in 2011, with module efficiencies range from 15%-20% and lifetimes guaranteed to 25 years. It is realistic to expect that silicon modules could continue to reduce manufacturing costs around \$0.70/W. Great strides have also been made in the commercialization of thin-film technologies, where CdTe has achieved module efficiencies of 10-12.5% at cost around \$0.70/W and current roadmaps show a reduction in cost. Therefore, competition from DSC will not only depend in the ability to increase power-conversion efficiencies and develop ultralow-cost architecture that is stable over 20 years, but also on market factors such as the overall photovoltaic demand and the scarcity of rare elements. DSSC can be constructed from abundant non-toxic material, which is a significant benefit over thin-film technologies.

The DSSC provides a technically and economically credible alternative concept to present day p-n junction photovoltaics devices. The perspective offered thus far gives a grim future on the progress of DSSCs. However, with all the options available, from quantum dots and multiple exciton generation (MEG), to the use of tandem dyes, various electrolytes, one can be optimistic that progress will be made provided that

Careful thought is given to the motivation for a particular research strategy. An optimal combination of high efficiency, good stability, and low cost will determine the future of DSSCs. Although the present liquid-electrolyte based concept seems to be close to optimal, some technical problems such as hermetic sealing for the liquid, high price of dyes, the platinum counter electrode, and conducting glass still exist to hinder further applications. Many efforts are already underway to address such issues such as developing solid-state electrolytes, organic dyes, and carbon based counter-electrodes. In addition, cells fabricated on lightweight and flexible substrates can employ roll-to-roll coating production lines to reduce processing costs. Increasing module-efficiencies of DSSCs to more than 15 % would create incentive for the path to commercialization. So far, this technology is now being scaled up for commercial applications by several industrial companies such as Konarka (USA), Solarmer (USA), and Heliatek (Germany).

Materials aside, developments in new techniques to better control the kinetic electron transfer processes at the interface needs further understanding and solutions. However, despite intense research efforts, our ability to identify predictive materials and structure/device function and, thus, achieve the rational optimization of material and device designs, remain relatively limited. In addition, the effective environmental friendliness in the fabrication should also be considered, as sometimes toxic solvents and chemicals are used in fabrication.

### **1.5 Thesis Outline, Aims and Objectives**

The objective of my thesis is to provide information that could advance the progress of light harvesting and charge collection in DSSCs. There are two reasonable objectives that could address this narrative: (1) an efficient photoanode for dye loading and electron transport, and (2) co-sensitization of the  $\text{TiO}_2$  photoanode.

The first goal seeks to address the slow charge transport through the nanoparticle matrix. It is known from prior discussion that electrons diffuse slowly through the photoanode film, thereby increasing the probability for recombination with the dye or electrolyte. One-dimensional structures allow easier and faster transport due to electrons moving along in the axial direction with very little electronic scattering. It also serves to scatter incoming light, thereby increasing the optical path length of photons in the film. We



seek to deposit a photoanode that comprises of both nanowires and nanoparticle to take advantages of the mesoporous nature of the nanoparticles, and the fast electron transport of the nanowires.

The second goal seeks to address the problem of DSSCs lack of available sensitizers in the NIR region.

The most commonly used dyes are known to only harvest only the visible part of the spectrum. It is with this shortcoming that we seek to additionally sensitize the  $\text{TiO}_2$  with PbS quantum dots in hopes of harvesting NIR light as well.

Therefore several different devices with different photoanode composition and sensitizers were fabricated and investigated for their photocurrent properties. The morphology of these materials is investigated by scanning electron microscopy and/or transmission electron microscopy. The optical characteristics of the material were characterized by a UV-Vis spectrometer. The structural and physical attributes to the molecular species of the material used were verified by Raman spectroscopy. The electrical resistivity of our films is investigated by the 4-point probe method. And finally, to observe the solar cell characteristics were studied by using a solar simulator.

Chapter 2 of the thesis covers the material used and their specific characteristics. Here we investigate the properties of our material to better enhance device parameters.

Chapter 3 covers the experimental details on how to synthesize, deposit, assemble and characterize a state-of-the-art DSSC. The fabrication method used through the thesis is described in detail, along with the theory and relevant equipment setup for each characterization technique.

Chapter 4 presents the results of our films and device parameters. The surface topology of our photoanode, resistivity, and its compositions are reported. The qualities of CuPc deposition technique, along with the properties of quantum dots grown on nanowires are also reported with extensive focus. And finally, the reasoning behind the different photocurrent of our devices is analyzed.

Chapter 5 serves as a summary of the thesis, and a perspective on possible future research directions are also prepared.

# 2

## Material Properties & Characterization

In this section, we review the materials to be used in this thesis and their properties. We outline the motivation for these materials, and how they can enhance the overall performance of the cell. We then discuss the device energetics of the ones tested in this thesis.

## **2.1 Materials Used**

### **2.1.1 FTO**

One important factor that influences the efficacy of a DSSC is the nature of the transparent substrate and its resistivity. There are mainly two transparent and conduction oxides (TCO) used in DSSCs: indium-doped tin oxide (ITO) and fluorine-doped tin oxide (FTO). There is already substantial discussion on which of these materials influence DSSC performance. However, based on their respective research, it is sometimes ambiguous which TCO is the appropriate for DSSCs. Zumeta's [16] research concluded that a DSSC with photoelectrodes on FTO was more efficient than with photoelectrodes on ITO, while Yoo and colleagues [38] reported that a DSSC with ITO/ATO (antimony-doped tin oxide)/TiO<sub>2</sub> exhibited a better photovoltaic performance than the conventional FTO.

Resistivity of these oxides are fairly low, on comparable with some highly conductive metals such as copper and gold. However, the resistivity increases after subjected to thermal treatment from 18  $\Omega$ /sq to 52  $\Omega$ /sq, while the FTO does not change very much [39]. Therefore, FTO exhibiting proper of lower resistivity, thermal stability, and better adhesion for TiO<sub>2</sub> nanostructures is the main reason for the choosing of this substrate.

### **2.1.2 TiO<sub>2</sub> morphologies**

TiO<sub>2</sub> can be fabricated by sol-gel solution method, hydrothermal method. They exhibit predominant a bipyramidal shape, with exposed facets having (101) orientation, which is the lowest energy surface of anatase. Their size ranges from 5-20 nm.

A short sintering process is usually applied to ensure that the particles are electronically interconnected. To enhance the light—harvesting capacity of the dye-sensitized film in the red or near-infrared region, particles of 200-400 nm radius are either mixed in the film or printed as an over layer on top of the smaller particles [2].

Single-crystalline, one-dimensional nanostructures, such as nanotubes, nanorods, nanobelts and nanowires have stimulated intensive interest because of their unique applications in mesoscopic physics and the fabrication of nanoscale devices. Among these one-dimensional nanostructures, in particular, nanowires

play an important role as both interconnects and active components in fabricating nanoscale electronic and photonic devices [9]. We will use both nanoparticles and nanowires, and a composite of various weight distributions in our photoanode.

### 2.1.3 PbS Quantum Dots

Current conversion efficiencies are limited by low absorbance of dye monolayers and the low efficiencies imposed with it. The use of stronger absorbers such as quantum dots has not led to an increase in efficiency due to the slow hole removal that enhance recombination efficiency and stability of the nanocrystals when iodine-based electrolytes are used [40]. Therefore, new approaches in using relevant sensitizer required the use of more than one absorber in order to match the solar spectrum [41]. Since it is well known that efficient photoinduced charge separation requires direct contact between the absorber and the metal oxide surface [26], it seems that quantum dots are a reasonable candidate to sensitize the photoanode.

However, using more than one sensitizer to extend the spectral response comes at the expense of lower optical density [41]. As long as absorbers are directly attached to the nanoporous oxide, DSSCs should lead to an enhanced optical density and higher overlap with the solar spectrum without damaging the electron collection efficiency. It is the motivation with this concept, knowing well of its limitations, that we use both PbS quantum dots and CuPc as sensitizing agents in our cell. The resulting cells consists of a porous nanowire structure as our photoanode, PbS quantum dots grown directly on the surface of the nanowires *in situ*, and a layer of CuPc particles directly deposited on top.

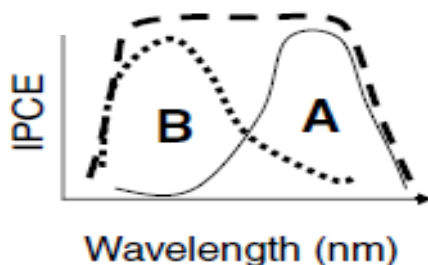


**Figure 2.1** – The idea behind co-sensitization incorporating a dye and quantum dots. Dyes are known to be optically absorbing in the visible spectrum, while small band gap semiconductors, such as PbS, can absorb light in the NIR region, extending the light harvesting potential.

Semiconductor quantum dots composed of lead chalcogenides are unique materials that are ideal for fundamental studies of strongly confined quantum systems. From a technology perspective, lead chalcogenide QDs are of interest because they are among the few materials that can provide tunable band gaps primarily in the NIR region. Fundamental studies of PbS and PbSe QDs are frequently motivated by their intrinsic small Bohr radii ( $a_B$ ), for which PbS is approximately 20nm [43]. This small Bohr radius permits confinement that is not possible for other II-VI or III-V materials<sup>2</sup> for which is nearly equal contribution from electron and hole [43]. This allows for both carriers to be extremely quantum-confined. This extreme confinement of both carriers is the motivation to enhance nearly all of the size-dependent properties that are of interest in dye sensitized solar cells.

One of the current challenges of sensitized solar cells is expanding the light absorption range from the visible to the near-infrared (NIR) region of the solar spectrum in order to maximize the generated photocurrent. Conventional dyes absorption fall in the visible range, and have an absorption coefficient that falls far below. The use of narrow band gap semiconductors such as PbS may expand the light absorption range to the near-infrared region in DSSCs increasing the photocurrent. The absorption region of molecular dyes commonly used in DSSCs is limited to the visible range. Semiconductor materials can absorb all photons with energies higher than their band gap,  $E_g$ , while molecular dyes can only absorb light photons within a more or less broad band corresponding to their molecular transitions. Semiconductors with  $E_g$  in the infrared (IR), such as PbS with  $E_g = 0.41$  eV, have attracted enormous interest as sensitizers because they can allow extension of the absorption band toward the NIR part of the solar spectrum. Bulk semiconductors exhibit three inherent problems: (i) due to its low  $E_g$ , the maximum theoretical efficiency is far below 33% reported for a band gap 1.4eV [44], (ii) its conduction band (CB) is located at lower energy compared to that of  $\text{TiO}_2$ , and therefore electron injection is suppressed, (iii) PbS is not stable with redox couples as iodine or polysulfide. These problems can be avoided by incorporating quantum dots. The first two problems can be circumvented by reducing the size of PbS particles below the Bohr radius, where quantum confinement regime is reached. PbS QDs present higher  $E_g$  than bulk PbS, and also, the energy position of their CB is up-shifted, allowing the fast electron injection into  $\text{TiO}_2$ .

It is well known that nanoscale light absorbers can quickly spate the photogenerated carriers in two different media quickly [45]. However, disagreement exists on the mechanism on the operation for solar cell application. Several authors claim that excitons diffuse to electron or hole extracting interface where they dissociated [46], while other argue that electron and holes are separated by means of Schottky

junction [47]. If quantum dots are strongly coupled, photogenerated excitons may dissociate efficiently, similar to the situation in bulk semiconductors. These strongly coupled QD solids the photoconductivity becomes independent of temperature high photoexcitation densities. This implies that a transition takes place from hopping between localized states to a band-like transport. In such an ‘Anderson Transition,’ the wave functions of electrons and holes become extensively delocalized over the QD solid [48].

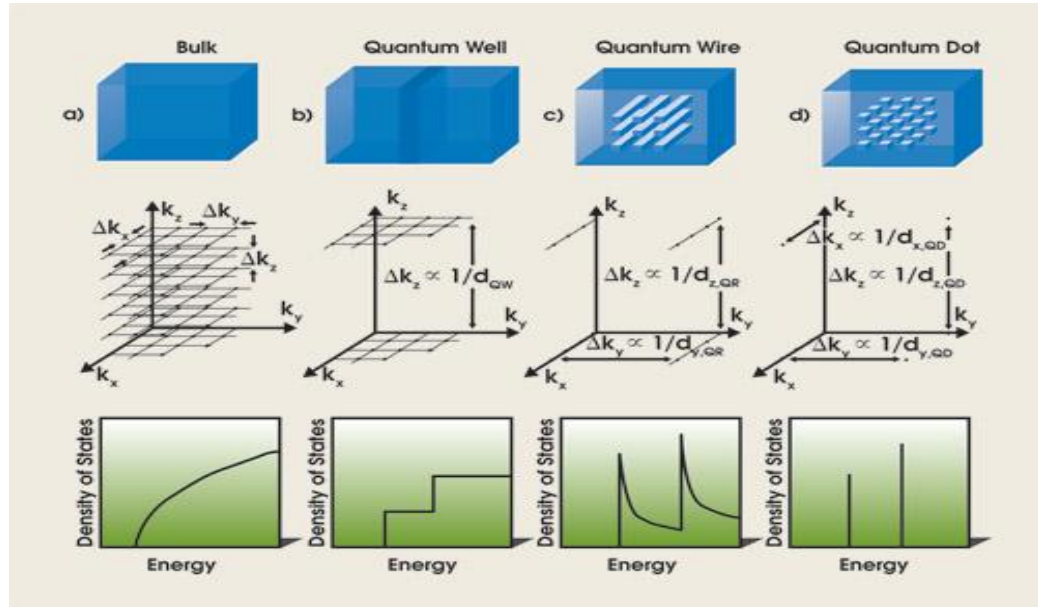


**Figure 2.2** – These graphics represents the material structure (top), allowed states in momentum space (middle, and density of states (bottom) for confinement in no dimensions. Bulk material is confined in no dimensions, while quantum well is confined in 1D, quantum wires in 2D, and quantum dot in 3D [49].

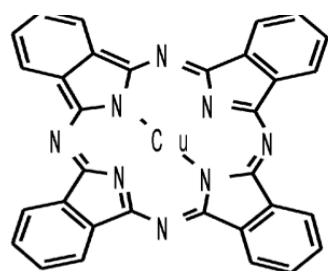
Recently, the use of PbS and PbSe colloidal quantum dots in Schottky solar cells has demonstrated the potential of these materials for solar energy conversion, obtaining remarkably high photocurrents ( $>21$  mA/cm<sup>2</sup>) [50]. It has also recently been shown that films of Pb chalcogenide QDs have produced a record power conversion efficiency of 5.1% [51].

However PbS quantum dots exhibit a nonstable behavior even with ZnS coating as core-shell structure [52]. There is a continual decrease in measured photocurrent in PbS DSSC due to the progressive degradation of PbS, which is reasonably attributed to PbS oxidative process [53]. The fundamental parameter effecting this degradation is the surface termination on the photochemical properties of the QD absorber.

Some other problems inherent to QDSCs is the recombination due to the mesoporous electrode, which the TiO<sub>2</sub> surface remains uncovered is undoubtedly considered as a factor for the high recombination rates. Another problem with inorganic sensitizers such as PbS is that the I<sup>-</sup> /I<sub>3</sub><sup>-</sup> is not suitable because it corrodes the sensitizer. Alternative electrolytes such as polysulfide [54] or cobalt complexes[54] have been used successfully with PbS. However, we intend to use this since this was the only electrolyte available.

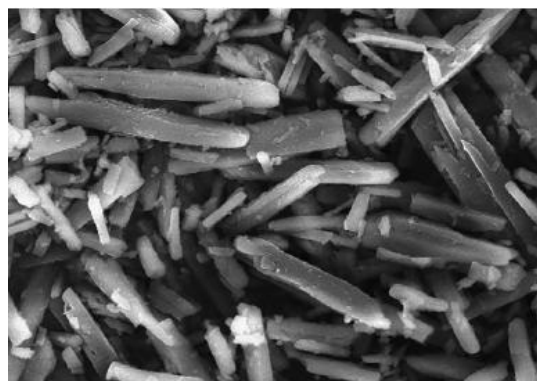
#### 2.1.4 CuPc

Metal-phthalocyanines (MPc) are among the most studied organic molecules in the moving from of organic semiconductors. This class of material has unique properties that are promising candidates for the use in DSSCs: high hole mobility, self-assembling behavior, (3) high conductivity and superconductivity, doping, and chemical stability among others [55]. They have been used in a range of device such as organic light-emitting diodes [56], organic field effect transistors [57], or organic solid-state injection lasers [58]. MPcs are planar fourfold-symmetry molecules characterized by a common electronic structure of the ligand independent from the metal that in the center. Since the molecules of phthalocyanines are similar to the porphyrin groups of chlorophyll and heme, biologically important compounds, phthalocyanines can be used as model object for studies in biochemical physics [59]. In particular, the energy gap in the ligand between the highest occupied molecular orbital (HOMO) and the lowest unoccupied molecular orbital (LUMO) falls in the visible region. The transport energy gap of pure CuPc is  $E_g > 2.1$  eV, with high molar absorption coefficients in the visible region.



**CuPc**

(a)



(b)

**Figure 2.3** – The molecular structure of CuPc, with the Copper atom in the center (a). SEM image of CuPc without any treatment (b).

It has been shown that the Fermi energy of CuPc lies in the middle of a HOMO-LUMO gap, which confirms that CuPc without any impurities could be regarded as an intrinsic semiconductor [55]. However, when CuPc films are deposited, the observation is a more p-type like behavior of CuPc due to the oxygen impurities in the CuPc from the surrounding atmosphere. The pale blue, blue, or blue green color of CuPc suspensions, films, and powders comes from intense 500–800-nm absorption bands, the shape of which is determined by the character of packing of the molecules in the chromophore particles. It is also believed that CuPc in the composite can retard the recombination of photo-generated electron-hole pair of  $\text{TiO}_2$  and can increase the absorption capability in the visible region of the composite. It is believed that in this composite CuPc can retard the recombination of photo-generated electron-hole pair of  $\text{TiO}_2$  and can increase the photovoltaic performance. It is for these properties that CuPc is delegated for loading in  $\text{TiO}_2$ . Due to its exceptional property of stability, cost, and compatibility in the kinetic transfer with  $\text{TiO}_2$ , we use this as the preferred dye for our experiments.



### 2.1.5 Iodine/Iodide Electrolyte

Although scientists have discovered several alternative redox couples that are less corrosive than iodide and whose potential are more suited to achieving high  $V_{OC}$ , solar cells containing such complexes typically have unacceptably high recombination rates, and consequently poor performance (efficiencies of  $< 5\%$ ). One advantage over some new redox couples, such as  $Co^{2+}$  and  $Co^{3+}$ , are surrounded by ligands that can be modified to modulate the redox potential. Bulky groups on these ligands can function as insulating spacers, which slow down the recombination process between the electrolyte and  $TiO_2$  [56]. The main motivation to move away from iodine/iodide complex is to introduce more flexibility in the choice of the redox Fermi level. However, due to the low diffusion coefficients, complex chemistry, and lower photovoltaic performance,  $I^-/I_3^-$  remains the preeminent choice for the electrolyte today, and will be the sole electrolyte in our devices.

### 2.1.6 Pt as Counter Electrode

The counter electrode widely used in DSSCs is constructed of conducting glass substrate coated with Pt films, where the platinum acts as a catalyst. Although this counter electrode has a better performance, it is expensive, and along with the two conducting glass substrates, account for nearly 60% of the total cost in the DSSC [57]. Regardless, platinum was chosen for its ease in deposition, excellent catalytic properties, very low resistivity, and stability in the iodine/iodide redox complex used in this thesis.

## 2.2 Device Architecture

In this section, we outline the electron transport kinetic and energetics unique to our devices. There are two configurations two our device: one in which we use one sensitizer and one device in which we use two sensitizing agents. The purpose of this discussion is to outline electron (and hole transport), and whether co-sensitization using PbS quantum dots and CuPc can co-sensitize  $TiO_2$  enhanced photocurrent.

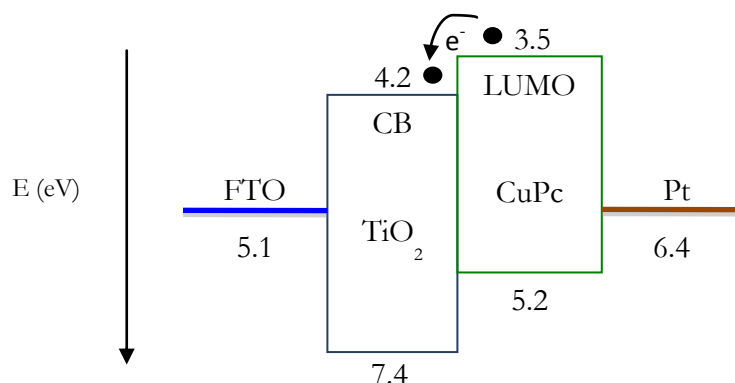


**Figure 2.4** – The band diagram schematic shows a favorable process for electron injection from the CuPc to the TiO<sub>2</sub> photoanode.

### 2.2.1 Single Sensitization

Electron transport is favorable from a lower potential to an increasing potential, while hole transport is from a lower potential to a higher one. Therefore, from Figure 2.4, electrons are transported through a path that is favorable. The transport of injected electrons through the nanoparticle layer is thought to be by diffusion, instead of by drift, due to the macroscopic electric field being negligible across the semiconductor film. The ionic charge present in the electrolyte penetrates to the surface of the nanoparticles and screens the negatively charged electrons in the semiconductor, thus prevent an electrical field build up in the film. Consequently, the gradient of electron concentration, high at the interface of TiO<sub>2</sub>/dye, is the main driving force for this process.

### 2.2.2 Co-Sensitization

In our discussion on dyes, and in particularly CuPc, absorption falls off dramatically in the NIR. To extend the harvesting potential of our cell, we seek to incorporate another sensitizing agent that can extend the absorption range to the NIR. Therefore, quantum dots are an ideal candidate, since the band gap can be tuned based on the diameter the QD. The geometry of the nanoparticle oxide electrode and the diffusion length of electrons in the electrode limit the surface area that can be used for dye molecule adsorption. Due to the small size of QDs, they can easily percolate through the nanoporous electrode without comprising film thickness. It is with this intention of increasing optical density without

compromising other qualities that we present the bi-sensitizer configuration shown in Figure 2.5. This configuration promotes electron injection from both PbS QDs and from CuPc.

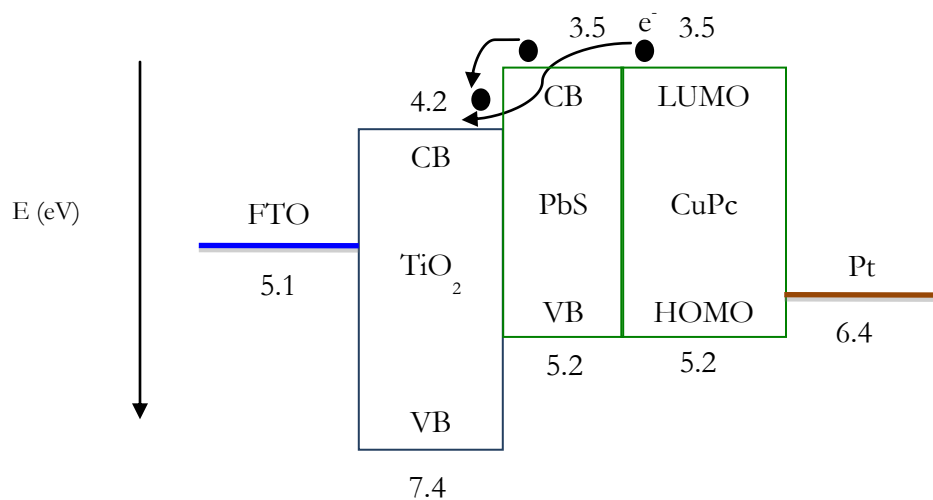


**Figure 2.5** – The band diagram schematic shows a favorable process for electron injection from both the PbS QDs and CuPc. Due to the band structure, hole transport is not favorable.

# 3

## Experimental Procedure and Characterization

### **3.1 Material Synthesis and Electrode Preparation**

This chapter deals with the experimental procedure for material synthesis and device fabrication. DSSCs are prepared and assembled by following a series of steps that include (1) formation of the nanostructure film as a working electrode, (2) dye absorption, (3) preparation of the counter electrode, (4) assembly of the cell into a device, and (5) electrolyte infiltration. This section discusses the materials, fabrication steps, and optimization procedures used in the assembly of a typical  $\text{TiO}_2$  nanoparticle/nanowire based DSSC. Preparation of other semiconductor nanostructure films, TCO microstructure film, and experimental details associated with particular DSSCs are also discussed in Chapter 3.

Before the deposition of the nanostructured film onto the substrate, a suitable TCO must be identified. Since this substrate acts as the final current collector to extract the separated charge carriers from absorbing region, it should meet several criteria to ensure achievement of certain properties. For example, the TCO should be highly transparent to allow maximum light penetration in order to reach the dye molecules in the cell. Furthermore, The TCO should be highly conductive to provide uniform electrical current distribution and minimize the series resistance of the cell. The TCO should also have a good thermal stability at high temperature, specifically during annealing of the photoanode. In order to satisfy these requirements discussed in the previous section, fluorine doped tin oxide was used as the substrate.

We perform several studies on which deposition method effectively address these concerns. Our comparison was based on resistivity of the materials, transmission UV-Vis spectra, thickness, and the overall density of the film.

### **3.1.1 Preparation of FTO/Glass Slides**

1. Each slide was first sonicated in acetone, isopropanol, and DI water for 15 minutes respectively.
2. Use compressed air to quickly dry the surface of the glasses and put them in the oven at 85° C.
3. FTO slides were then exposed to UV Ozone treatment for 5 minutes at 50° C mTorr to allow for better adhesion of the photoanode and to eliminate the residual organic layer on the surface.

### **3.1.2 Preparation of TiO<sub>2</sub> Photoanode**

We have already discussed the use and properties of TiO<sub>2</sub> as the photoanode for our cell, primarily for its porous nature and enormous surface area for dye and quantum dot bonding. There are several common methods employed for coating of the TiO<sub>2</sub> matrix. One such facile method is dip coating and the Langmuir-Blodgett trough deposition. Both techniques are solution based processes that require

the dipping of the sample slide in the solution and the consequent slow withdrawal under specific speeds and conditions to consider.

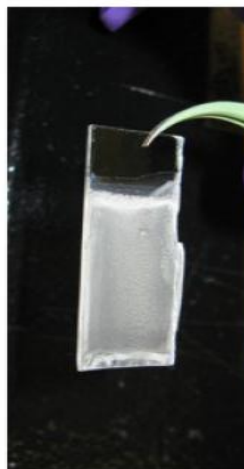
Depositing the nanocrystalline  $\text{TiO}_2$  film requires preparing a basic paste/solution containing commercial  $\text{TiO}_2$  nanopowder with additives, such as acetic acid and polymers, to avoid particle aggregation and to form pores between particles.

Prior to coating the photoanode on the TCO substrate, the glass substrate is masked and defined in a certain area to  $1 \times 1 \text{ cm}^2$  active cell area. The prepared solution or paste is applied and distributed on the FTO slide by doctor blade or screen-printing methods.

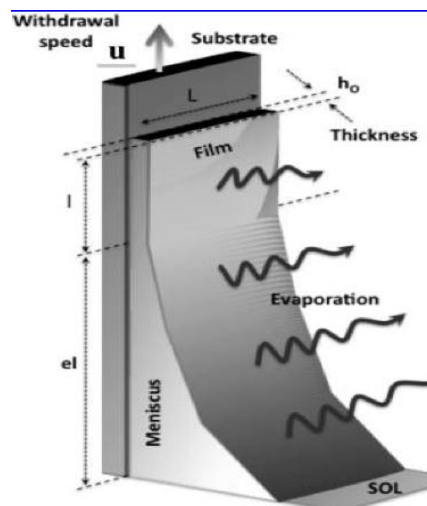
### **3.2.1 Dip Coating of $\text{TiO}_2$ Solution in Isopropanol**

We have prepared proceed for dip coating of ITO and  $\text{TiO}_2$ . The speed is a direct correlation to the thickness of the coating; faster withdrawal giving thicker coats. The excess liquid drains from the surface and solvent readily evaporates from the solution, forming a thin layer. The suspension use for  $\text{TiO}_2$  solutions is as follows:

1. Prepare vials for mixing of isopropanol and  $\text{TiO}_2$  powder to reach a concentration of  $30 \text{ mg/mL}$ . This concentration was chosen for its thorough film coverage and compact nature of the film.
2. The substrate was immersed in the solution at a constant speed of  $1 \text{ mm/min}$ . The speed is kept to a minimum for thinner coating, complete surface coverage, and loading of more particles onto substrate.
3. Once fully immersed, the substrate remained inside the solution for 30 seconds.
4. The thin later deposits itself onto the substrate while it is withdrawn at the same speed.



(a)



(b)

**Figure 3.1** – Dip-coating mechanism (a) and thermally treated  $\text{TiO}_2$  dip-coated film (b).

The resulting thick film is allowed to dry at room temperature in air. The film is then sintered and annealed at  $450^\circ\text{C}$  for 30 minutes in order to remove any organic components and achieve an excellent electrical connection between the  $\text{TiO}_2$  particles. The synthesized single-layer  $\text{TiO}_2$  nanocrystalline film is  $\sim 25\text{ }\mu\text{m}$  thick and contains high porosity which is used as a light absorption layer. The porosity of the film can be controlled by adjusting the amount of polymer additives to the film, however no such treatment was applied on our devices.

The introduction of a compact layer at the interface of the FTO/ $\text{TiO}_2$  has been proven theoretically and practically effective to block electron recombination [60]. This compact layer is far denser than the  $\text{TiO}_2$  layer, preventing the contact between the bare FTO sites and the redox mediator in the electrolyte. This layer would provide adherence between the  $\text{TiO}_2$  layer and the FTO surface, which allows an additional pathway for electrons for efficient electron transfer efficiency. This blocking layer should be nominally 50-100nm thick, can be coated directly onto the substrate by dip coating, spin coating, spray pyrolysis, and sputtering methods. In future research, we intend to use this compact layer.

### 3.2.2 Dr. Blade Method

Doctor blade (or tape casting) is one of the widely used techniques for producing thin films on large area surfaces. Tape casting is a relatively new process, which was originally developed during the 1940's as a method of forming thin sheets of piezoelectric materials and capacitors [61], and is now an accepted precision coating method.

In the doctor blading process, well-mixed slurry consisting of a suspension of ceramic particles along with other additives (such as binders, dispersants or plasticizers) is placed on a substrate beyond the doctor blade. When a constant relative movement is established between the blade and the substrate, the slurry spreads on the substrate to form a thin sheet, which results in a gel-layer upon drying. The doctor blading can operate at speed up to several meters per minute and it is suitable to coat substrate with a very wide range of wet film thicknesses ranging from 20 to several hundred microns.

This kind of doctor blade is also used in combination with a reservoir. The effect of the reservoir geometry on the flow of the sol is described in [62]. The layer is formed by a doctor blade that is either stationary when used with a moving casting surface, or by a frame that moves along a stationary casting surface. The principle is shown in figure below.

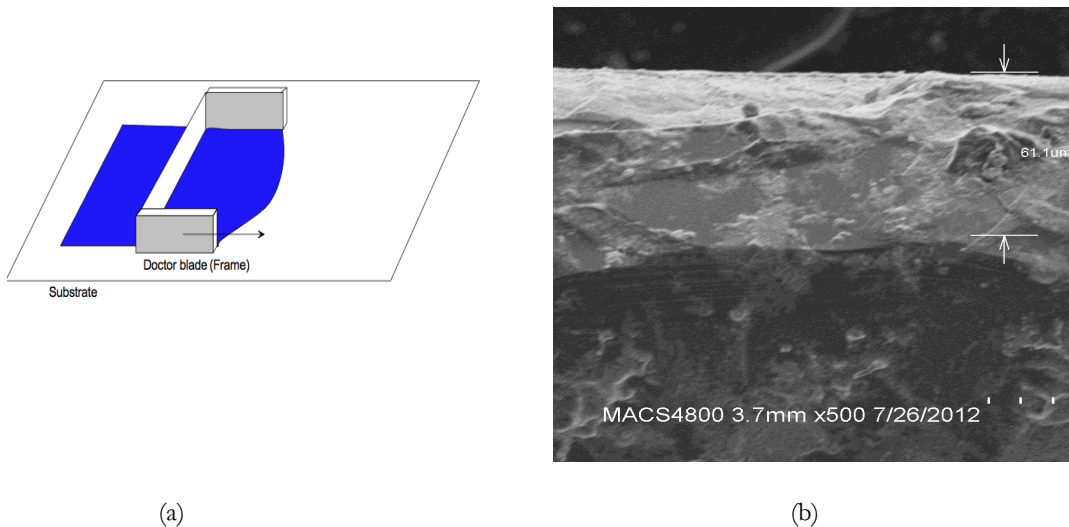


**Figure 3.2** – Dr. Blade technique (a), and a cross-sectional SEM image of the deposited nanoparticle film (b).



The theoretical wet layer thickness corresponds to the height of the doctor blade's edge, or the spiral geometry, respectively. However, the wet layer is sheared during the layer application due to the surface tension of the sol, the wetting behavior and the rheological properties of the sol (dynamic viscosity) and the coating speed. This has the consequence, that the practical wet layer thickness is only 60 to 70 % of the theoretical ones. The final, dried layer thickness of course also depends on the solid content and the densification behavior of the sol.

### 3.2.3 Synthesis of TiO<sub>2</sub> Nanowires

In this work, TiO<sub>2</sub> nanowires were synthesized by a simple hydrothermal reaction with sodium hydroxide, ethanol and commercial P25. The preparation method is convenient, low cost and easily adaptable to mass production. TiO<sub>2</sub> nanowires are known to exhibit excellent electrochemical properties in comparison to nanotubular TiO<sub>2</sub> and nanostructured TiO<sub>2</sub> nanorods [63].

The nanowires were synthesized according to a procedure outlined by Wang [4] and colleagues prepared by a hydrothermal chemical reaction followed by the post-heat treatment at 400° C.

1. Commercial P25 powders (Evonik, Aeroxide P25) of 0.5 g were added into the mixture of absolute ethanol (30 mL) and aqueous NaOH (Sigma Aldrich, 99%) in solution of 30 mL at 10 M.
2. After stirring for 1 hour, the resulting suspension was transferred into a Teflon-lined stainless steel autoclave (150 mL). The autoclave was maintained at 180° C for 24 hours and then naturally cooled to room temperature.
3. Subsequently the obtained precipitates were filtered, washed with HCl (0.1 M) solution and then with DI water until the pH value approaching about 7.0.
4. Finally, the precipitates were dried at 8° C and further annealed at 400° C for 2 hours in air to obtain TiO<sub>2</sub> nanowires.

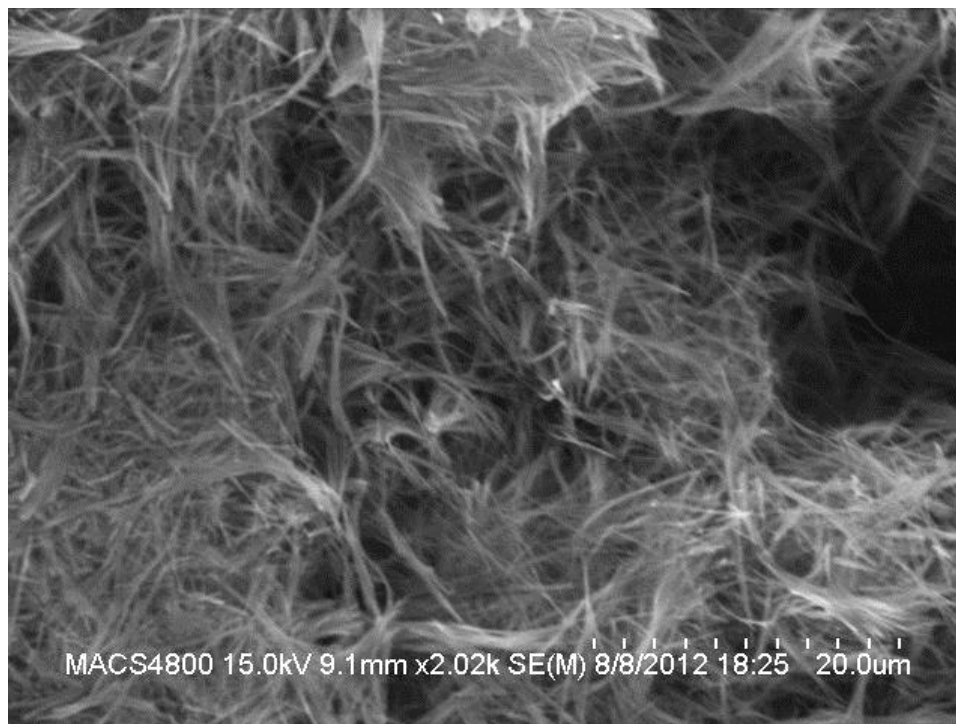


**Figure 3.3** – TiO<sub>2</sub> nanowires after synthesis procedure and thermal treatment. The nanowires have high density and thorough coverage throughout slide.

### 3.2.4 Preparation of TiO<sub>2</sub> Nanoparticle/Nanowire Composite

An objective within this thesis was to test the feasibility of a composite in aiding electron transport while maintaining the high surface area of the photoanode. The rapid electrons transport in the TiO<sub>2</sub> film is important to ensure the efficient collection of electrons by the conducting substrate, in direct competition with kinetic processes such as recombination. When we consider a pure nanoparticle film, for a film with modest thickness of 10  $\mu\text{m}$ , electrons have to pass through more than  $10^6$  particles with various grain and discontinuities in the film to reach the conductive substrate [64]. In the diffusion process, electrons may recombine, typically with the oxidizing species in the electrolyte. In an anatase TiO<sub>2</sub> nanoparticle film, the electron diffusion coefficient is more than two orders of magnitude lower than in single crystals. Due to the high crystallinity order of nanowires, we can improve the order of grain boundaries in the film by incorporating TiO<sub>2</sub> nanowires morphology, which are preferable to electrons

transport, since electronic scattering is reduced due to a higher crystallinity order [65]. It is known that nanowires can also scatter light and thus enhance the light harvest as reported by Tan *et al* [66].

Since the nanoparticle size are on the order of 10-20 nm, which are smaller than the wavelength of incoming light, thus light goes through the film without much scattering. If larger particles were used in a double-layer film, it is sensible that this would scatter light more preferentially. Nanowires have the same affect; therefore a double layer nanoparticle film is omitted in this work. A mixed film can represent a very versatile structure that includes advantages of both: high surface area and fast electron transport.

Three composites by weight ratios of nanoparticle (NP) and nanowire were mixed: (1) 80 % wt. NP and 20% NW wt., (2) 50% wt. NP and 50% NW wt., and (3) 20% NP wt and 80% NW wt. All solutions were mixed in isopropanol. Each suspension was sonicated for 1 hour. Prior to deposition by Dr. Blade method, they were magnetically stirred for 30 minutes since the higher concentrations of nanowires cause the solution to be viscous.

### 3.3 Preparation of CuPc Suspension

Copper (II) phthalocyanine (Sigma Aldrich, 99.5 %) was processed in two solutions based process: one in which the crystal grains were mixed with chloroform to create a suspension, and one in which CuPc readily dissolves in highly concentrated sulfuric acid. CuPc has a very low solubility in organic solvents where as it easily soluble in sulfuric acid due to the protonation of the nitrogen atoms bridging the pyrrole rings. It was initially suggested to try mixing the dissolved solutions, one which CuPc grains are in its smallest constituents, with the TiO<sub>2</sub> nanostructure. However, this results in two features: (1) the TiO<sub>2</sub> surface becomes damaged, and large cracks in the film are observed.

1. .01 M CuPc in 10 mL of Chloroform (Sigma Aldrich, 99.9%): the initial mixing of CuPc into chloroform did not create and observable interaction. Chloroform does not dissolve the large crystals into individual molecules, but instead breaks the crystal grains down to its smallest components, limiting us to 1-10um. The dispersion was ultrasonicated for two hours, in which the only noticeable change to the chemical complexation, but was only physical. The suspension turned from a light blue to an opaque dark navy blue color after the completion of the sonication.

An attempt to heat the chloroform to 60° C to see if it has any chance of dissolving, but doesn't. Chloroform has a boiling point of 80° degrees; therefore temperature did not make any difference.

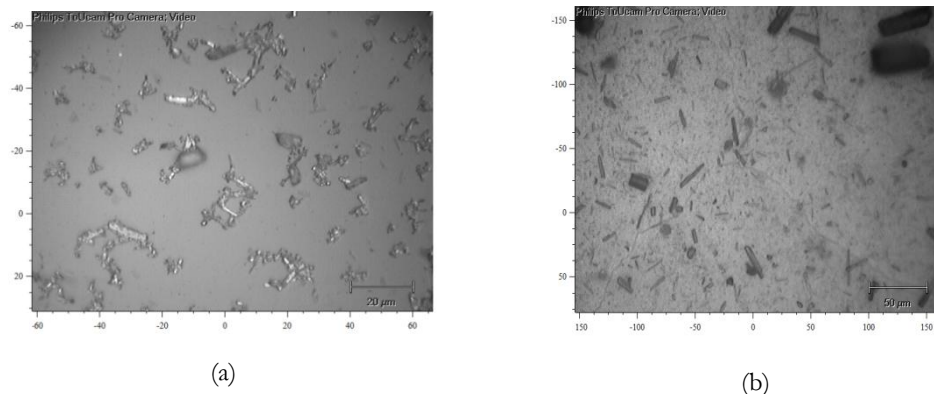


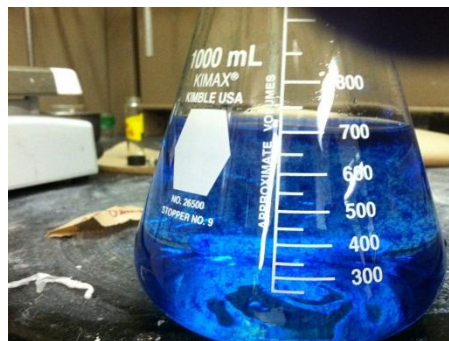
**Figure 3.4** – CuPc particles distributed in solution of Chloroform (a). The particles do not aggregate significantly, and the size distribution ranges from ~ 800 nm to 10 µm (b).

2. .01 M CuPc in 10 mL of H<sub>2</sub>SO<sub>4</sub>(Sigma Aldrich, 99.99%) – It is known that sulfuric acid reacts strongly with CuPc, and the color from the solution turned from a transparent to opaque and then to very dark-violet immediately – a consequence of the protonation of the nitrogen atoms to the H<sub>2</sub>SO<sub>4</sub>. The solution was then ultrasonicated for 2 hours. The procedure is according to Wang and colleagues [67].
  - a. Dissolve 10mg CuPc in 20g concentrated H<sub>2</sub>SO<sub>4</sub>.
  - b. After 24 hours, we add the CuPc/H<sub>2</sub>SO<sub>4</sub> mixture drop by drop into 700 mL DI water with constant magnetic stirring at 3° C. With the decrease of the concentration of H<sub>2</sub>SO<sub>4</sub>, CuPc will precipitate. The low temperature will increase the precipitation rate.
  - c. Filter the suspension liquid and collect the CuPc nanoparticles by firstly washing with water until pH=5, and with acetone to eliminate the residue water finally.
  - d. Dry the CuPc nanoparticles with compressed air.
  - e. Add 1/3 CuPc nanoparticles (~3 mg) into 50 mL toluene, and put it in the ultrasonic water bath for half an hour.

f. Deposit the CuPc nanoparticles on top of the dye coated TiO<sub>2</sub> by spray coating.



(a)



(b)

**Figure 3.5** - CuPc as a suspension in Chloroform (a) and CuPc precipitating in H<sub>2</sub>SO<sub>4</sub> (b).

### 3.3 Synthesis of PbS Quantum Dots *in situ* on TiO<sub>2</sub> Nanowires

The synthesis of PbS quantum dots is a modified procedure from Ratanatawanate and co-workers originally outlined for synthesis of PbS quantum dots on TiO<sub>2</sub> nanotubes. Their procedure is slightly modified for growth on TiO<sub>2</sub> nanowires. One-dimensional structures offer the possibility to control the size PbS QDs by encapsulation on the surface of the nanowires, which have a fixed diameter. The size of the quantum dots is correlated to the concentration of thiolactic acid, however this claim is yet to be conclusive.

- a. To prevent formation of bulk PbS, the TiO<sub>2</sub> nanowires were first treated with 0.5 M of thiolactic acid (Sigma Aldrich, 99.5%) for 30 minutes with thiolactic acid (pH=1), which provides a binding site for Pb<sup>2+</sup> ions.
- b. After 15 minutes of drying at 60 °C and washed with DI water, the nanowires were then treated in 0.2 M aqueous solution of Lead (II) Nitrate (PbNO<sub>3</sub>, Sigma Aldrich, 99.9%) to allow Pb<sup>2+</sup> ions to adsorb onto the nanowire surface.

c. Following another drying and washing process (pH=3), the crystallization of PbS QDs onto the nanowires surface takes place in an aqueous solution of 0.5 M Sodium Sulfide ( $\text{Na}_2\text{S}$ , Sigma Aldrich, 99.9%), which brings the pH to 12.

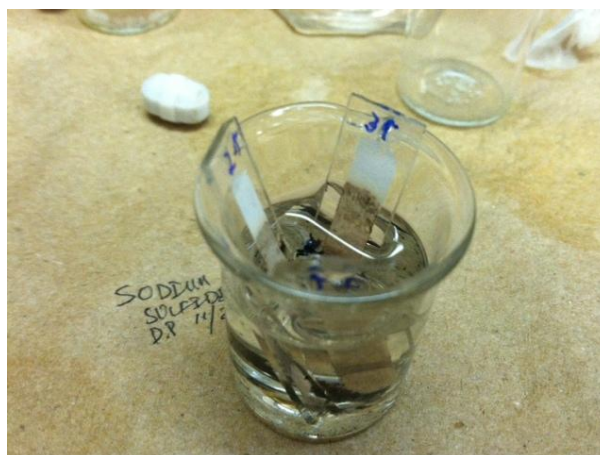


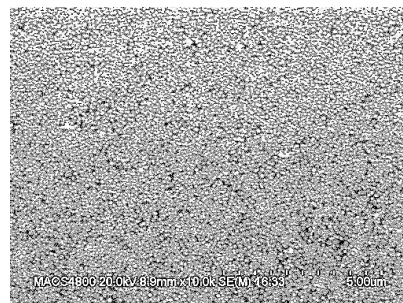
**Figure 3.6** –  $\text{TiO}_2$  nanowires treated with PbS quantum dots. The crystallization is complete when the Lead (II) Nitrate treated surface is immersed in Sodium Sulfide solution. This turns the slide color from white to dark brown.

### 3.4 Platinum Deposition on Counter Electrode via DC Sputtering

To prepare the counter-electrode, ITO glass slide was used as the substrate for metal deposition. Upon cleaning in acetone, isopropanol and DI water for 15 minutes respectively, the slides were dried at 60 °C to remove any residual organics. The slide was then exposed to UV Ozone treatment to remove further contaminants and DC sputtering was chosen to sputter a nominal 100 nm at a rate of 1 Å/s. The thickness of the Pt film was recorded by a quartz crystal thickness monitor. The slide was then annealed at 80 °C for 10 minutes to electrically connect the nanoparticles.



(a)



(b)

**Figure 3.7** – Denton Vacuum sputter used for platinum (a). SEM image of Pt (b) for a thickness of 150 nm and thermally treated for 10 minutes at 80° C.

### 3.5 Injection of Electrolyte

Iodide based electrolyte with low viscosity with 50 mM of iodide/tri-iodide (Solaranix) in acetonitrile was injected by capillary action, filling the space left between the two electrodes to ensure charge transportation through a redox couple.

### 3.6 Material Characterization

In order to fully understand the DSSC and the complex interaction of its components, it is essential to study the material properties and its influence of device parameters. Accordingly, a number of nondestructive analysis methods and techniques for DSSCs have been developed. Thus, this section is dedicated to the experimental methods and techniques used to characterize and evaluate DSSCs. The section consists of three sub-sections that focus on different characterization and analysis techniques. Also, each sub-section describes the theory associated with a technique and the relevant experimental setup.

### **3.6.1 Raman Spectroscopy (Renishaw inVia Raman Microscope)**

Raman spectroscopy studies the vibration modes of molecules, and gives us a fingerprint on the molecules at play. Three lasers (514nm, 633 nm, and 785nm) are used to confirm the existence of the proper crystalline structures.

### **3.6.2 Photoluminescence**

Photoluminescence spectroscopy has been widely recognized as a useful tool for characterizing the quality of semiconductor materials as well as for elucidating the physics may accompany radiative recombination. PL is useful in quantifying: (1) optical emission efficiencies, (2) composition of the material, (3) impurity content, (4) layer thickness (such as quantum well thickness).

Photoluminescence is most commonly characterized via spectroscopic techniques. These techniques involve measure the energy distribution of emitted photons after optical excitation. This energy distribution is analyzed to give us an idea on the size and band gap of the nanocrystals.

### **3.6.3 SEM (Hitachi S-4800 Scanning Electron Microscope)**

This imaging tool serves as a great way of viewing the crystallinity of our films, the surface thickness and topology, and to see how well the composite nanoparticle and nanowire composites formed.

### **3.6.4 TEM (Hitachi Transmission Electron Microscope)**

Transmission electron microscope images serve to give us an insight into the size and distribution of the quantum dots on the nanowire surface.

### **3.6.5 AFM (Multimode Atomic Force Microscopy)**

Atomic Force Microscope images were obtained with an Atomic Force Microscope (AFM) in tapping mode, and using silicon tipped cantilever from at 200-400 Hz. Scan size and speeds were adjusted as images were calibrated.



### 3.6.6 UV-Vis (Jasco V-670 UV-Vis Spectrophotometer)

Besides directly measuring photovoltaic properties of solar cells, optical techniques are also useful to characterize and optimize isolated cell components. A common example of this is a comparison between UV-Vis absorbance traces of sensitizers on the substrate, such as nanoparticle/nanowire film, the sensitizing dye, and quantum dots. Such characterization offers a way to qualitatively determine the aggregation of the dye on the nanostructured surface, which can produce supporting information of measurement of the current of the cell as well as sensitization of the mesoporous surface.



**Figure 3.8** – Jasco V-670 UV-Vis-NIR Spectrophotometer setup.

### 3.6.7 4-Point Probe (MMR Technologies)

Resistivity gives use an on how conductive a film is, and how easy it is for electrons to transport through our photoanode. A setup composed of a 4-point probe station, with electrical source-meter(s) and computer controller was assembled in order to perform electrical characterize such as thin film sheet resistance. Two different configurations were setup to serve two types of films: (1) conditions for low/medium impedances up to  $10\text{M}\Omega$ , (2) the second one is suitable for medium and high impedances up to  $110\text{G}\Omega$ . Sheet resistance is a measure of resistance of thin films that are nominally uniform in thickness. If the thickness of the film is relatively constant, the sheet resistance is given by the ratio between resistivity of the material and its thickness  $t$ , as shown in Equation 3.1

$$(3.1) \quad R_S = \frac{\rho}{t} \quad \frac{\Omega}{\blacksquare}$$

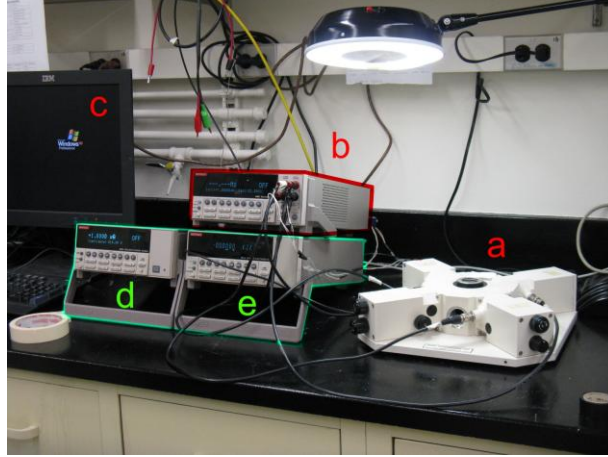


**Figure 3.9** – 4-Point probe setup.

From this equation one can know the overall resistivity if thickness and measurements of the sheet resistance. There are direct methods to measure this sheet resistance: the Kelvin Sensing and Van der Pauw method. We have chosen Van der Pauw method due to its ability measure resistance of arbitrary shaped thin film samples and simplicity.

After positioning the probes, the most basic version of this technique requires the measurement of two partial resistances  $R_A$  and  $R_B$  as it is illustrated in the following figure. The Van der Pauw resistance can be obtained from the numeral solution to the following equation:

$$(3.2) \quad e^{\left(-R_A \frac{\pi}{R_S}\right)} + e^{\left(-R_B \frac{\pi}{R_S}\right)} = 1$$

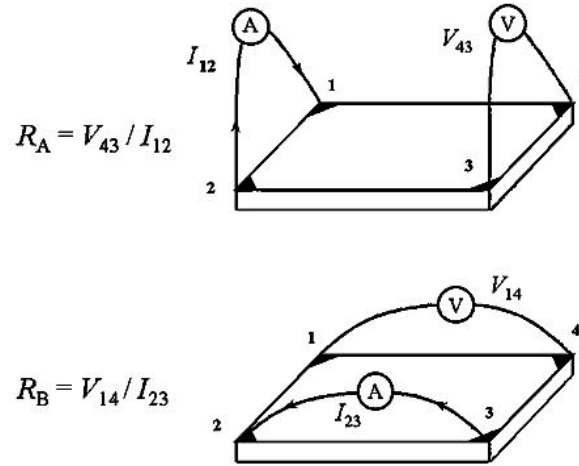


**Figure 3.10**– Schematic of the working principle for the Van der Pauw method for sheet resistance measurement of thin films.

The sample then has a 90° degree rotational symmetry and the contacts are equally spaced around the boundary. This reduces the formula to:

$$(3.3) \quad R_S = \frac{\pi}{\ln(2)} \frac{R_A + R_B}{2} f$$

The constant  $f$  in Equation 3.3 comes from the correction factor (see Appendix B) that is function of the ratio of the two resistances,  $r = R_A/R_B$ .

Four probes are equipped for both two sets of measurements,

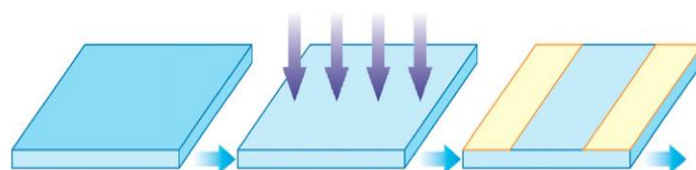
- Position the probes film with the configuration for  $R_A$  and measure current voltage output
- Position the probes film with the configuration for  $R_B$  and measure current voltage output
- Computer sheet resistance from equation above, and compute resistivity from the previous equation

In references to the Figure 3.9, the components of this configuration are:

- The 4-point probe station (a)
- The source-meter Keithley 2400 (b)
- Computer with National Instruments LabView software

### 3.7 Device Assembly

Once all materials are deposited, the device can now be assembled. The following figure shows procedural steps in the assembling of the device.

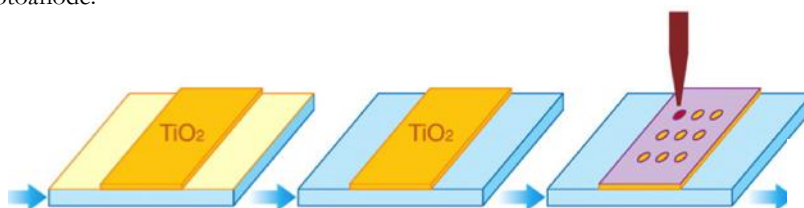


1. FTO (SnO<sub>2</sub>:F)

2. UV Radiation

3. Masking by Tapes

**Figure 3.11** – The FTO slide, after cleaning process, are exposed to UV Ozone treatment. They are then masked by Scotch tape for the deposition of the photoanode.



4. TiO<sub>2</sub> film on FTO

5. Removal of Tapes & annealing

6. Dye adsorption

**Figure 3.12** – The TiO<sub>2</sub> film upon annealing is loaded with the CuPc dye by drop casting the particles from the suspension.

Once the

tapes are in place, Dr. Blade technique is applied to each photoanode deposition. The tapes are then removed and the photoanode is treated thermally in an oven at 450° C. Tapes are then masked again for dye loading on the same exposed surface. Once dye loading is complete, the parafilm space is ready to be masked on.

### 3.7.1 Secondary FTO with Pt and Parafilm Spacer

To prevent the leakage of the liquid electrolyte and evaporation of the solvent, a spacer with the outline of the working area must place. Parafilm has chemical and photochemical stability with the electrolyte component, iodine, and the solvent, and therefore is best candidate as a sealant. The secondary slide with Pt sputtered on FTO is then sandwiched together with the space in between. To have the parafilm adhere to the surface of the slide, the pressed slides are placed in the oven at 60° C for 5 minutes. This creates a sufficient spacer to prevent leakage. After 5-10 minutes of cooling at room temperature, the devices are now ready for testing.

### 3.8 Solar Cell Characterization and Measurement

The photocurrent-voltage characteristics were performed using a Keithley model 2400 source measuring unit. A solar simulator with 150 Xenon lamp (Oriel) served as the light source, and its light intensity was adjusted using a calibrated (NREL certified) monocrystalline Silicon solar cell for AM 1.5 radiation. Once assembled, the DSSC can be characterized and modeled in a variety of ways. The figure below shows a typical I-V characteristics curve obtained when a voltage is applied between the two electrodes of a solar cell, allowing for the current to be measured under illumination. From this curve, the fundamental parameters of DSSCs performances such as short-circuit current, open-circuit voltage, fill factor, and the energy conversion efficiency  $\eta$ , can all be determined conveniently.

Short circuit current is the maximum output current of the cell, obtained when the external load resistance is zero (or negligible compared to the resistance of the device). Open-circuit voltage ( $V_{OC}$ ) represents the light-created maximum output voltage for infinite resistance load, which occurs at zero current. To produce power, the cell must operate in the fourth quadrant of the I-V plane at a voltage between 0 and  $V_{OC}$ . Since power is described as a product of current and voltage, both aspects of ideal current and voltage need to be dealt with. As voltage is increased from 0 to  $V_{OC}$ , power increases from 0, reaches a maximum at some point, and then decreases back to zero (See Appendix C). The maximum power ( $P_{MAX}$ ) is indicated by the shaded area of the rectangle from Figure 3.13. From the maximum power, the fill factor

(FF) can be calculated by Equation 3.4, which is defined as the ratio between the maximum output power of the cell and the product of short circuit current and open circuit voltage. The fill factor has a value between 0 and 1 and graphically is a measure of the ‘squareness’ of the I-V curve.

The overall conversion efficiency of the cell can be determined by the following parameters as described in Equation 3.5:

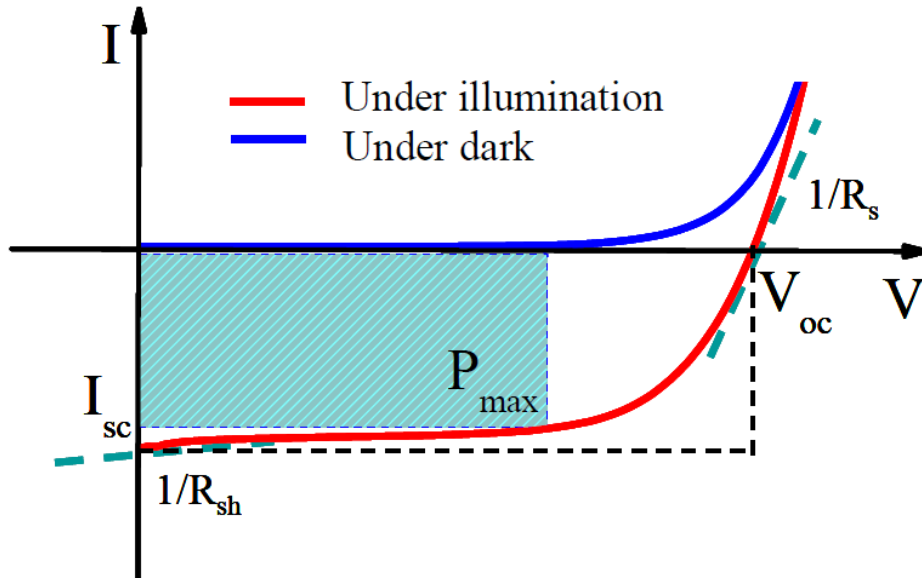


**Figure 3.13** – The characteristics of a photovoltaic cell.

$$(3.4) \quad ff = \frac{I_{MAX} \cdot V_{MAX}}{I_{SC} V_{OC}}$$

$$(3.5) \quad \eta = \frac{I_{SC} \cdot V_{SC} \cdot ff}{P_{IN}}$$

Generally, photocurrent-photovoltage (I-V) measurement is one of the standard characterization techniques that can obtain basic properties for any solar cell. The important figures of merit that describe the macroscopic performance of a solar cell that can be found from photocurrent-photovoltage (I-V) characterization include: short-circuit current, open-circuit voltage, fill factor, and overall conversion efficiency.

# 4

## Results and Discussion

In this section, we review the properties of the materials used, and their characteristics through various instruments. Through these tools, we will know the surface characteristics and topology of our films, the resistivity, the optical properties, as well as device performance under illumination.



## 4.1 Material Characterization

Prior to device testing, we first examine the host of materials used for our device, and verify their functionality with imaging and characterization tools. The porosity of the film, surface roughness, nanoparticle and nanowire composition, and the resistivity of our photoanode are of particular interest, since these parameters serve to affect device performance the most. PbS quantum dots are also review through their TEM images, photoluminescence (PL) spectra, decay of signal intensity, and the effects of multiple coatings on the distribution throughout slide.

### 4.1.1 TiO<sub>2</sub> Photoanode

There were two different methods to deposit our film, dip coating and the Dr. Blade technique. During dip coating, the solvent evaporates off as the slide is being withdrawn, and therefore parts of the slide are exposed to air, allowing the solvent to evaporate. Even though there is high viscosity in the solution, the gravitational forces on the slide cause uneven surfaces with visible marks. Therefore it was decided that Dr. Blade technique offers the most consistent method to deposit our photoanode film. Different compositions to our photoanode, which incorporated nanoparticles and nanowires, are also examined in detail to see if adhesion to the substrate and porosity for dye and quantum dot loading are also studied.

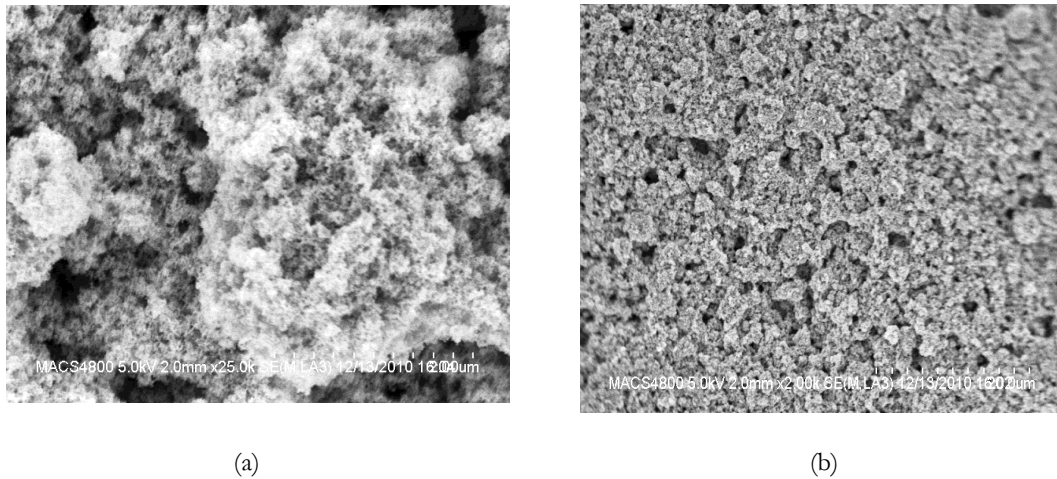
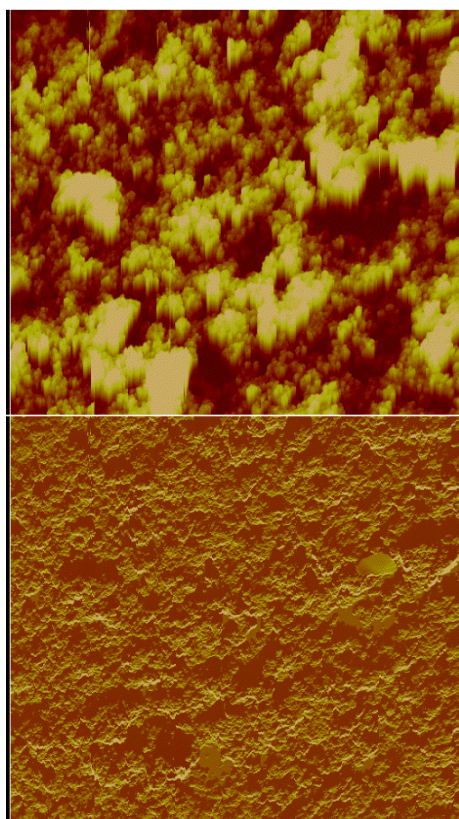
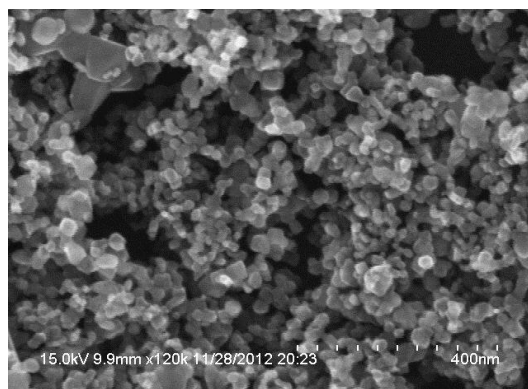


**Figure 4.1** - The high and low magnification SEM images show the surface composition of the film (a). The film has a mesoporous porosity, and high surface roughness, ideal for dye loading (b).

From these images, it can be verified that our film is continuous, the particle conglomerates are interconnected, and the porosity of the surface indicates a mesoporous film, condition best suited for dye adsorption. To examine the surface of the  $\text{TiO}_2$  nanoparticle network, we probe deeper to see the nature of the nanoparticle surface. The purchased  $\text{TiO}_2$  nanoparticle power indicated particles from 5-20 nm in size, and from the image below, this distribution is in line with what we expect.



(a)



(b)

**Figure 4.2** - The AFM image (a) shows the surface of the  $\text{TiO}_2$  nanoparticle film, which has a high roughness factor. The second half of the image shows our film as continuous. The FESEM image (b) shows the nanoparticles of  $\text{TiO}_2$ , ranging from 5-25 nm in approximate size. The particles are well interconnected, a necessary condition for DSSC photoanode.

### 4.1.2 TiO<sub>2</sub> Nanowires

Fabrication of TiO<sub>2</sub> film from one-dimensional nanowire and nanotube structures has proven to be an effective way to improve the overall efficiencies of the devices [68]. The one dimensional nanostructure allows diffusion free electron transport along the axial direction to improve electron collection, while the light scattering effect from the sub-wavelength feature can enhance the effective absorption thickness of the quantum dots later.

In this thesis, we report the fabrication of superior TiO<sub>2</sub> film structure for QD DSSCs formed by Dr. Blade coating and annealing of thin compact TiO<sub>2</sub> nanowire films. The interconnected nanowire network structure maintains the large surface-to-volume ratio from traditional porous TiO<sub>2</sub> films, while allowing efficient electron transport along the nanowires.

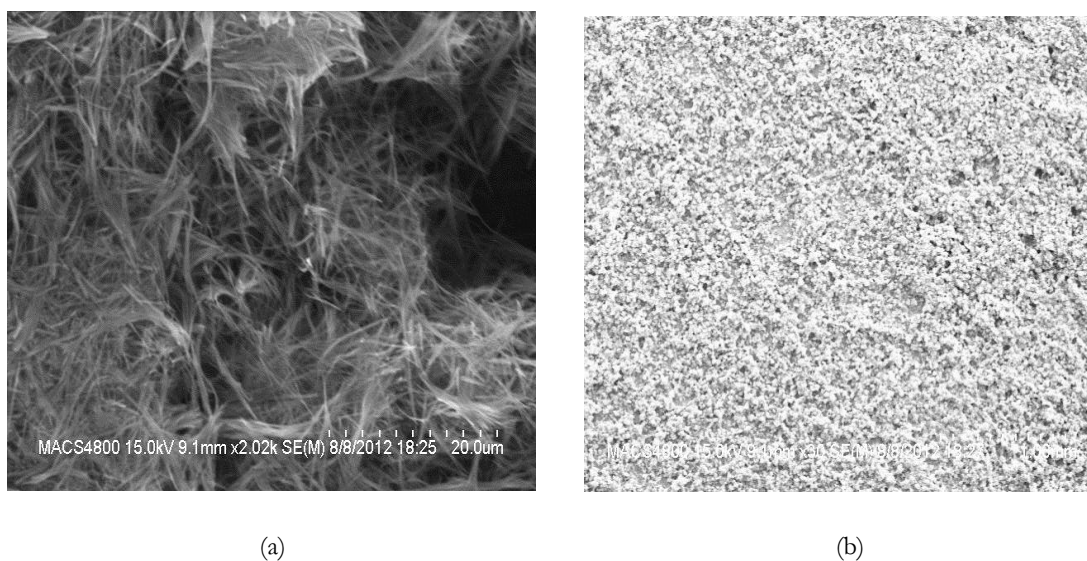


**Figure 4.3**– A low magnification on the surface of the film indicates continuity and interconnectedness (a). The surface topology has a rough surface, which makes it suitable for quantum dot and dye loading (b).

The  $\text{TiO}_2$  nanowires fuse with each at the contact point via sintering. On one hand, the one dimensional nanowire will reduce the aspect ratio and spheroidize owing to the surface energy reduction. Thus a high surface area, interconnected porous  $\text{TiO}_2$  nanostructure is fabricated using a facile process of Dr. Blade coating and annealing as shown the figure above. While the film does have pores, they do not distribute themselves equally in size, ranging from pores that are hundreds of nanometers to several microns wide.

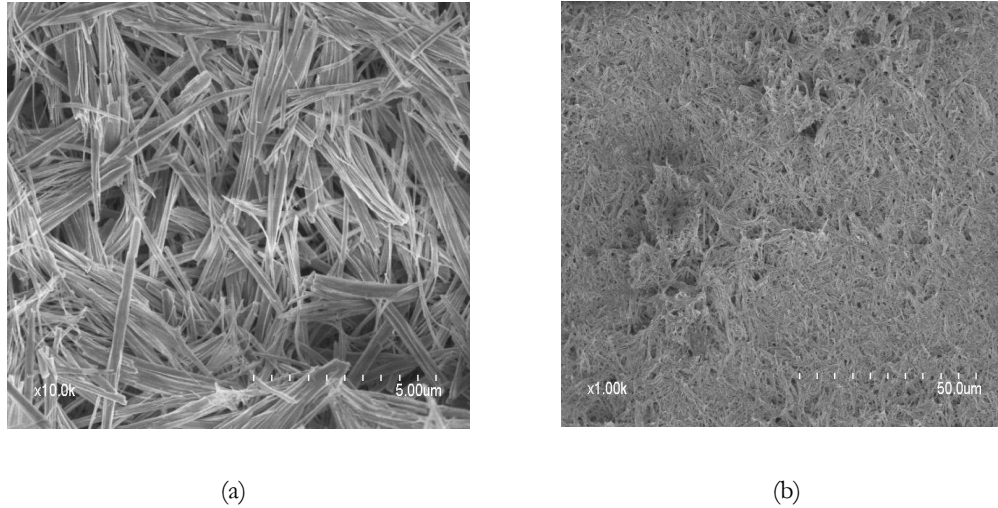


**Figure 4.4** – High-resolution SEM images show well dispersed nanowires (a) and surface topology (b).

The irregularly distribute nanopores are interconnected by spheroidized NWs after thermal annealing process, with average diameter of 150 nm and length of 3-5 μm.

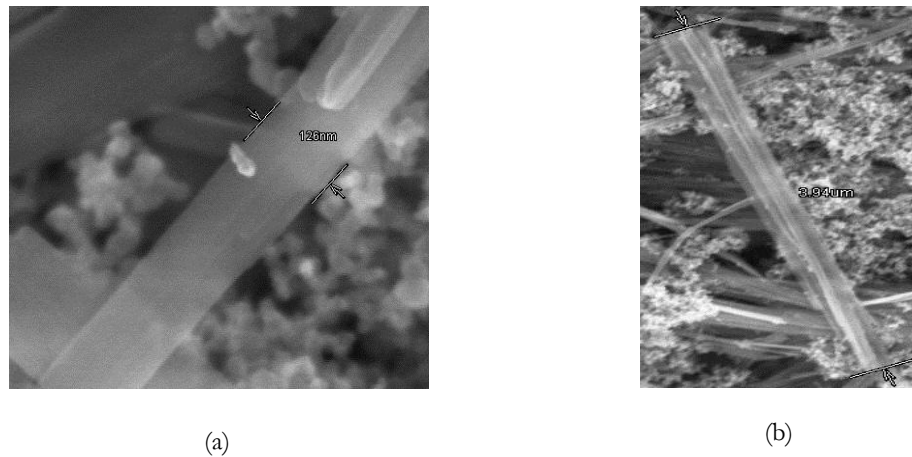
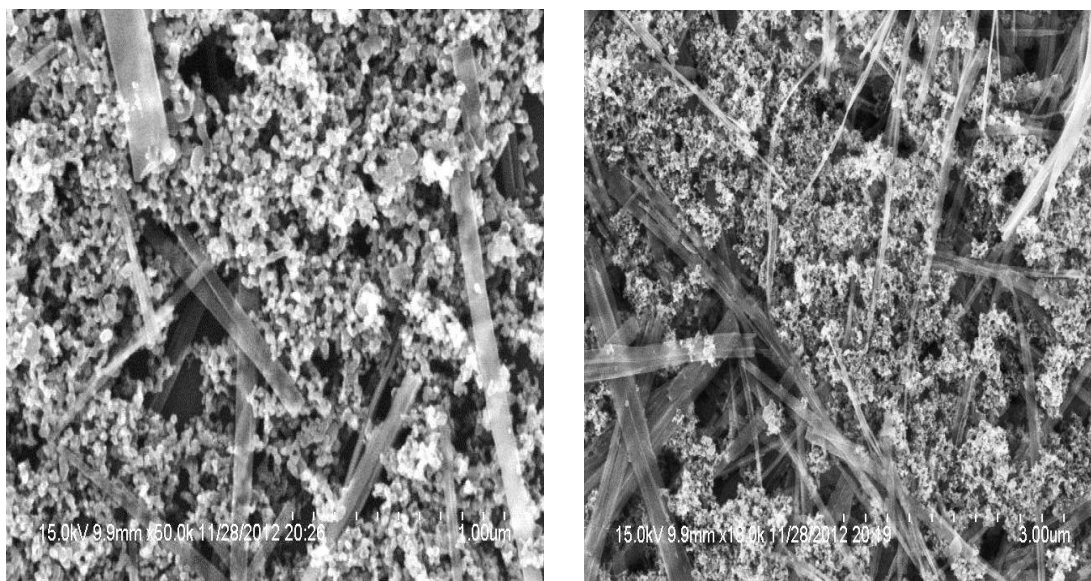


**Figure 4.5** – High-resolution images point to the average length and width of  $\text{TiO}_2$  nanowires.

As shown in the Figure 4.5,  $\text{TiO}_2$  nanowires are typically on the order of  $\sim 125$  nm in width and several microns in length. The high-resolution images confirm their sound crystalline structure.

We have also explored the idea of composite photoanode structure: one that contains a weight proportion of nanoparticle to nanowires. Three different mixtures were devised based on their weight percentage in solution: (1) 80 % wt. nanoparticle and 20 % wt. nanowire, (2) 50 % wt. nanoparticle and 50 % wt. nanowire, (3) 20 % wt. nanoparticle and 80 % wt. nanowire. These compositions were investigated to see which photoanode works to best harvest injected electrons and for their transport properties to the working electrode.



(a)

(b)

**Figure 4.6** - SEM high-resolution image of an 80% wt NP and 20% wt. of NWs (a) and 50 % wt. NP and 50% NW (b). These compositions are evenly distributed and there are neither aggregation sections of the nanoparticles of nanowires.

From Figure 4.6 and 4.7, it is clear that the weight ratios are confirmed by the composition of the surface.  $\text{TiO}_2$  anatase nanowires were well dispersed in the  $\text{TiO}_2$  nanoparticle matrix. No apparent cracks were observed by nanowire dispersion. The films exhibit excellent interconnectedness and porosity that is suitable for dye loading. The films do not show any agglomeration of nanoparticles or nanowires, but an even distribution throughout the film.

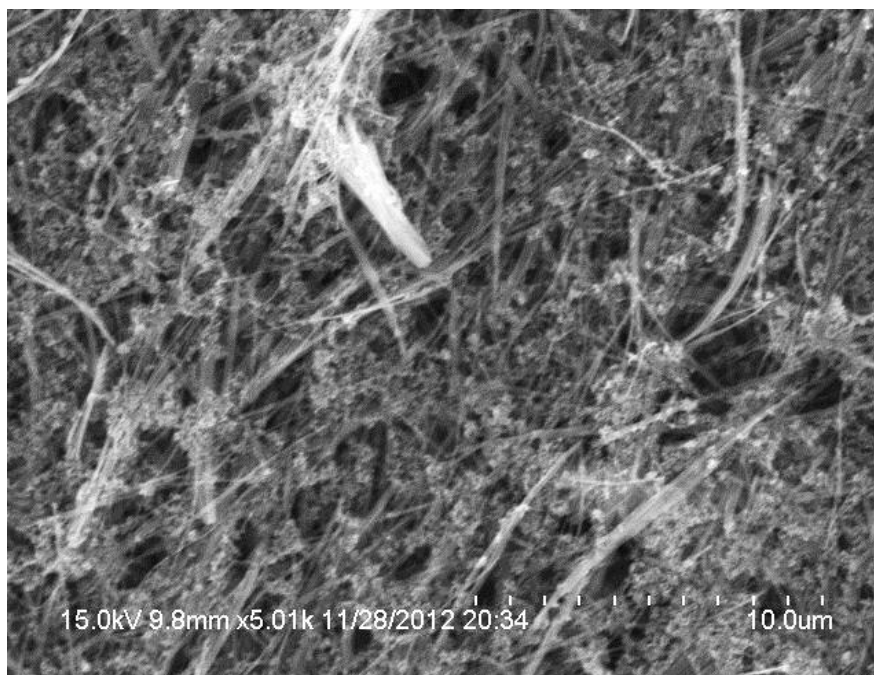


**Figure 4.7** - SEM high-resolution image of a 20% wt. NP and 80% wt. of NWs.

#### 4.1.3 Resistivity of Photoanode

In order to facilitate fast and efficient electron transport, the series resistance of the films must be low as possible. High resistance films have a significant influence on device parameters such as photocurrent. It serves to add to the series and shunt resistance to the cell. Increasing  $R_s$ , will decrease the short circuit current parameters of our cell.

Four point resistivity measurements were carried out on our different photoanode compositions. The table below has the resistivity and film thickness.

Resistivity of TiO <sub>2</sub> Morphologies		
Film Composition	Resistivity [ $\Omega$ -m]	Thickness [ $\mu$ m]
TiO <sub>2</sub> Nanoparticle	230	30
TiO <sub>2</sub> Nanowires	4.22	50
TiO <sub>2</sub> 80% NP 20% NW	7.31	33
TiO <sub>2</sub> 50% NP 50% NW	140	35
TiO <sub>2</sub> 20% NP 80% NW	46.4	42

**Table 4.1** – Resistivity values for the different TiO<sub>2</sub> morphologies as measured by Van der Pauw method. It was expected for nanowires to have the lowest value due its high crystallinity.

#### 4.1.4 CuPc Characterization

The only suitable method to deposit CuPc on our photoanode was by drop casting, as a stained bath solution did not adequately deposit a thorough film of CuPc on TiO<sub>2</sub>. The conventional method to deposit films of CuPc is by thermal evaporation, as solution-based processes present a difficult challenge since CuPc is not soluble in any organic solvent.

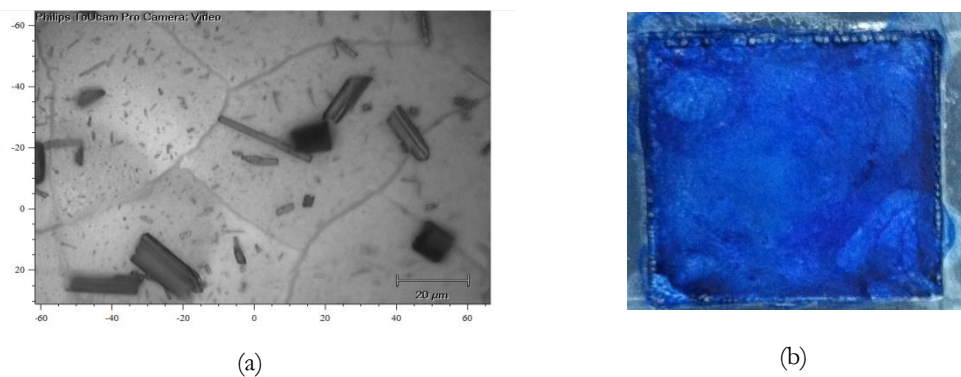


**Figure 4.8** – Optical microscope images show size distribution of the CuPc crystals. We can see that dispersion includes size from several hundred nanometers to tens of microns (a). The TiO<sub>2</sub> nanoparticle photoanode with CuPc loaded onto its surface (b).



From the image above, we see that the crystals are in contact with the  $\text{TiO}_2$  film, however, since the particle size distribution ranges from several hundred nanometers to several microns, it is not an effective way to sensitize the photoanode, therefore compromising the efficacy of the DSSC concept, which requires the particle size to be on the order of several nanometers such that these crystals can adsorb themselves on the mesoporous  $\text{TiO}_2$  crystal structure. Regardless, this method is an effective way to decorate the  $\text{TiO}_2$  surface in such a way that doesn't change the chemical or physical composition of the  $\text{TiO}_2$ .

We know that CuPc has strong absorption coefficient in the visible regions, particularly at the onset of its two pi-pi bond interactions. We use UV-Vis spectroscopy to verify the absorbance spectra of the crystal, and are expecting peaks around  $\sim 753$  nm and  $\sim 450$  nm.

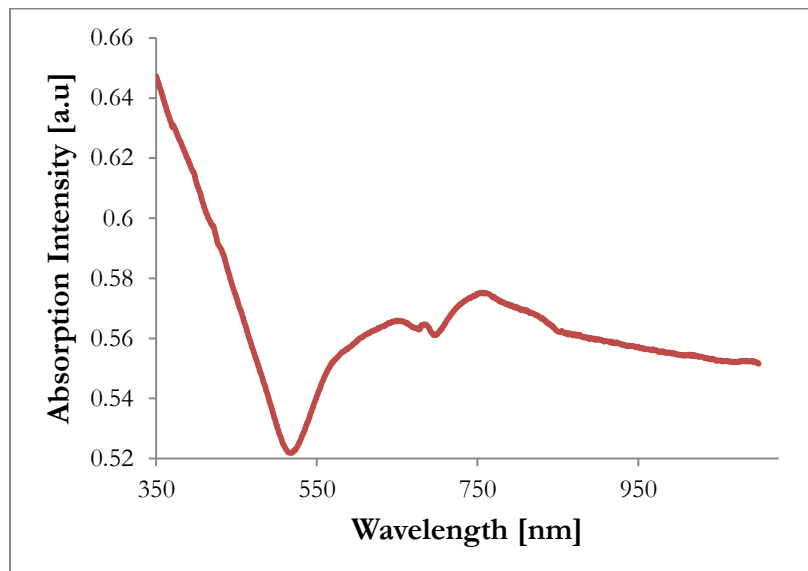


**Figure 4.9** – UV-Vis Spectroscopy of CuPc film. It is well known about its high absorption coefficient in the visible region, where we expect it generate most of the photocurrent.



#### 4.1.5 PbS Quantum Dots

Lead (II) Sulfide quantum dots are studied extensively in this thesis, for their structural and physical characteristics. The procedure outlined from our reference argued that different concentration of thiolactic acid determines the size of the crystallized quantum dot. Though they have evidence that this is true in their paper, which calls for *in situ* growth on  $\text{TiO}_2$  nanotubes, the same cannot be applied to nanowires. The authors claim this, however is not a conclusive study.

TEM images provide us with the best resolution into the crystallization of quantum dots on the nanowire surface. We expect our procedure to give us quantum dots that are 3-5 nm in size, however from subsequent images, we can see that is a distribution in the diameter of the QDs.

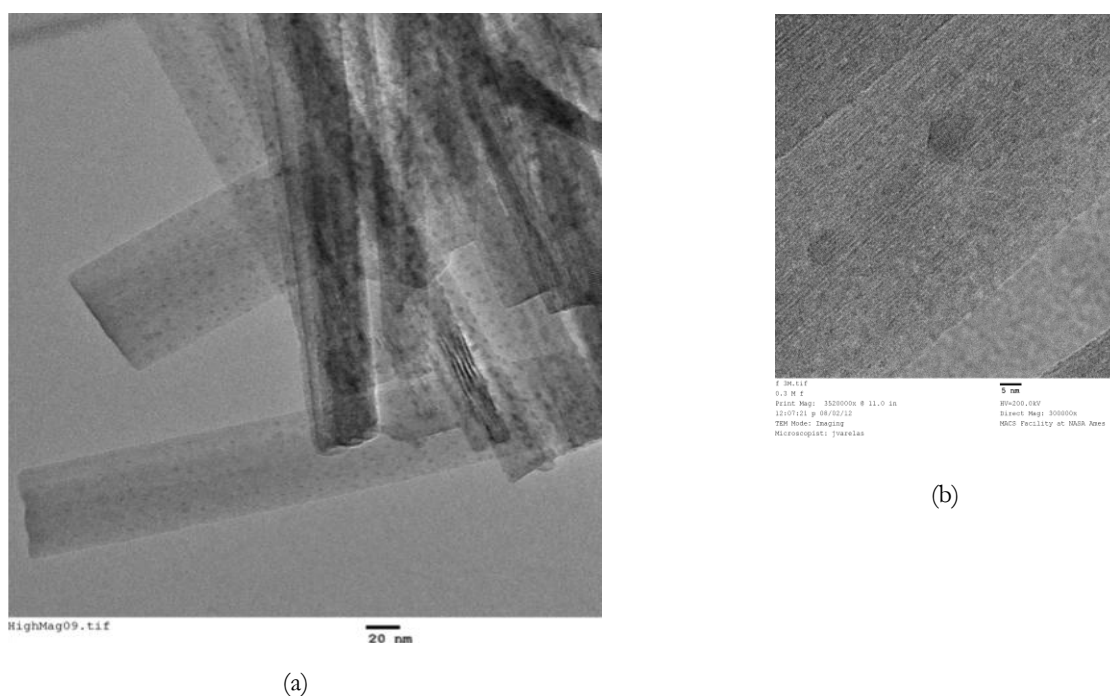


**Figure 4.10** - TEM images of  $\text{TiO}_2$  Nanowires coated with PbS quantum dots. The black dots indicate quantum dot crystals (a). The image (b) shows a single quantum dot that is approximately 5 nm in diameter from the scale.

The long chain of stabilizing thiolactic acid plays a crucial role in passivating the nanowires to prevent agglomeration. Therefore we see the quantum dots spread out along the surface. It seems that the quantum dots have adequately adsorbed onto the surface by the linker thiolactic acid.

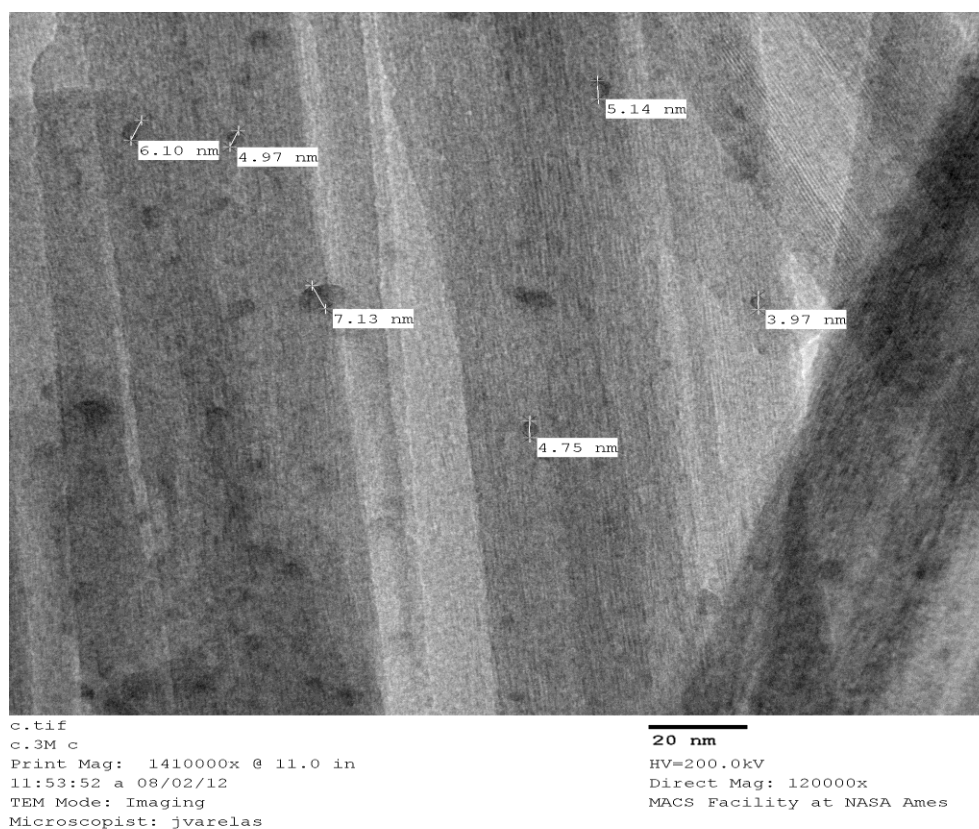


**Figure 4.11** – TEM image of  $\text{TiO}_2$  nanowires with PbS quantum dots. The size distribution of the quantum dots range from 4-7 nm in size.

From Figure 4.11, it is apparent that the diameter of the nanocrystals varies in size. Although the procedure outlines that a specific concentration leads to a crystallization of the nanocrystals at to a certain size, however, the distribution ranges from 4-8 nm.

#### 4.1.5.1 Photoluminescence of PbS QDs

To better understand the excitonic dissociation and electron extraction from the PbS quantum dots to the  $\text{TiO}_2$ , we studied the absorption and photoluminescence (PL) of the nanocrystalline films deposited on FTO. The electron transfer can be monitored through the shift and quench of the absorption and PL spectra. The conduction band of these small quantum dots lies well above that of  $\text{TiO}_2$ , thus the high energy excitons generation upon absorption of high energy photon in small QDs can rapidly dissociate with electrons injected to the  $\text{TiO}_2$  layer.

The rapid relaxation of high-energy excitons can in turn improve the absorption of high-energy photon by rapid depopulating of the excitons in the QDs. As can be seen from the absorption spectrum of the PbS nanocrystals deposited on  $\text{TiO}_2$  nanowire structure display a stronger absorption on the high-energy side and an obvious blue shift.

The photoluminescence of the quantum dots are quenched owing to hot electron transfer to  $\text{TiO}_2$ .

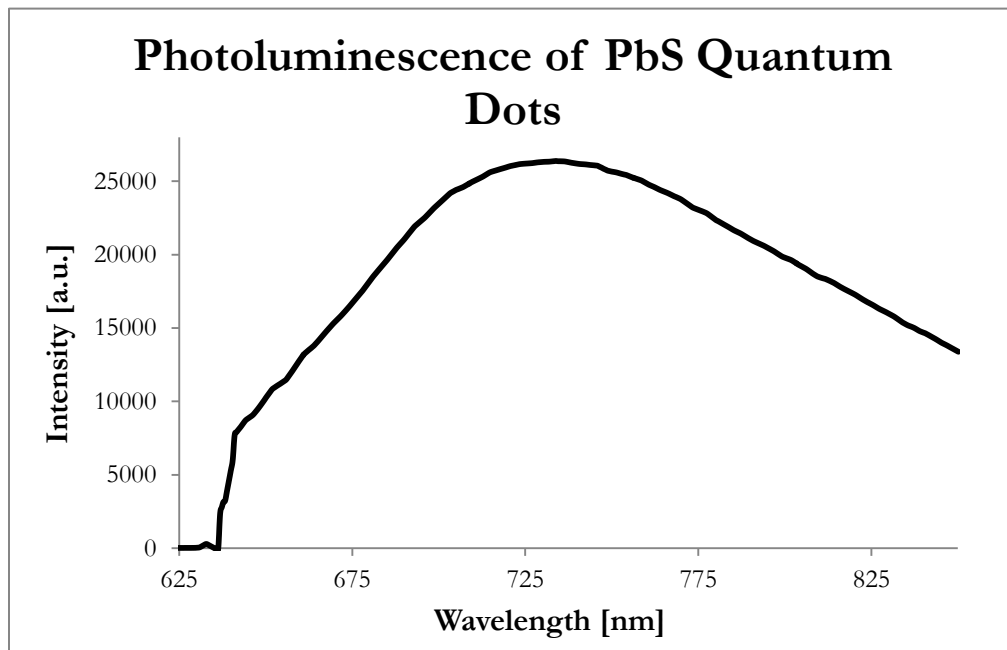


**Figure 4.12** - Photoluminescence spectra of PbS quantum dots excited with a 632.8 nm laser. The broadening of the peak tells us that ensemble of QDs excited must be from a range of sizes, emitting different wavelengths of light due to its varied diameter.

The above photoluminescence spectrum implies several key points about the quantum dot nature decorated on  $\text{TiO}_2$  NW surface. The width of the plot is a signature indication that the quantum dots are not one size, but a distribution in size. From our TEM image from before, we are able to discern the sizes of the quantum dots, ranging from 3.5 - 8 nm. The size dependence correlated directly into its confined band gaps. The broad peaks reveals that the ensemble of quantum dots under study are from a wide distribution of sizes, however concentrated mostly in the  $\sim 725$  nm region, which can be approximated at 4nm in size, contributing the most signal intensity from the ensemble of QDs. We also attribute the broadening to photoinduced oxidation of the QD surface, which causes an effective decrease in the QD diameter [69].

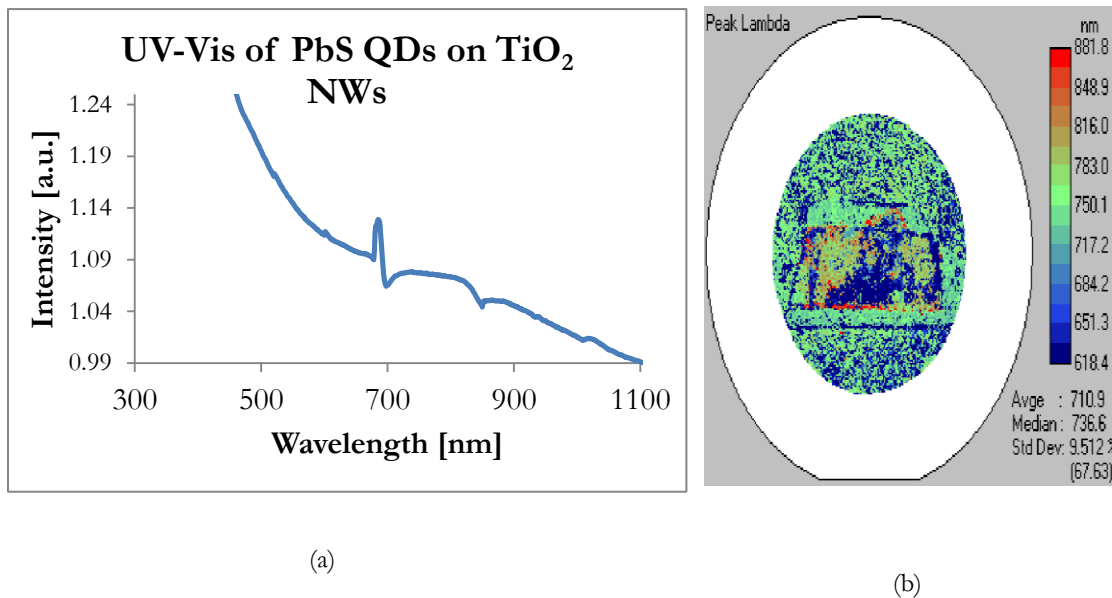


**Figure 4.13** – UV Vis spectra of PbS quantum dots excited with a NIR and UV-Vis lamp (a). The narrow peak at around  $\sim 700$  nm tells us a strong absorption. The broadening in the NIR region indicates the various diameters of the QDs. From the PL mapper image (b), only certain regions of the nanowire surface are decorated with PbS QDs. These regions of no signals are regions where the thiolactic acid did not properly link themselves onto the surface of the nanowire.

The UV-Vis spectra of PBs QDs are shown with a peak observed at around  $\sim 700$  nm. From this, it can be estimated that the bandgap of the QDs are from 1.4-1.8 eV. We however do observe a broad peak from 700-860 nm. This broad peak indicates that in the ensemble of quantum dots, there is a range in the diameter. The PL mapped image shows where on our slide the peak intensities are distributed. Since we

decorate the NW film with PbS, there are certain areas where the thiolactic acid linker molecule did not adequately adsorb onto the surface of the nanowires. This critical step is necessary for  $\text{Pb}^{+2}$  ions to latch to the linker for the crystallization process. Much of the  $\text{TiO}_2$  surface is still bare, that is, not covered with PbS QDs. Therefore experimental conditions for the deposition of PbS QDs must be adapted for higher density, either by applying the growth process in additional cycles, or introducing new synthesis methods such as successive ionic layer adsorption and reaction, known as SILAR [70].

#### 4.1.5.2 Crystallization Cycles of PbS Quantum Dots

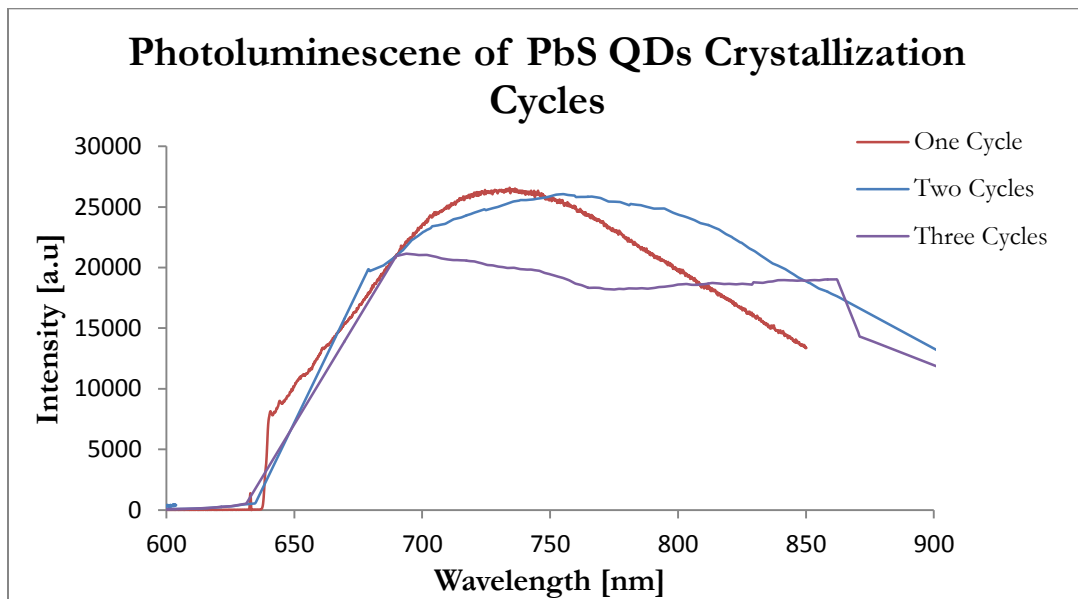


**Figure 4.14** - Photoluminescence spectra of PbS quantum dots excited with a 632.8 nm laser. The broadening of the peak tells us that ensemble of QDs excited must be from a range of sizes, due to cycles of crystallization, emitting different wavelengths of light due to its varied diameter.

The effect on the number of cycles in the optical properties of PbS is illustrated by the photoluminescence spectra in Figure 4.14. Increasing the number of cycles leads to a progressive aggregation of the QDs and a concomitant shift of the PL feature towards high wavelength. This red-shift from  $\sim 725$  nm to  $\sim 775$  nm indicates that there is a greater distribution in quantum dots themselves, and the size of the nanocrystals. It can be assumed that with this red shift, there are crystal greater than 8 nm and therefore extend into the

NIR region. This enhanced absorption in the NIR should increase the amount of photogenerated electrons, and consequently  $I_{SC}$ .

#### 4.1.5.3 Stability and Degradation of Quantum Dots

There is a continual decrease in measured photocurrent in PbS DSSC due to the progressive degradation of PbS, which is reasonably attributed to PbS oxidative process [71]. Therefore a study on the degradation process over some weeks was performed to measure the decay of the QDs. We use a PL spectra gathered on the same slide of quantum dots over the span of a month. From Figure 4.15, there is noticeable decrease in the intensity of the signal, as well as broadening of the PL peak. This clearly indicates that PbS QDs decay progressively over the three weeks, and by the fourth week, there isn't any discernible signal.

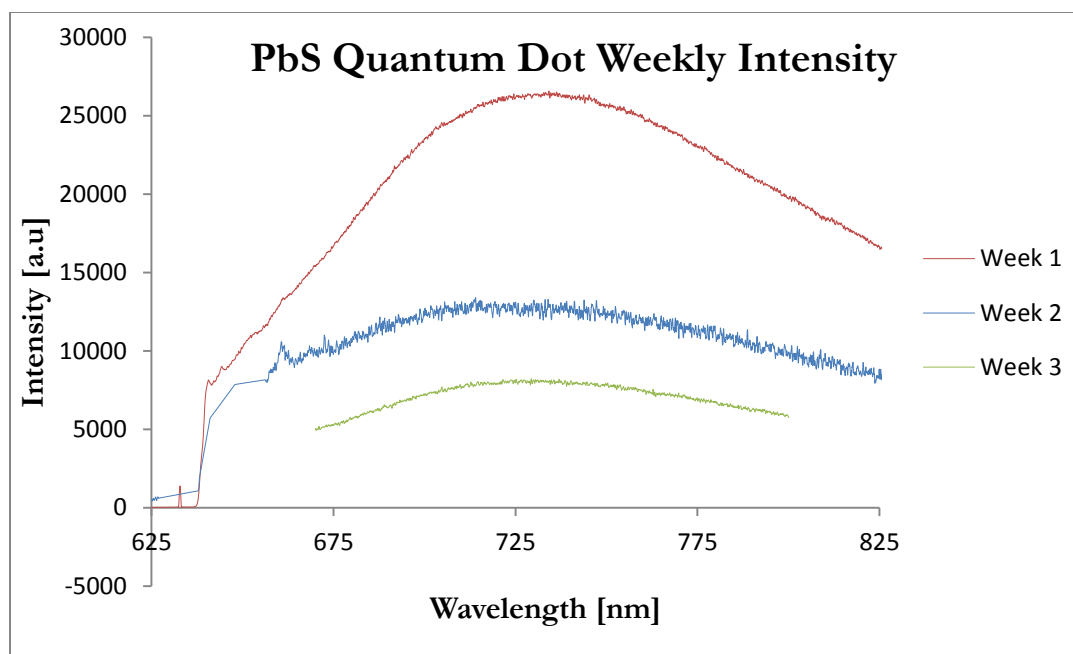


**Figure 4.15** - Quantum dot PL intensity measured over a period of three weeks. Due to the surface of QDs exposed, and as a result of oxidation, the crystals degrade with time, and therefore impose a limit on the stability of PbS QDs. Steps to passivate the exposed surface needs to be addressed.

This test highlights the vulnerability of quantum dots and its application in DSSCs. New and careful fabrication procedures has addressed in this by passivating the dangling bonds the surface, coating the quantum dot with a shell layer to protect them from degrading with time. These issues must be addressed if they are to have any potential for applicable use in the future.

#### 4.2 Co-Sensitization of TiO<sub>2</sub> Nanostructures by Raman and UV-Vis Spectroscopy

Raman spectroscopy was used to identify the crystal structure of TiO<sub>2</sub> anatase and composite as illustrated in Figure 4.16 and Figure 4.17. There are three crystalline structures of TiO<sub>2</sub> -brookite, anatase, and rutile. The spectrum in Fig 2 confirms the four significant modes of the anatase TiO<sub>2</sub> film that are assigned to the tetragonal structure of anatase TiO<sub>2</sub> as in previous reports [72]. Once we were able to verify the dominant anatase crystal structure of our film, we loaded the CuPc crystals into the solution with TiO<sub>2</sub>. We look at the crystal structure of our composites to see if CuPc adsorbed onto the TiO<sub>2</sub>. Using the 514 nm laser, the hybrid composite Raman spectra in Figure 4.17 show nearly identical patterns to TiO<sub>2</sub>. This result implies that the small percentage of CuPc loaded with TiO<sub>2</sub> did not change the basis crystalline of TiO<sub>2</sub> but indicates that it existed as a sensitizing agent. The dual-sensitized Raman spectrum also highlighted in Figure 4.17. It shows the vibrational modes of TiO<sub>2</sub> anatase, CuPc, and PbS QDs. This spectrum indicates that both CuPc and PbS sensitize the photoanode without any structural changes.

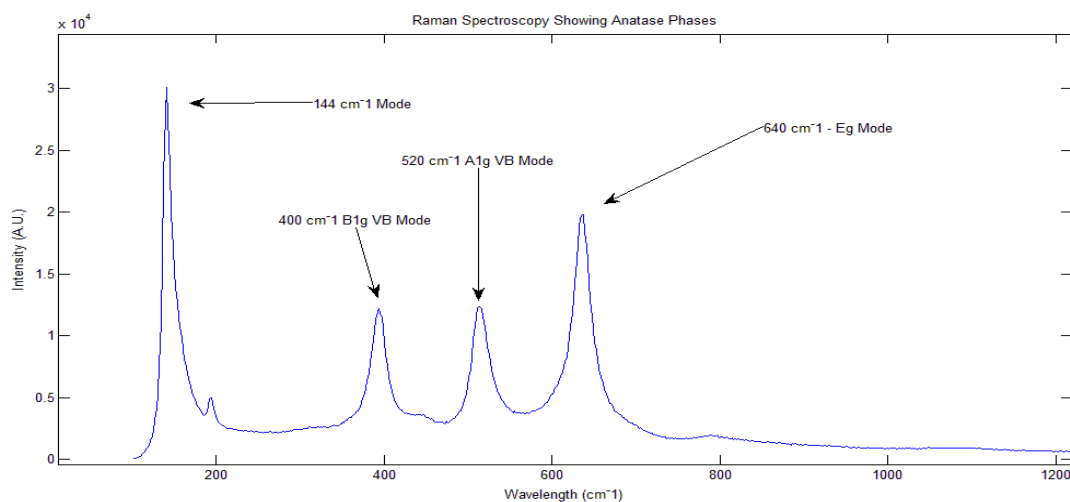


**Figure 4.16** – Raman spectroscopy showing the vibrational modes of TiO<sub>2</sub> anatase.

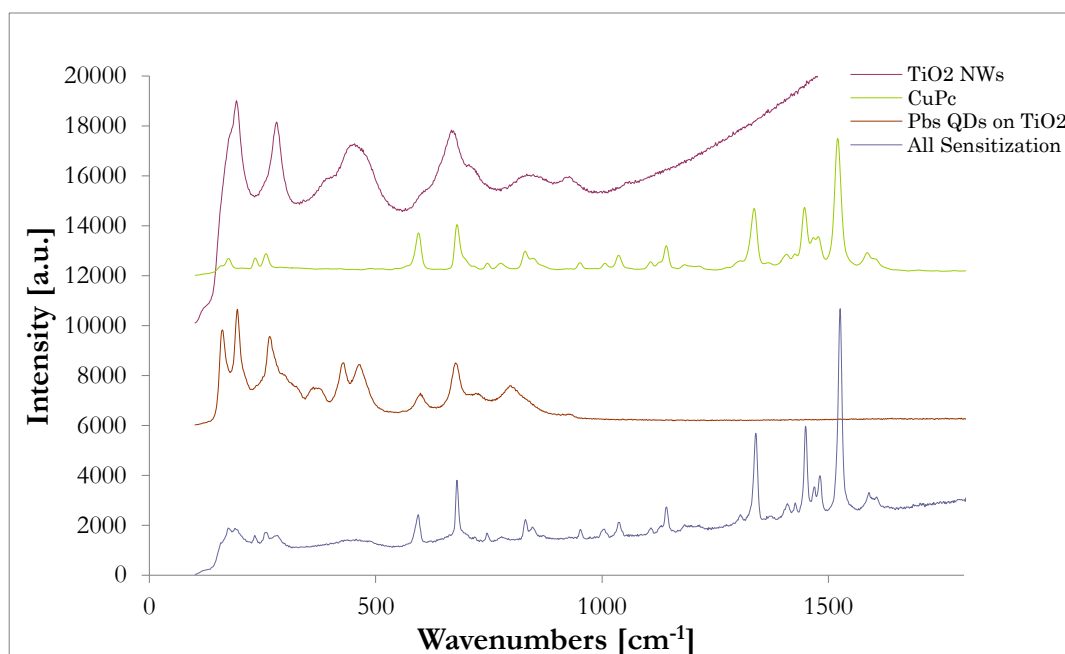


**Figure 4.17** - Raman Spectra of  $\text{TiO}_2$  NW, CuPc, PbS QDs on  $\text{TiO}_2$  NWs, and Sensitized  $\text{TiO}_2$  by both sensitizers CuPc and PbS QDs. This plot indicates that the overall  $\text{TiO}_2$  crystal structure has not deformed or changed by sensitization.

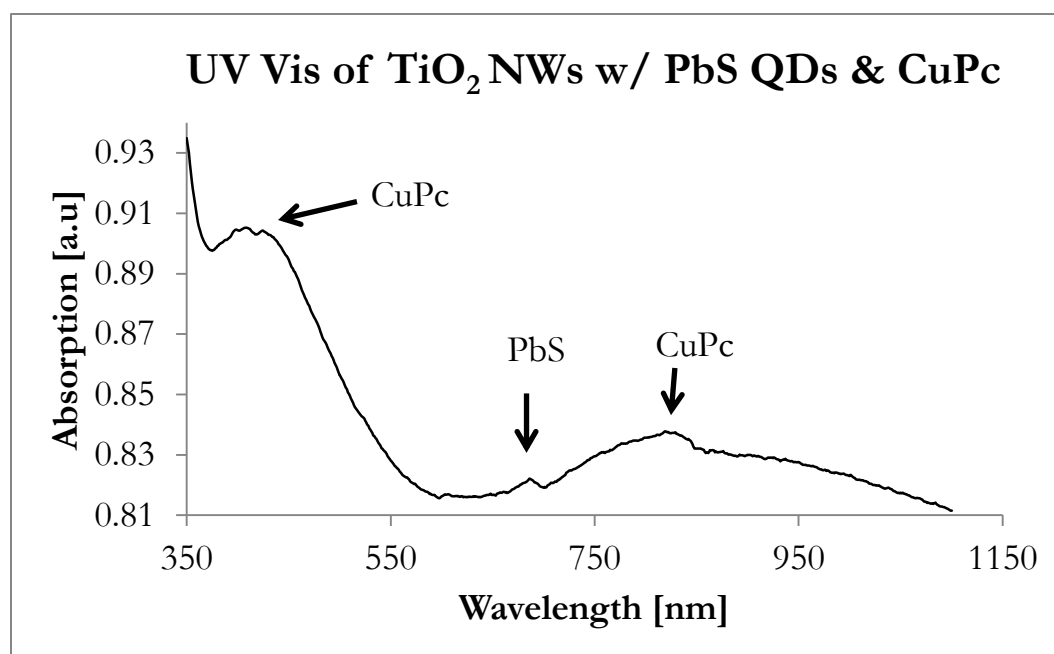


**Figure 4.18** – UV-Vis showing the absorption band of both PbS and CuPc sensitizing agents. This spectrum highlights the extended light absorption into the NIR that was initially desired.



In the absorbance spectra from Figure 4.18, we see the absorption bands of both PbS and CuPc, indicated by the highlight peaks. These correspond to the band gap of PbS and the difference between the CuPc HOMO-LUMO levels. This spectrum confirms one objective of the device: to cover a broadband absorption from UV to NIR by incorporating three materials that are optically sensitive to these wavelengths.

### 4.3 Photocurrent and I-V Characteristics

I-V characteristics of the several devices fabricated with different photoanodes and combination of sensitizers are discussed in this section. The solar simulator setup was assembled for this experiment and component features were discussed in detail in the prior section. The light source of this setup produces nearly 1 suns power with an AM 1.5 G filter on a small circular aperture of 10 cm in diameter. The active layer of the device was about 1 cm<sup>2</sup>. We plot the I-V curves of each device, and present the device parameters in Figure 4.19 and Table 4.2.

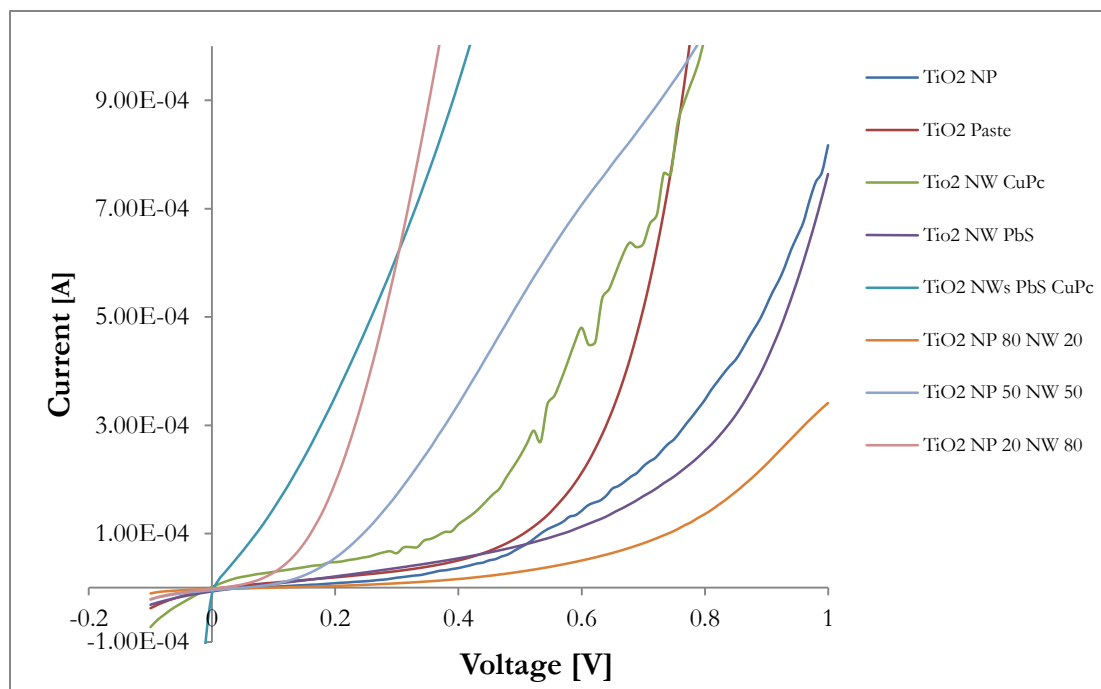


**Figure 4.19** – I-V Plots of the various photoanode compositions and sensitizing agents in the cells tested. All device show typical I-V characteristic curve.

**Table 4.2** – I-V curve plot parameters of the devices tested under 1 sun illumination with a AM 1.5G filter.

Device Properties	I <sub>sc</sub> (μA)	V <sub>oc</sub> (mV)	FF	η (%)
TiO <sub>2</sub> NP w/CuPc	3.18	335	.26	-
TiO <sub>2</sub> NP Paste CuPc	3.14	185	.41	.002263
TiO <sub>2</sub> NW CuPc	1.4	256	.33	.00001
TiO <sub>2</sub> NW PbS QDs	6.84	365	.35	.00015
TiO <sub>2</sub> NW PbS QDs CuPc	10.14	306	.45	.0030
TiO <sub>2</sub> 80% NP 20% NW CuPc	2.49	153	.36	.00057
TiO <sub>2</sub> 50% NP 50% NW CuPc	4.55	219	.43	.0038
TiO <sub>2</sub> 20% NP 80% NW CuPc	2.03	85.7	.43	.00001

TiO<sub>2</sub> NWs with PbS QDs from the table confirms the sensitization of TiO<sub>2</sub> nanowires. Here, the quantum confined dots of relatively small band gaps with their conduction band well above that of TiO<sub>2</sub> were used to achieve nominal electron injection and transport to the TiO<sub>2</sub> [3], as the schematic for the band diagram is presented in Figure 4.20. This increased photocurrent suggests that the nanowire structured film, along with the porosity of the film creates a suitable topology for quantum dot adsorption. For single sensitization devices, the quantum dot sensitized nanowire photoanode had a current of 6.84 μA, nearly five times as much with that of CuPc. This result can be attributed to four factors: (1) QDs are more suitable to adsorb on the surface of nanowires due to their small size, (2) the band structure of TiO<sub>2</sub> and PbS conduction band (CB) are aligned accordingly for electron injection, (3) the near unity quantum yield of quantum dots, and (4) the size of CuPc crystals are too large for the porosity of the TiO<sub>2</sub> to adequately sensitize the anode.

The TiO<sub>2</sub> NW/CuPc exhibited the smallest photocurrent than any of the devices. This can be equated to the physical attributes of CuPc; the size of CuPc ranging from several hundred nanometers to tens of microns, simply too large for proper sensitization. DSSC conceptually calls for sensitizing agents to be small such that they can percolate through the pores of the photoanode and be anchored on the surface of the TiO<sub>2</sub>. From our SEM images in Figure 4.3, it is observable that the reasonably physical attributes of the nanowire pore sizes are too small for CuPc crystals. Therefore, our CuPc particles are not in proper

contact with the nanowire surface, leading to small photocurrent. Anchoring of dyes are critical for generating photocurrent and the overall principle of DSSCs functionality, otherwise we simply lose the ejected electrons to recombination from the electrolyte.

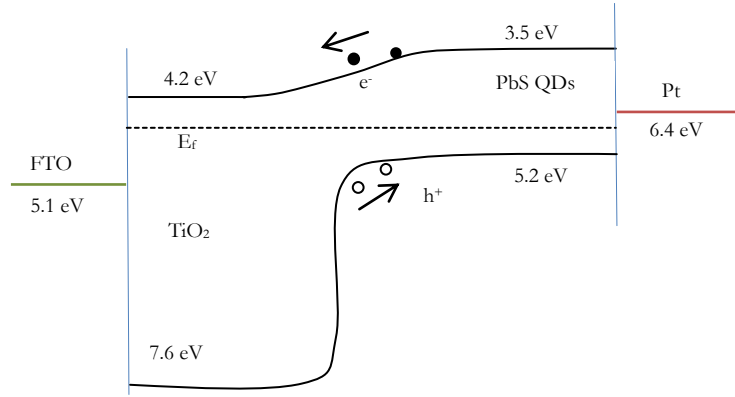


**Figure 4.20** – Band Energy schematic of PbS quantum dot sensitization. This band energetics favors electron injection.

An objective of this thesis was to see if incorporating two sensitizers can increase photocurrent. The TiO<sub>2</sub> NW/PbS/CuPc device exhibited the largest photocurrent of 10.14  $\mu$ A, a nearly 45% enhancement. This behavior can be adequately addressed by two operating principles: (1) the PbS QDs, adsorbed onto the surface of the nanowires directly injects electrons into the CB of TiO<sub>2</sub>, facilitating easier electron transport, (2) the CuPc crystals that are in direct contact with the nanowire surface also contribute to overall photocurrent. This result implies that co-sensitization is possible in 1-D nanostructure. If the CuPc crystals were in the tens of nanometers in size, and adequately adsorbed onto the surface of the nanowires, we can expect the photocurrent to increase dramatically, since it is known for electron injection, transport, and collection to be much higher in a nanowire photoanode versus a conventional nanoparticle matrix [14].

When we examine the photoanode composition that incorporates both nanoparticles and nanowires, there are some interesting results to discuss. When 20 % wt. of nanowires are incorporated, we see a modest increase in I<sub>SC</sub> (2.49  $\mu$ A) from the pure nanowire device (1.40  $\mu$ A), but a decrease from the pure

nanoparticle matrix (3.14 uA). This enhanced photovoltaic performance can be attributed to several reasons.

It could be credited to the porosity of nanoparticles versus nanowires. In the NP matrix, the surface area is larger, and the porosity is in the micron scale, as well as its distribution through the film. In the nanowire films, the pores are not large, and nor are they evenly dispersed. However, the increase in photocurrent from the pure nanowire device is likely a consequence of the faster electron transport in nanowires than that of nanoparticles.

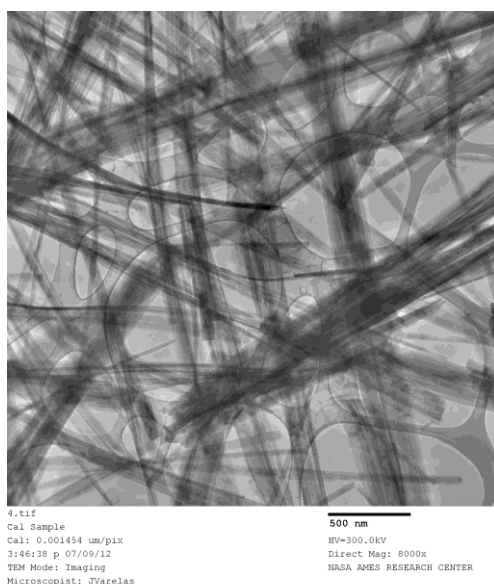


**Figure 4.21** – The porosity of the nanowire film does not adequately meet the need for the size of CuPc.

Nevertheless, one major concern with lateral nanowires is the small surface area it presents for dye and quantum dot sensitization. From our table above, the photocurrent-voltage curves of DSSC of 50% wt. nanowire addition demonstrates a substantial increase in photocurrent than the basic nanoparticle matrix or nanowire film. This enhanced photovoltaic performance can be attributed to several reasons.

First, TiO<sub>2</sub> anatase phase nanowire seems to have faster electron transfer ability, since transport exists only in the axial direction, thus reducing the possibility of electronic scattering due to the high crystallinity order. Park et al [74] reported that the speed of electron transfer in anatase layer is faster than in a rutile

later. P-25 TiO<sub>2</sub> powder (matrix nanoparticles) consisted of anatase and rutile phases in a ratio of 7:3. Anatase nanowire dispersion into DSSC electrode increases the anatase ratio in the film, resulting in the improvement of photovoltaic measurements. Second, it is thought that the packing density can be increased by mixing two nanomaterials with different size and morphology. The enhanced of light scattering induced the nanowires may be an important factor [72]. Nanowires presumably act as electron path and lead rapid electron transfer, however further quantitative electron diffusion measurement is required to determine the contribution from these factors. In the device in which the weight composition of nanowires and nanoparticles are even (50/50), the photocurrent is the best performing amongst the mixed anodes by a factor of 2. This can be attributed to two desired factors in which this film has over the others: (1) a distribution of the porous nature of the film from the nanoparticles, (2) faster electron transport from the nanowires. This even weight composition seems to be a good candidate for a photoanode that generally draws on two desirable qualities: mesoporous film structure and a fast electron transfer through the anode.

Considering the data obtained from the solar simulator, QD photocurrent values were the most promising and showed to have the single most contributing factor out of the two sensitizers. This seems trivial since the QDs are more efficient in their quantum yield, as well as the band structure allows for electron movement through the CB of TiO<sub>2</sub>.

#### **4.4 CuPc Dispersed in TiO<sub>2</sub> Matrix**

Since the CuPc crystals used in our devices are far too large for proper sensitization, we sought to create a photoanode with CuPc crystals interspersed in the TiO<sub>2</sub>. From the nature of our deposition technique, there is a gradient of the number of particles throughout the film, resulting in aggregation of dye molecules in certain regions. Aggregation occurs when the dye molecules are packed so tightly that their wavefunction overlap is large enough to change their electronic character, which often causes the dyes to quench in the excited state before electron transfer can occur [56]. Knowing that their size are incompatible with the nanometer structure of the TiO<sub>2</sub>, a mixed solution of TiO<sub>2</sub> nanostructures and CuPc crystals were directly mixed as outlined in Section 3.3. Under the same solar simulator conditions, we tested the devices, primarily looking for a change in its photocurrent.

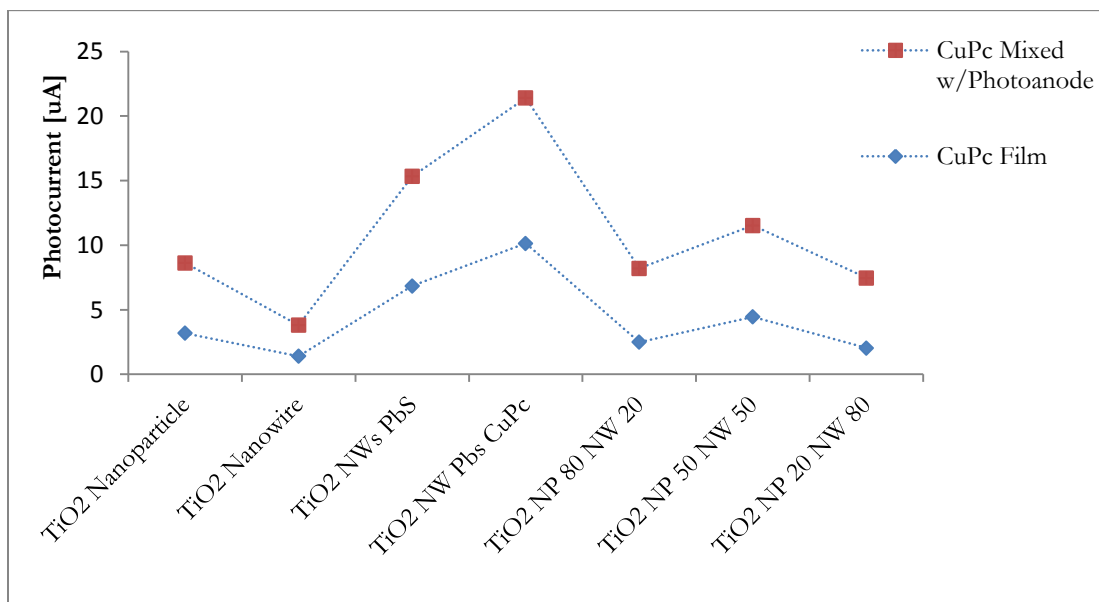


**Figure 4.22** – Chart comparing photocurrent of cells that had CuPc deposited as film on photoanode (blue), and CuPc dispersed within the TiO<sub>2</sub> morphology (red). Photocurrent increases when CuPc particles are dispersed with TiO<sub>2</sub>.

From Figure 4.22, for each device tested, there is a modest increase in the photocurrent. This is a probable result, since in this film deposition process, the CuPc crystals were interspersed with the TiO<sub>2</sub> nanostructure morphology. This process allows for CuPc crystals to imbed themselves within TiO<sub>2</sub> network, in contact with the nanoparticle/nanowire surrounding, rather than just a film on the surface. This ensures physical contact with TiO<sub>2</sub>, thus making electron transport from the CuPc to the TiO<sub>2</sub> more probable.

# 5

## Conclusion and Future Work

### **Conclusion and Future Work**

However, the record-high conversion efficiency of DSSC, which currently stands at 11.2 % has remained unchanged for nearly two decades [17]. Therefore, more basic and focused research effort is need to alter the structure and/or the nature of the components in the DSSCs, particularly in in the semiconducting layer that bridges the dyes and the electron collecting anode, in order to optimize the electron transfer energetics and kinetics.

Highly ordered one-dimensional nanostructures in ZnO nanowires and nanotubes, TiO<sub>2</sub> nanotubes and nanowires, and other compound offer a verifiable way to facilitate electron transport. These highly order 1-D semiconducting nanostructure provide an ordered pathway for electron percolating to the collecting anode, in contrast to the highly disordered electron pathway found in nanoparticulate layer than can lead to significant scattering of free electrons at the particle-particle interface [9,10] .

In addition, if the radius of the 1-D n-type semiconductors is large enough, an upward band bending that semiconductor surface can form, which suppressed the adverse back electron transfer from the semiconductor to the electrolyte or to the oxidized dyes. This is because the Fermi level of an n-type semiconductor is typically higher than the redox potential of the electrolyte. To equilibrate the two electron levels, electrons flow from the semiconductor into the electrolyte. As a result, there is a built-in circular electric field from the surface of the semiconductor nanowires towards their centers. This internal electrical field pulls the injected electron towards the center of wire, thereby reducing interception of the electrons by the electrolyte around the surface of the wire. The suppression of back electrons transfer, currently a major drawback of DSSCs, can improve the current density of cells.

However, so far, none of these ordered 1-D structure have achieved efficiency exceed that of conventional TiO<sub>2</sub> nanoparticle based DSSC. The reason lays in the fact that many other device parameters are often interlinked, which can offset or reduce the improvements brought by the new features. A particular problem addressed by Yang and co-workers is the diametric opposing effect resulting form increase the length of nanowires [9]. The compromise that nanowires exhibit are two competing factors: as the length of wire increases, they exhibit high short circuit current due to the increased surface area and thus higher dye loading. On the other hand, longer wired lead to higher series resistance, thus lowering the fill factor [11]. Narrow wires, thus denser, appear as a potential approach to overcome this problem. However, if the Debye-Huckel screening length exceeds the wire radius, reducing the diameter of the wires can eliminate the upward band bending at the wire surface [11], an advantage of the 1-D semiconductor discussed above. Therefore the depletion layer can extend to tens of nanometers in nanowires [12]. These dilemmas make is especially desirable to explore further investigation into 1-D ordered structures than can provide new fundamental insights to improve the efficacy of DSSCs.



Hence, the use of 1D nanostructures leads to the following paradox; the advantages of using a disordered material is sacrificed for the sake of improving the efficiency of the device. Tiorosh *et al* [12] found a substantial increase in the electron diffusion coefficient when a partial ordering is induced in the nanocrystalline electrode by means of an electrical field that is applied during the deposition procedure. This enhancement was interpreted in terms of percolation effects.

Another improvement to work upon is with the deposition of the photoanode on the conducting substrates. A small portion of the TCO surface is inevitably uncovered by the semiconducting particles, which allow the redox electrolyte solution to reach the exposed surface of the TCO, and thereby results in problems of electron leakage. Therefore, in this regard, an effort to passivate the TCO glass surface is imperative to improve charge collection. Therefore a compact thin blocking underlayer of  $\text{TiO}_2$  needs to be deposited by pyrolysis or a sputtering method to suppress the electron leakage at the interface.

Through research, it has been demonstrated that electron recombination time (lifetime) is correlated to the collection transport through the electron diffusion length [13] as shown in Equation 1.4. The diffusion Length  $L_n$  is the distance than an electron travels through the film before it is recombined to at the acceptor. Thus, in order to achieve efficient electron collect,  $L_n$  must be longer than the thickness of the semiconducting film. If  $L_n \gg t$ , then an efficient charge collection is achieved. For a typical DSSC, the efficient nanoparticle film thickness is limited to  $\sim 10 \text{ um}$ , resulting in one of the most important limitations of a DSSC [14]. A limited film thickness prevents an increase in the film's optical density in order to improve the device's light harvesting efficiency.

Semiconducting devices generally examine performance in terms of electron transport and collection. However, many devices neglect the potential for the second charge carrier, holes, in their potential to enhance device transport. In order to facilitate hole transport, band energetics must be favorable such that they move along the HOMO/VB levels accordingly to the counter electrode. Implementation of a photocathode that is a p-type semiconductor (p-SC), with a photoanode that uses the traditional n-type  $\text{TiO}_2$  can open a possibility to fabricate tandem DSSCs [54]. The theoretical limit that is imposed on photovoltaic devices goes from 31 % to 42 % in a tandem cell [54]. An extraordinary advantage of tandem DSSCs is the independence from a redox potential of the mediator and depends only on the difference between the potential of the valance band of the p-SC and conduction band of n-SC. Since the overall efficiency of the cell is proportional to  $V_{OC}$ , making a tandem cell is certainly a pertinent strategy to

enhance  $\eta$  of DSSCs. And lastly, a tandem cell contains two different sensitizers (one on each photoelectrode); therefore a larger portion of the solar spectrum could be harvested. This topic has received a great deal of interest for its potential to increase power delivered to the external circuit.

However, significant progress was made towards a better understanding in the phenomena behind DSSCs. We gained great insight into the energetics and kinetics behind DSSC, and can extend this knowledge to future work highlighted in the previous paragraphs. The device can reach enhanced photocurrent with a composite of both nanoparticles and nanowires. We can achieve enhanced photocurrent with co-sensitization of  $\text{TiO}_2$ ; incorporating both CuPc and PbS QDs. Thermal evaporation is the main technique to deposit CuPc, a technique that will allow nanometer size particles to adsorb onto the surface of  $\text{TiO}_2$ . Furthermore, increased cycles in crystallization and altering the sizes could greatly enhanced light harvesting into the NIR. With additional work, the goal is to create a highly efficient DSSC that has facile fabrication methods, easy scale up to larger modules, and enhanced photocurrent and efficiency.

# Appendix

# Appendix A

## Keithley 6514 and 6220 controller in LabVIEW

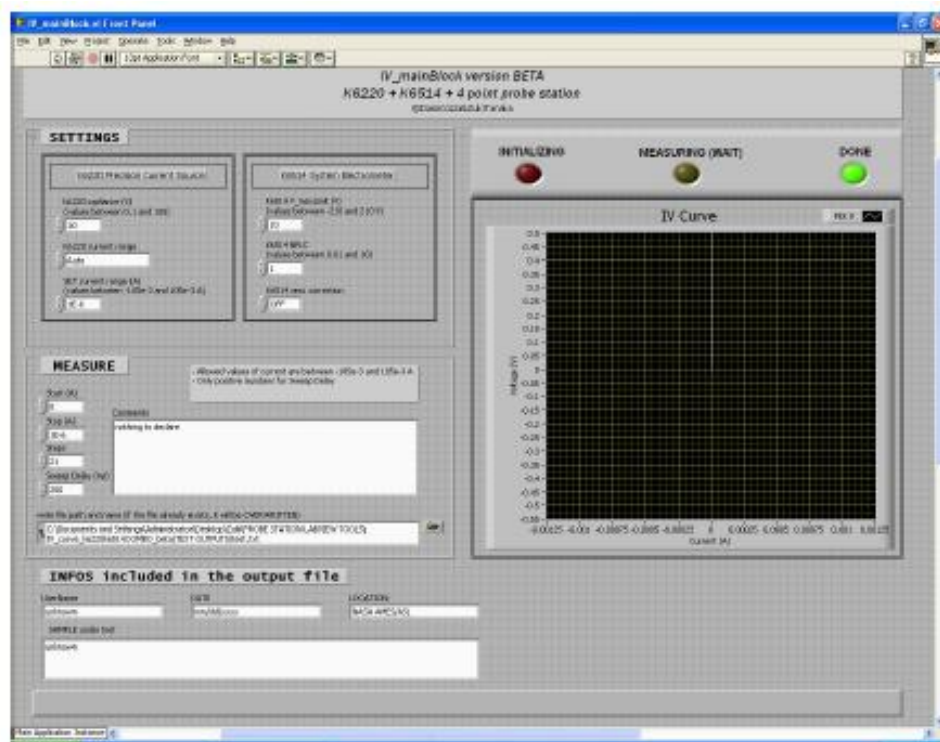
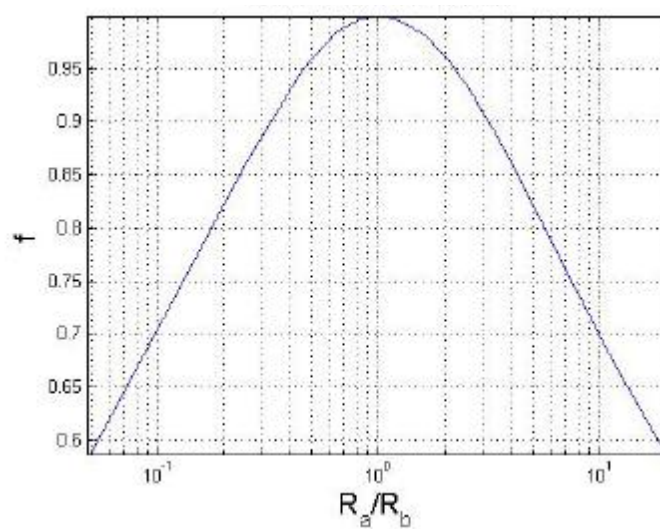


Figure A.1 – Interface LabVIEW Software for IV Plots and for resistivity measurements.

## Appendix B

Van der Pauw Sheet Resistance Correction Factor:



**Figure A.2** – Correction factor plot for the Van der Pauw method for thin-film sheet resistance.

# Appendix C

## Solar Cell Basics

DSSCs can be modeled in a variety of ways. Figure A.3 shows a typical I-V characteristic curve obtained when a voltage is applied between the two electrodes of a solar cell, allowing for the current to be measured under illumination. From this curve, the fundamental parameters of DSSCs performances, such as short-circuit current ( $I_{sc}$ ), open-circuit voltage ( $V_{oc}$ ), fill factor (FF), and the energy conversion efficiency ( $\eta$ ), can be determined conveniently.

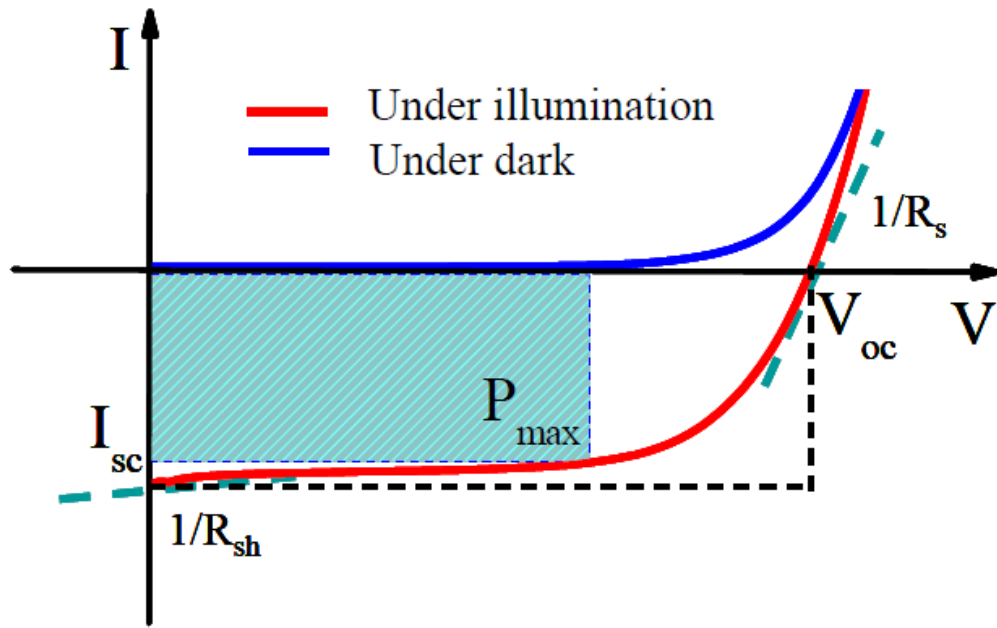


**Figure A.3** – Typical I-V characteristic for a DSSC under illumination (red curve) and dark measurement (blue).  $I_{sc}$ ,  $V_{oc}$ ,  $P_{max}$ ,  $R_s$ , and  $R_{sh}$  are the important parameters that can be obtained from an I-V characteristic.

Short circuit current is the maximum output current of the cell, obtained when the external load resistance is zero (or negligible compared to the resistance of the device).<sup>91</sup> Open-circuit voltage represents the light-created maximum output voltage for infinite resistance load, which occurs at zero current.

To produce power, the cell must operate in the fourth quadrant of the I-V plane at a voltage between 0 and  $V_{oc}$ . Since power is described as a product of current and voltage, both aspects of ideal current and

voltage needs to be dealt with. As voltage is increased from 0 to  $V_{OC}$ , power increases from 0, reaches a maximum at some point, and then decreases back to 0 as indicated in Figure A.4. The maximum power ( $P_{MAX}$ ) is indicated by the area of the rectangle in Figure A.4. From the maximum power point, the fill factor ( $ff$ ) can be calculated by the equation A.1, defined as the ratio between the maximum output power of cell and the product of short circuit current and open-circuit voltage. The fill factor has a value between 0-1 and graphically is a measure of the “squareness” of the I-V curve, where  $I_{MAX}$  and  $V_{MAX}$  can be obtained from the maximum power point of the I-V curve.

$$(A.1) \quad ff = \frac{I_{MAX} \cdot V_{MAX}}{I_{SC} \cdot V_{OC}}$$

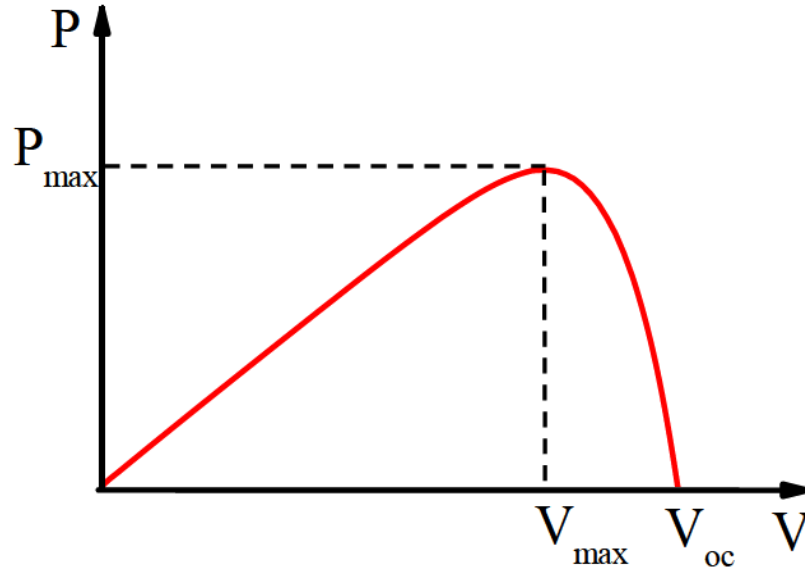


**Figure A.4** – Plot of Voltage vs. Power as obtained from the I-V curve. Power of a solar cell is given by the product of current and voltage. As the voltage is increased from 0 to  $V_{OC}$ , the cell power increases and reaches a maximum at  $V_{MAX}$  and  $I_{MAX}$ . At this point, the cell operates in a condition known as the Maximum Power Point (MPP).

Then, the overall conversion efficiency of the dye-sensitized solar cell can be determined by the short-circuit photocurrent, the open-circuit photovoltage ( $V_{OC}$ ), the fill factor of the cell ( $ff$ ) and the power of the incident light ( $P_{IN}$ ), as described in the equation A.2.

$$(A.2) \quad \eta = \frac{I_{sc} \cdot V_{oc} \cdot ff}{P_{IN}}$$

Electrically, the solar cell is equivalent to a current generator in parallel with a diode. Figure A.5 is a traditional equivalent circuit for an ideal DSSC. This model has been investigated extensively for the DSSC because it can provide internal electrical mechanisms working in the solar cell [52]. For example, the inherent electric characteristic of DSSCs, such as series and parallel resistance, may be estimated by fitting the equivalent circuit into I–V curve. In a cell, power is dissipated through the resistance contacts and leakage current in the device. In particular, power is lost due to series resistance ( $R_s$ ) and a parallel or shunt resistance ( $R_{sh}$ ) in the equivalent circuit. The series resistance arises from contact resistance, resistance of TCO substrate, semiconductor film, electrolyte resistance, and resistance of wires connected to the cell. The  $R_s$  value can be estimated from the reciprocal of the slope of the I–V curve at  $V=V_{OC}$  (Figure A.3). The shunt resistance is mainly attributed to the current leakage around the edge of the device, and particularly across the semiconductor/electrolyte interface. It can be approximated from the inverse of the slope of the I–V curve at  $I=I_{SC}$  (Figure A.3). After the parameters are determined by fitting, the current flow through the external load can be given by equation A.3.

$$(A.3) \quad I = I_{ph} - I_D = I_{ph} - I_o \cdot \left[ e^{\left( \frac{V+I \cdot R_s}{nV} \right)} - 1 \right] - \frac{V+R_s}{R_{sh}}$$

The terms of equation A.3 are follows:  $I_{ph}$  is the photocurrent density,  $I_o$  is the diode reverse saturation current (dark current),  $n$  is the ideality factor,  $V$  is the output voltage,  $R_s$  is the series resistance, and  $R_{sh}$  is the shunt resistance.

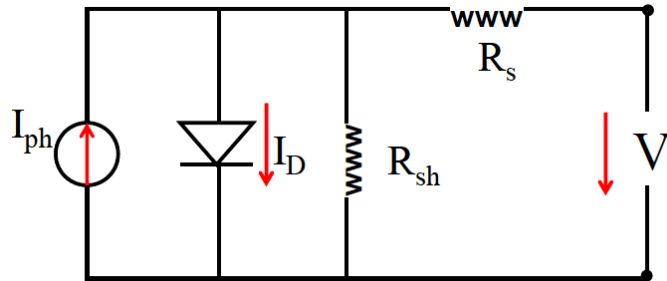


**Figure A.5** – The basic equivalent circuit model of a solar cell.  $I_{ph}$  is the photo-generated current source;  $I_d$  is the current passing through the diode.  $R_s$ ,  $R_{sh}$  represent series and shunt resistances respectively.



## References

1. Service, R.F. Solar energy - Is it time to shoot for the Sun? *Science*, 309: 548-551, 2005.
2. Graetzel, M. Solar Energy Conversion by Dye-Sensitized Photovoltaic cells. *Inorganic Chemistry*, 44(20): 6841-6821, 2005.
3. Atwater, H.A and R. Polman. Plasmonics for improved photovoltaic devices. *Nature Materials* 9, 205-213, 2010.
4. A. Hagfeldt, G. Boschloo, L. Sun, L. Kloo, H. Pettersson. *Chemical Review* 110, 6595, 2011.
5. Green, M.A., Emery, K., Hishikawa, Y., Warta, W., Dunlop, E.D. Solar Cell efficiency tables (version 38). *Progress in Photovoltaics: Research and Applications* 10, 565-572, 2011.
6. O. Semonin, J.M. Luther, and M.C. Beard. Multiple Exciton Generation in a Quantum Dot Solar Cell. *SPIE Newsroom*, March 26, 2012.
7. W. Shockley, H.J. Queisser. Detailed Balance Limit of Efficiency of p-n Junction Solar Cells. *Journal of Applied Physics* 4, 6032-6038, 1961.
8. O'Regan, B. and M. Grätzel. A Low-Cost, High-Efficiency Solar Cell Based on Dye Sensitized Colloidal TiO<sub>2</sub> Films. *Nature* 353, 737-740, 1991.
9. Peter, L.M. The Grätzel Cell: Where's next? *Journal of Physical Chemistry Letters* 2, 1861-1867, 2011.
10. A. Andersen, P.R.F. Barnes, J.R. Durrant, B.C. O'Regan. Quantifying Regeneration in Dye-Sensitized Solar Cells. *Journal of Physical Chemistry C* 115: 2439-2447, 2011.
11. Grätzel, M. Photoelectrochemical cells. *Nature*, 414, 338-344, 2001.
12. J.P Gonzalez-Vazquez, V. Morales-Florez, and J.A. Anta. How Important is Working with an Ordered Electrode to Improve the Charge Collection Efficiency in Nanostructured Solar Cells? *Journal of Physical Chemistry Letters*, 3, 386-393, 2012.
13. T.W. Hamman, R.A. Jensen, A.B. Martinson, H. van Ryswyk, J.T. Hupp. *Energy Environmental Science* 1, 66, 2008.
14. H. Xu, X. Tao, D.T. Wang, Y.Z. Zheng, and J.F. Chen. Enhanced efficiency in dye-sensitized solar cells based on TiO<sub>2</sub> nanocrystal/nanotube double-layered films. *Electrochimica Acta* 55, 2280-2285, 2010.
15. S.A. Haque, E. Palomares, B.M. Cho, A.N.M Green, N. Hirata, D.R. Klug, J.R. Durrant. *Journal of American Chemistry Society* 127: 3456, 2005.
16. I. Zumeta, J.A. Ayllon, B. Gonzalez, X. Domenech, E. Vigil. TiO<sub>2</sub> films obtained by microwave-activated chemical-bath deposition used to improve TiO<sub>2</sub>-conducting glass contact *Solar Energy Materials and Solar Cells* 93(10): 1728-1723, 2009.
17. M. Grätzel, Solar Energy Conversion by Dye-Sensitized Photovoltaic Cells. *Inorganic Chemistry* 44: 6841-6851, 2005.
18. G. Boschloo. A. Hagfeldt. Characteristics of the Iodide/Triiodide Redox Mediator in Dye-Sensitized Solar Cells *Accounts of Chemical Research*, 42, 1819-1822. 2009.
19. M. Grätzel, *MRS Bulletin* 30, 23 (2005).

20. L. M. Peter. The Grätzel Cell: Where's next? *Journal of Physical Chemistry Letters* 2: 1861-1867, 2011.
21. H.G. Agrell, G. Boschloo, A. Hagfeldt. Determination of the light-induced degradation rate of the solar cell sensitizer N719 on TiO<sub>2</sub> nanocrystalline particles *Journal of Physical Chemistry B*, 109 (47): 5100-5105, 2005.
22. S. Meng, E. Kaxiras. Electron and Hole Dynamics in Dye-Sensitized Solar Cells: Influencing Factors and Systematic Trends *Nano Letters*, 10: 1238-1247, 2010.
23. S. Kambe, S. Nakade, Y. Wada, T. Kitamura, et al. *Journal of Material Chemistry* 12: 723-728, 2002.
24. H.G. Agrell, G. Boschloo, A. Hagfeldt. Determination of the light-induced degradation rate of the solar cell sensitizer N719 on TiO<sub>2</sub> nanocrystalline particles *Journal of Physical Chemistry B*, 109 (47): 5100-5105, 2005.
25. Frank, A. J., Kopidakis, N., van de Lagemaat. Electrons in nanostructured TiO<sub>2</sub> solar cells: transport, recombination and photovoltaic properties *Coordination Chemistry* 248(13-14), 1165-1179, 2004.
26. M. Grätzel. Dye Sensitized Solar cells. *Journal of Photochemistry and Photobiology C* 4: 145-153, 2003.
27. Forro M., Chauvet E., Emin L., High-Mobility n-Type Charge Carriers in large Single-Crystals of Anatase TiO<sub>2</sub>. *Journal of Applied Physics* 75(1): 633-635, 1994.
28. Y. Luo, D. Li, Q. Meng. Towards Optimization of Materials for Dye-Sensitized Solar Cells. *Advanced Materials* 21: 4647-4651, 2009.
29. J. Bisquert, V.S. Vikhrenko. Interpretation of the Time Constants Measured by Kinetic Techniques in Nanostructured Semiconductor Electrodes and Dye-Sensitized Solar Cells. *Journal of Physical Chemistry B* 108: 2313-2322, 2004.
30. Frank, A. J.; Kopidakis, N.; van de Lagemaat, Electrons in nanostructured TiO<sub>2</sub> solar cells: transport, recombination and photovoltaic properties *Coordination Chemistry Reviews* 248(13-14) 1165-1179, 2004.
31. K. Prabakar, M. Son, D. Ludeman, H. Kim. Visible light enhanced TiO<sub>2</sub> thin film bilayer dye sensitized solar cells. *Thin Solid Films* 519, 894-899, 2010.
32. A. Yella. Porphrin-sensitized solar cell with cobalt (II/III)-based redox electrolyte exceed 12 percent efficiency. *Science* 334, 629-634, 2011.
33. M.A. Green, K. Emery Y. Hishikawa, W. Warta, and E.D. Dunlop. Solar Cell efficiency tables (version 38). *Progress in Photovoltaics: Research and Applications*, 10, 565-572, 2011.
34. I. Mora-Sero, J. Bisquert. Breakthroughs in the Development of Semiconductor-Sensitized Solar Cells. *Journal of Physical Chemistry Letters* 1, 3046-3052, 2010.
35. M.A. Green, K. Emery Y. Hishikawa, W. Warta, and E.D. Dunlop. Solar Cell efficiency tables (version 38). *Progress in Photovoltaics: Research and Applications*, 10, 565-572, 2011.
36. J.N Clifford, E. Palomares, M. K. Nazeeruddin, M. Grätzel, J.R. Durrant. Modulation of the rate of electron injection in dye-sensitized nanocrystalline TiO<sub>2</sub> films by externally applied bias *Journal of Physical Chemistry C*, 111: 6561, 2001.
37. H. Nusbaumer, J. Moser, S. Zakeeruddin, M.K. Nazeeruddin, M. Grätzel. Electron transfer dynamics in dye sensitized nanocrystalline solar cells using a polymer electrolyte *Journal of Physical Chemistry B* 105: 10461, 2001.

38. Yoo, K. Kim, S.H. Lee, W.M. Kim, N.G. Park. ITO/ATO/TiO<sub>2</sub> triple-layered transparent conducting substrates for dye-sensitized solar cells. *Solar Energy Materials and Solar Cells* 92(8) (2008) 873-877.
39. Sima, C. Grigoriu, S. Antohe. Comparison of the dye-sensitized solar cells performance based on transparent conductive ITO and FTO. *Thin Solid Films* 519: 595-597, 2010.
40. Y.L Lee, C.H. Chang. Efficient Polysulfide Electrolyte for CdS Quantum Dot-Sensitized Solar Cells. *Journal of Power Sources* 185: 584-588, 2008.
41. H.B. Lee, H.C. Leventis, S.J. Moon, P. Chen, et al. PbS and CdS Quantum Dot-Sensitized Solid-State Solar Cells: Old Concepts, New Results. *Advanced Functional Materials* 19, 1-8, 2009.
42. H. Nusbaumer, J. Moser, S. Zakeeruddin, M.K. Nazeeruddin, M. Grätzel. Electron transfer dynamics in dye sensitized nanocrystalline solar cells using a polymer electrolyte. *Journal of Physical Chemistry* 11, 1154-1159, 2006.
43. Peterson, J.J.; Krauss, T.D. Fluorescence Spectroscopy of Single Lead Sulfide Quantum dots. *Nano Letters*. 15(3), 510-514, 2006.
44. M. S. Sze. *Physics of Semiconductor Devices*. 2<sup>nd</sup> ed.; John Wiley and Sons: New York, 1981.
45. A. Braga, S. Gimenez, S. Concina, A. Vomiero, I. Mara-Sero. Panchromatic Sensitized Solar Cells Based on Metal Sulfide Quantum Dots Grown Directly on Nanostructure TiO<sub>2</sub> electrodes. *Journal of Physical Chemistry Letters*, 2: 454-460, 2011.
46. K.S. Leschkies, T.J. Beatty, T.J. Kang. Solar Cells based on junctions between colloidal PbSe nanocrystals and thin ZnO films. *ACS Nano*, 3: 3638-3648, 2009.
47. W Ma, J.M. Luther, H.M Zheng, Y. Wu. Photovoltaic devices employing ternary PbSe nanocrystals. *Nano Letters*, 9: 1699-1703, 2009.
48. E. Talgorn, Y. Gao, M. Aerts, and L.T. Kunneman. Unity quantum yield of photogenerated charges and band-like transport in quantum-dot solids. *Nature Nanotechnology*, 6: 733-739, 2011.
49. H.C. Leventis, S.A. Haque. Control of Charge Recombination oot Nanostructured Quantum-Dot Sensitized TiO<sub>2</sub> Interface Employing a Multi-Step Redox Cascade. *Energy Environmental Sciences*, 2: 1176-1179, 2009.
50. Luther, J. M.; Law, M.; Beard, M. C.; Song, Q.; Reese, M. O.; Ellingson, R. J.; Nozik, A. J. Schottky Solar Cells Based on Colloidal Nanocrystal Films. *Nano Letters* 8, 3488–3492, 2008.
51. A.G. Pattantyus-Abraham et al. Depleted-heterojunction colloidal quantum dot solar cells. *ACS Nano* 4: 3374-3380, 2010.
52. Braga, A.; Gimenez, S.; Concina, I.; Vomiero, A.; Mara-Sero, I. Panchromatic Sensitized Solar Cells Based on Metal Sulfide Quantum Dots Grown Directly on Nanostructure TiO<sub>2</sub> electrodes. *Journal of Physical Chemistry Letters*, 2: 454-460, 2011.
53. S.M. Yang, C.H. Huang, J. Zhai, Z.S. Wang, L. Jiang. High Photostability and quantum yield of Nanoporous TiO<sub>2</sub> Thin Film Electrodes Co-sensitized with Capped Sulfides. *Journal of Material Chemistry*, 12: 1459-1464, 2002.
54. A. Braga, S. Gimenez, I. Concina, A. AVomiero, I. Mora-Sero. Panchromatic Sensitized Solar Cells Based on Metal Sulfide Quantum Dots Grown Directly on Nanostructured TiO<sub>2</sub> Electrodes. *Journal of Physical Chemistry Letters*, 2: 454-460, 2011.

55. T. Schwieger, H. Peisert, M.S. Golden, et al. Electronic Structure of the organic semiconductor copper phthalocyanine and K-CuPc studied using photoemission spectroscopy. *Physical Review B*, 66: 1552071-1552075, 2002.
56. R.H. Friend, R.W. Holmes, et al. Electroluminescence in conjugated polymers. *Nature* 397(6715): 121-128, 1999.
57. Z. Bo, A.J. Lovinger, and A. Dodabalapur. Organic field-effect transistors with high mobility based on copper phthalocyanine. *Applied Physics Letters*, 69: 3066-3068, 1996.
58. J.S. Schon, C. Kloc, A. Dodabalapur. An organic solid state injection laser. *Science* 289 (5479): 599-601, 2000.
59. Y.A. Mikheev, L.N. Guseva, Y.A. Ershov. Vibronic Spectra of Solutions and Solutions of Copper Phthalocyanine. *Photochemistry and Magnetochemistry*, 81(4): 715-721, 2007.
60. Y.K. Zhou, C. Lin, F.B. Zhang, B.L. He, H.L. Li, *Journal of Electrochemical Society* 150, 1246-1249, 2003.
61. G. Howatt, R. Breckenridge, Fabrication of Thin Ceramic Sheets for Capacitors, J. Brownlow, *Journal of American Ceramics Society* 30, 237-242, 1947.
62. J.R. Li, Z.L. Tang, Z.T. Zhang, *Electrochimica Solid State Letters* 8 A316, 2005.
63. Y. Wang, M. Wu, W.F. Zhang. Preparation and electrochemical characterization of TiO<sub>2</sub> nanowires as an electrode material for lithium-ion batteries. *Electrochimica Acta* 53 (2008) 7863–7868
64. Y. Ohsaki, N. Masak, T. Kitamura, Y. Wasa, T. Okamoto, T. Sekino, K. Nukara, and S. Yanagida. Dye Sensitized TiO<sub>2</sub> Nanotube Solar Cells: fabrication and electronic characterization. *Physics Chemistry: Chemical Physics*, 7, 2005.
65. D. Kuang, J. Brillet, P. Chen, M. Takata, S. Uchida, H. Miura, K. Sumioka, and M. Gratzel. Application of highly order TiO<sub>2</sub> Nanotube arrays in flexible dye-sensitized solar cells. *ACS Nano*, 2(6): 1113-1116, 2008.
66. B. Tan, Y. Wu. Dye-Sensitized Solar Cells. *Journal of Photochemistry and Photobiology C: Photochemistry Review*, 4(2): 145-153, 2003.
67. K. Wang, "Nanomaterials: from Interfacial Characteristics to Device Applications", Ph.D. Dissertation, McMaster University, ON, Canada 2011.
68. N. Koidakis, K.D. Benkstein, J. van de Lagemaat, A. Transport-Limited Recombination of Photocarriers in Dye-Sensitized Nanocrystalline TiO<sub>2</sub>. *Journal of Physical Chemistry B*, vol. 107, no. 41, pp. 11307-11315, 2003.
69. J. J. Peterson, T.D. Krauss. Fluorescence Spectroscopy of Single Lead Sulfide Quantum Dots. *Nano Letters* 6(3), 510-514, 2006.
70. H. Lee, H. Leventis, S.J. moon, P. chen, S. Ito, S. A. Haque, T. Torres, and M. Gratzel. Pbs and Cds Quantum Dot-Sensitized Solid State Solar cells: "Old Concepts, new Results." *Advanced Functional Materials* 29, 2735-2742, 2009.
71. S.M. Yang, C.H. Huang, J. Zhai, Z.S. Wang, L. Jiang. High Photostability and quantum yield of Nanoporous TiO<sub>2</sub> Thin Film Electrodes Co-sensitized with Capped Sulfides. *Journal of Material Chemistry*, 12: 1459-1464, 2002.
72. J.H. Yoon, S.R. Jang, R. Vittal, J. lee, K.J. Kim, *Journal of Photochemistry and Photobiology A: Chemistry*, 180, 184-188, 2006.

73. B. B. Hyun, A. C. Bartnik, L. Sun, T. Hanrath, and F.W. Wise. Control of electron transfer from lead Salt nanocrystals in  $\text{TiO}_2$ . *Nano Letters* 11 (5), 2126-2132, 2011.
74. N.G. Park, J. Lagemaat, A.J. Frank. *Journal of Physical Chemistry B*, 104, 8989-8994, 2000.